University of New Mexico
UNM Digital Repository

Civil Engineering ETDs | Engineering ETDs

2-1-2012

Clarification of the notched beam Level II Testing Procedures of ACI 446 Committee Report 5

Scott Chapman

Follow this and additional works at: https://digitalrepository.unm.edu/ce_etds

Recommended Citation
Chapman, Scott. "Clarification of the notched beam Level II Testing Procedures of ACI 446 Committee Report 5." (2012).
https://digitalrepository.unm.edu/ce_etds/57

This Thesis is brought to you for free and open access by the Engineering ETDs at UNM Digital Repository. It has been accepted for inclusion in Civil Engineering ETDs by an authorized administrator of UNM Digital Repository. For more information, please contact disc@unm.edu.

Scott Stephen Chapman
Candidate

Department of Civil Engineering
Department

This thesis is approved, and it is acceptable in quality and form for publication:

Approved by the Thesis Committee:

, Chairperson

CLARIFICATION OF THE NOTCHED BEAM LEVEL II TESTING PROCEDURES OF ACI 446 COMMITTEE REPORT 5

BY

SCOTT STEPHEN CHAPMAN

BACHELORS OF SCIENCE, CIVIL ENGINEERING

THESIS

Submitted in Partial Fulfillment of the
Requirements for the Degree of

Master of Science

Civil Engineering

The University of New Mexico
Albuquerque, New Mexico

December, 2011

©2011, Scott Stephen Chapman

ACKNOWLEDGMENTS

I would like to extend special thanks to my advisor and committee chairperson, Dr. Walter Gerstle, for his immeasurable support of my education over both my undergraduate and graduate studies at the University of New Mexico. His insight and guidance over the years has been invaluable, and will remain with me as I continue my career.

I also would like to extend thanks to my committee members, Dr. Mahmoud R. Taha and Dr. Arup K. Maji for their insight and criticism. Also, Dr. Taha was instrumental in acquiring the testing equipment for the experiments.

I'd also like to thank my fellow graduate students Rick Grahn and Jacob Hays for their help in the lab, and special thanks to my colleague and fellow graduate student, Ebadollah Honarvar Gheitenbaf, for his help with the development, analysis, and execution of the experiments.

Lastly, I would like to thank my parents, friends and family for their love and support over the years.

CLARIFICATION OF THE NOTCHED BEAM LEVEL II TESTING PROCEDURES OF ACI 446 COMMITTEE REPORT 5

BY

SCOTT STEPHEN CHAPMAN

ABSTRACT OF THESIS

Submitted in Partial Fulfillment of the
Requirements for the Degree of

Master of Science

Civil Engineering

The University of New Mexico
Albuquerque, New Mexico

December, 2011

CLARIFICATION OF THE NOTCHED BEAM LEVEL II TESTING PROCEDURES OF ACI 446 COMMITTEE REPORT 5

by

Scott Stephen Chapman

B.S., Civil Engineering, University of New Mexico, 2009
M.S., Civil Engineering, University of New Mexico, 2011

ABSTRACT

Concrete under tension exhibits a great degree of post-peak non-linearity. Current design codes assume the tensile strength of concrete to be negligible, which is not only a gross oversimplification of the fracture process of concrete in tension, but is also overly conservative. However, research in the field of fracture mechanics has produced models that can accurately predict crack propagation in concrete using fracture parameters determined from testing. One of these models, which is both simple and reasonably accurate, estimates the post-peak tensile behavior of concrete as a bilinear approximation of the softening curve, known as the bilinear cohesive crack model.

The American Concrete Institute's Committee 446 is developing a draft test method, ACI 446-5, which determines the key fracture parameters of the bilinear cohesive crack model using three-point bend notched beam tests. ACI 446-5 currently contains errors and some impractical methods, combined with complex and often obscure equations for the determination of the bilinear cohesive fracture parameters.

To remedy this, the equations for the calculation of the fracture parameters of the bilinear cohesive crack model are derived, and the experimental methods examined and criticized. Experiments of normal strength

concrete notched beams of three different sizes were also performed using the guidelines for Level II testing, provided in Chapters 2 and 4 of ACI 446-5, with modifications as needed in the case of ambiguity or impracticality. The results are analyzed and discussed, and potential size dependence of the fracture parameters is discussed. With the corrections provided in this thesis, ACI 446-5 is concluded to be adequate for the determination of the fracture parameters of the bilinear cohesive crack model, and modifications are suggested to improve the test method.

TABLE OF CONTENTS

LIST OF FIGURES

LIST OF TABLES

1 INTRODUCTION

Considerable effort has been expended in the attempt to model the behavior of concrete under tensile forces. Due to the complex behavior of concrete under tension, most modern design codes neglect the tensile strength of concrete altogether. This conservative assumption denies designers the ability to not only cut costs through the extra strength in tension concrete can offer, but also completely ignores the process of crack propagation. Researchers have long been aware of these problems, and throughout the years have developed several models that attempt to use the material properties of concrete to predict both failure and the process of crack propagation. Due to its complex structure and heterogeneity, replicating the behavior of concrete using classic analytical methods from mechanics of materials and other computational models has proven quite difficult.

However, the field of fracture mechanics has shown much promise in predicting crack propagation of concrete under tensile forces. In particular, the American Concrete Institute (ACI) is in the process of developing a standard testing method to determine key fracture parameters and material properties of concrete using simple three-point bend notched beam tests that can be performed in any modern materials laboratory. In March, 2010, ACI Committee 446 released a draft test method for fracture toughness testing of concrete, known as notched beam level II (NBLII) tests. This test method will be the focus for this thesis. In particular, this thesis provides the results of trial runs of NBLII tests of three different beam sizes of normal strength concrete, as well as adaptations, criticisms, and an in-depth discussion of the proposed testing method and the calculations of the key fracture parameters.

1.1 Motivation

Although the field of fracture mechanics has been broadly studied for many decades, its practical applications in design are currently limited. In particular, design codes for structures using reinforced concrete generally only use the uniaxial compressive strength of concrete, f'_c, to determine failure and

serviceability criteria. Although the equations for design using f'_c have proven to be adequate in most cases, they make gross assumptions concerning the behavior of concrete, where using parameters such as the fracture toughness of concrete would be more appropriate.

Part of the reason for the popularity of f'_c comes from the fact that the tests to determine compressive strength are very simple, repeatable, and only one calculation needs to be made; dividing the ultimate uniaxial force by the cross-sectional area of the specimen. By contrast, in the field of fracture mechanics of concrete, there currently exists no agreed upon standard testing method to determine key fracture parameters. In fact, there is still no agreement on a single theoretical model that can be used to describe crack propagation.

Despite this, it is expected in the future that the principles of fracture mechanics will be used in design codes. In order for this to occur, a standardized and agreed upon theoretical model and testing method must be developed. ACI Report 446-5 on Fracture Toughness Testing (ACI 446-5) provides two such standards with Level I and Level II beam tests, but is still in the developmental phase and requires further rigorous scrutiny. One of the motivations for this thesis is to provide such scrutiny, and to determine if the Level II testing method provided by ACI 446-5 is an adequate and reasonable method for determining the key fracture parameters of concrete. Also, the equations to calculate the fracture parameters listed in Chapter 4 of ACI 446-5 are very complex and often have obfuscated origins. Thus, this thesis provides a guide to the equations in Chapter 4 of ACI 446-5 by showing derivations where needed and providing scientific reasoning and criticism where appropriate.

1.2 Background

Concrete under tension exhibits a large degree of non-linearity close to and beyond its tensile strength. While simple tests to discover the tensile strength of concrete are reasonably well established, the tensile strength alone does nothing to describe concrete behavior past the peak load. In general, normal-strength concrete under tension exhibits approximately linear-elastic

behavior up to its peak tensile strength. After reaching peak tensile stress, concrete exhibits strain-softening behavior by gradually losing load-carrying capacity as deformation increases. In a typical load-deformation curve, after reaching maximum load, load asymptotically approaches zero as deformation increases. This behavior differs greatly from classically brittle materials, such as glass, which suddenly lose all load-carrying capacity after reaching maximum load, disallowing any further deformation. It also differs from typically ductile materials, such as steel, which exhibit yielding where deformation increases without increases in load, and eventually strain hardening, in which greater load is needed for further deformation. Concrete thus has been labeled as a quasi-brittle material, and falls under the realm of quasi-brittle fracture mechanics.

From a mechanics perspective, strain-softening in concrete occurs due to the existence of micro-cracks in the cementitious material surrounding the aggregate. In brittle materials, a single crack propagates through the material, with a very small fracture process zone in front of the crack. By contrast, concrete has a very long, but narrow fracture process zone due to micro-cracks forming at relatively large distances in front of the main crack, with a typical characteristic size in the range of 0.15 m – 0.40 m [Bazant & Planas, 1998]. With such a large fracture process zone, concrete does not fall under the realm of linear-elastic fracture mechanics, and thus other models have been developed in an attempt to replicate the crack-propagation of concrete.

One of the first of these models is the fictitious crack model developed by Hillerborg, which proposed the notion of a crack that has the ability to transfer tensile stress across the crack faces [Hillerborg, 1978]. The idea of this "cohesive zone" was later employed by Guinea et al. into what is known as the bilinear cohesive crack model [Guinea 1994], which assumes a bilinear approximation of the softening curve of concrete. This model is the basis for ACI 446-5 testing methods, and will be explored in detail in Chapter 2 of this thesis.

1.3 Objectives and Scope

The primary purpose of this thesis is to determine whether ACI 446-5 Level II test method is suitable as a standard for fracture toughness testing. For this conclusion to be satisfied, several criteria must be met. Primarily, the test must be relatively simple, inexpensive to perform, and repeatable. Also, the issue of potential dependence of the fracture parameters upon specimen size must be explored.

In fulfillment of the above requirements, the equations defining the bilinear cohesive crack model are explained and derived. Also, a thorough and descriptive examination of the testing procedures of ACI 446-5 is provided by performing several experimental trials using the proposed method, along with in-depth discussion and criticism where appropriate. Results of the tests are then analyzed to determine if the testing procedure delivers realistic and objective values, and conclusions are drawn with respect to the validity of the testing method.

Chapter 2 focuses on the theoretical background of the NBLII test method, providing the provenance of the calculations required to determine the cohesive crack model parameters utilized by ACI 446-5. Chapter 3 provides an in-depth description, criticism, and discussion of the NBLII testing methods, along with the raw experimental results of the experiments. Chapter 4 analyzes and discusses the results from the experiments, providing the key fracture parameters and bilinear approximations of the cohesive model for concrete. Lastly, Chapter 5 draws conclusions about the experimental methods and makes recommendations for further research and testing.

2 THE BILINEAR COHESIVE FRACTURE PARAMETERS

The ACI 446-5 NBLII testing method and the testing presented in this document follow what is known as the bilinear cohesive crack model, originally developed by Guinea et al., to create a four-parameter fracture mechanics model to describe the post-peak behavior of concrete as a bilinear approximation of the softening curve [Guinea et al., 1994]. This chapter is dedicated to the origins of the cohesive crack model, including the background and the provenance of the equations used to calculate the fracture parameters of the bilinear approximation of the softening curve of concrete. Section 2.1 discusses Hillerborg's fictitious crack model and the determination of the fracture energy, G_F, while Section 2.2 discusses the four-parameter bilinear cohesive crack model of Guinea et al. and the calculation of the fractures parameters in Chapter 4 of ACI 446-5.

2.1 Hillerborg's Model and the Determination of G_F

As discussed in Chapter 1, concrete is a quasi-brittle material with a large fracture process zone, and thus the principles of linear elastic fracture mechanics (LEFM) are not applicable. LEFM assumes that stresses at the crack tip approach infinity, where in reality the maximum stress achievable is the tensile strength of the material, f_t. Hillerborg reconciled this discrepancy by providing a fictitious crack ahead of the crack tip that imposes closing forces within the fracture process zone [Hillerborg, 1978]. As the crack widens, the closing forces within the cohesive zone decrease from f_t as the crack opening increases, and thus allows for the generation of the softening behavior seen in tension tests of concrete. Figure 1 depicts a graphical representation of this concept, where the maximum tensile stress, f_t, is reached, and as the crack opening, w, increases the stress, σ, decreases non-linearly until a critical crack opening displacement, w_c, is reached where the cohesive stress is reduced to zero.

The fracture energy dissipated per unit of crack area, G_F, is then defined as the area under the stress vs. crack opening displacement curve. G_F is

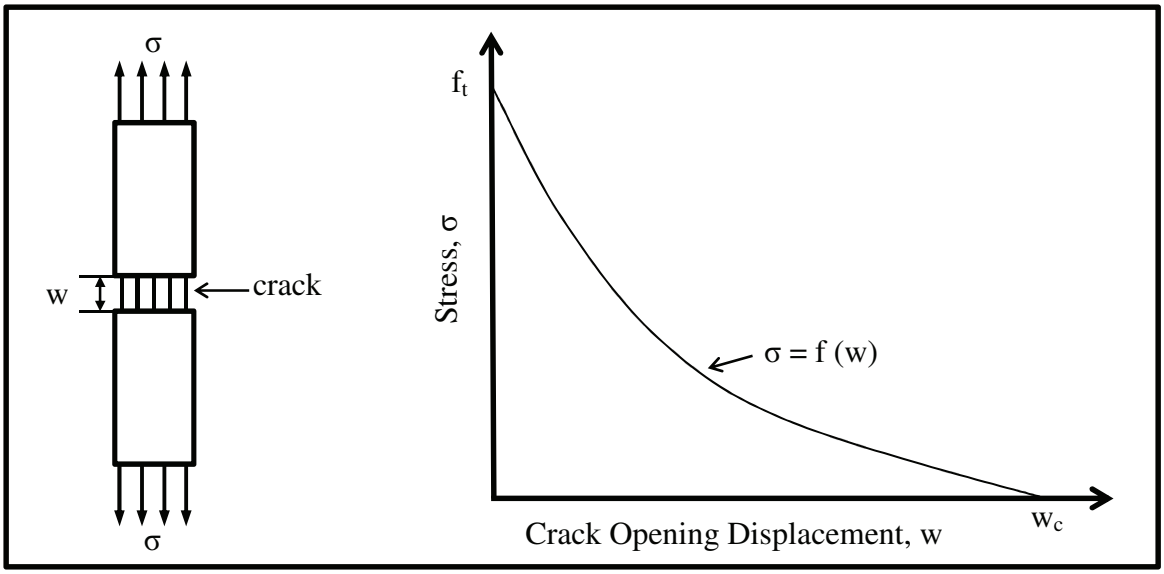

Figure 1: Graphical description of the cohesive zone, and accompanying stress vs. crack opening displacement curve

a material property of the concrete and represents the amount of external applied energy required to fully break a unit surface area of the cohesive crack. Hillerborg contended that G_F could be determined through the load-deformation curve data from three-point bend notched beam tests (without compensation for self-weight) by dividing the area under the load-deformation curve by the notched cross-sectional area of the specimen [Hillerborg, 1985]. However, the literature has shown that G_F exhibits considerable dependence on specimen size using Hillerborg's methods [Shah et al., 1995]. The primary reason for this size dependence is attributed to not accounting for energy dissipated at the tail end of the curve, where theoretically the load-deformation curve asymptotically approaches zero. ACI 446-5 provides an equation for G_F that takes into account the tail of the curve, as well as using slight over-compensation for self-weight, which will be discussed further in Section 3.2.2, to prevent dynamic instability before a full softening curve can be developed. To fully understand the origin of the ACI 446-5 NBLII method for the determination of G_F, one must explore its development. In particular, the work by Peterson is summarized next [Peterson, 1981].

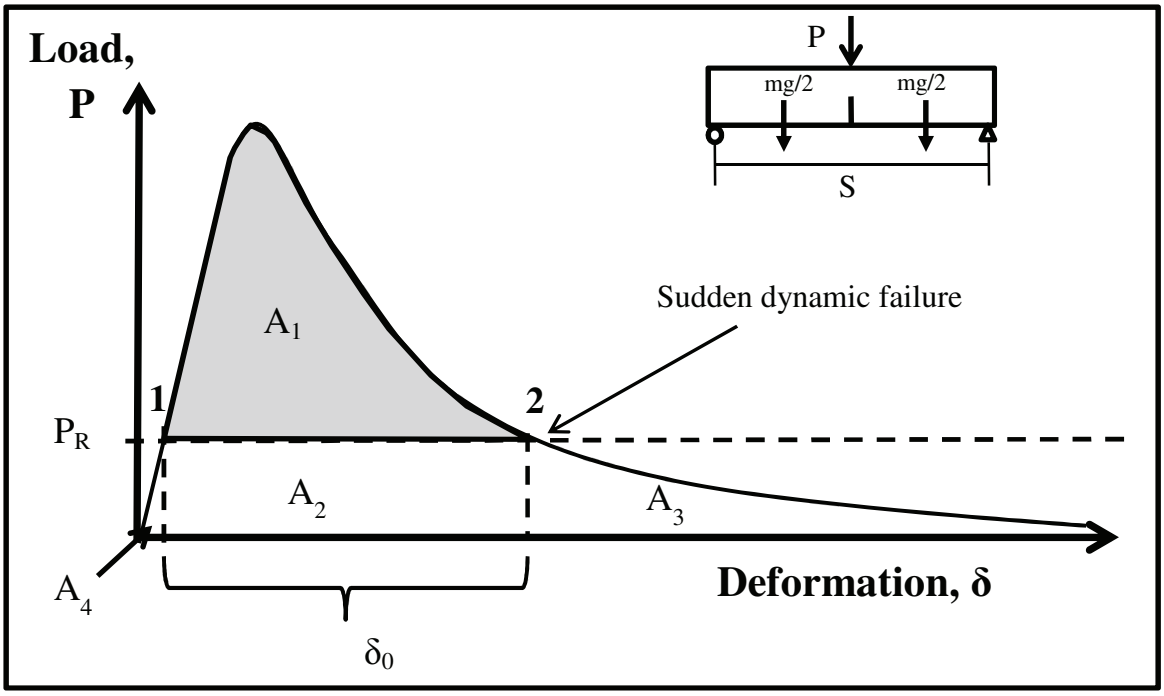

Figure 2: Load-deflection curve for a three-point bend test

Figure 2 shows a theoretical load-deformation curve using no weight compensation. With no weight compensation, the self-weight of the specimen contributes to the overall load in the system, and must be accounted for. The self-weight of the specimen is acting upon the system before testing begins, and thus the test actually starts at a non-zero load before any load by the testing machine is applied. The center-span moment due to this non-zero load of specimen self-weight, for a simply supported beam, is mgS/8, where m is the total mass of the beam, g is the acceleration of gravity and S is the span length of the test setup. Subsequently, an equivalent center-span load of P_R = mg/2, would cause the same moment at mid-span, and is referred to as the residual load. Thus, the recorded test data would occur in the shaded area of Figure 2, beginning at point 1 and ending in sudden unstable failure due to the beam's self-weight at point 2. The entire load-deformation curve, including the effect of self-weight, is represented by both the un-shaded and shaded areas of Figure 2. Integrating under the entire load-deformation curve ($A_1 + A_2 + A_3 + A_4$), and dividing by the cross-sectional area of the notched section, will yield the fracture

energy, G_F. A_1 is easily obtained from the test data by means of trapezoidal integration. The rest of the curve, however, is interpolated, as described next.

Generally, A_4 can be neglected as it is very small, normally 1 – 2% of the entire area [Peterson, 1981]. Knowing the deformation and residual load at point 2 (δ_0 and P_R respectively) from the recorded test data, A_2 can be calculated as follows:

$$A_2 = P_R \delta_0 \ . \qquad (1)$$

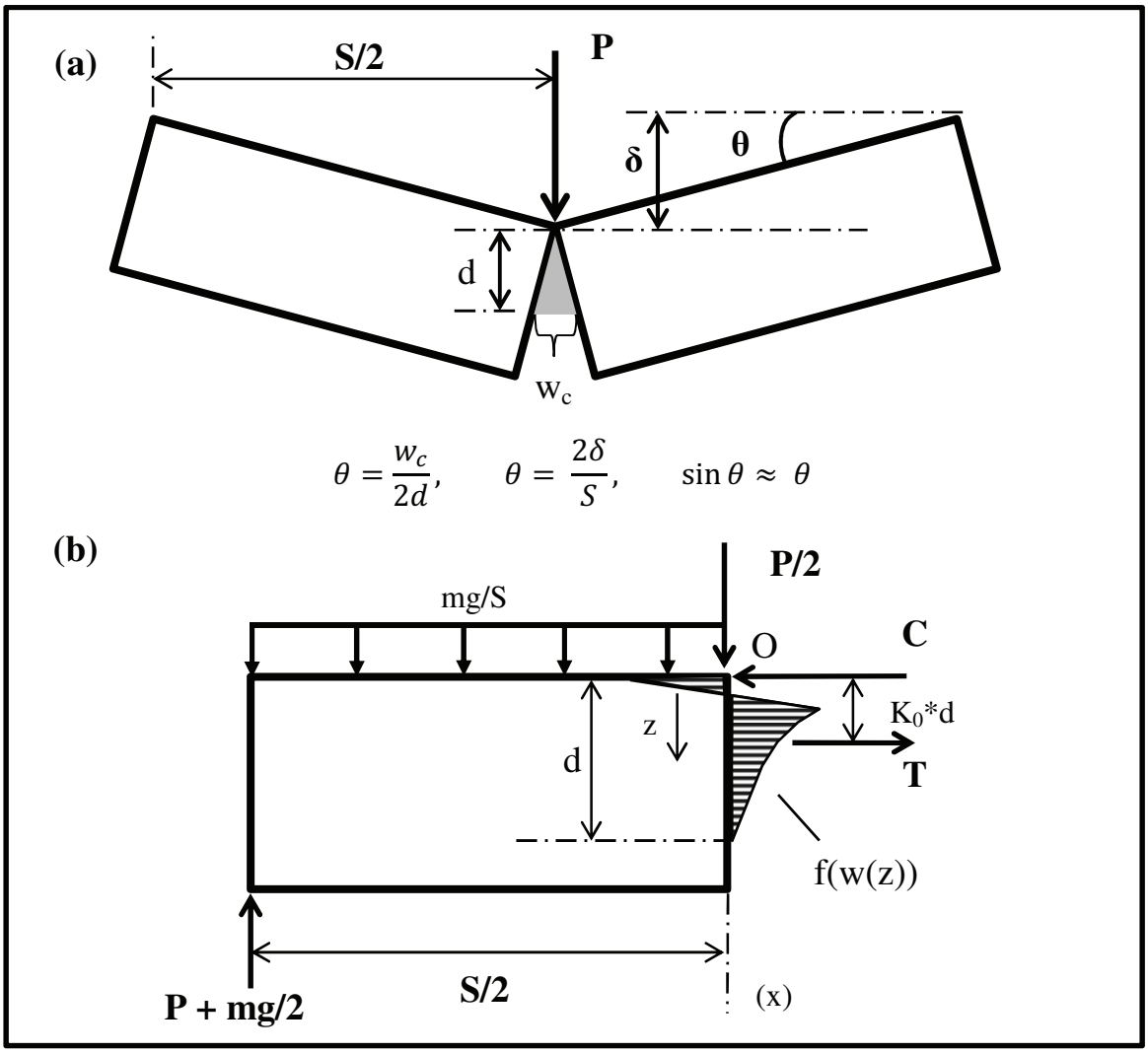

Figure 3: Graphical description and free body diagram of beam behavior toward the end of the test

To determine A_3, several assumptions must be made about the geometry of the area at the far tail of the curve. Toward the end of the test, one can

assume the beam acts as two separate rigid rectangular pieces held together only through the cohesive zone, as depicted in Figure 3 (a), where the cracked surfaces remain plane, the depth of the cohesive zone, d, varies based upon the displacement, δ, and the critical crack opening displacement, w_c, is always constant at depth d. This is an approximation as it assumes the stress in the compression zone of the beam is concentrated at a single point, seen as force C in Figure 3 (b). In reality there will always be a compressive zone of finite depth at the top of the beam. Using the beam geometry as seen in Figure 3 (a), with the foregoing assumptions and with a real crack propagating, the depth of the cohesive zone, d, is inversely proportional to the deformation of the beam, δ, i.e.:

$$d = \frac{Sw_c}{4\delta} \ . \tag{2}$$

In Figure 3 (b), the stress distribution of the cohesive zone is shown as a function of the vertical axis z, and the tensile portion of this function is labeled as f(z), where the resultant, T is:

$$T = B\int_{z=0}^{d} f\big(w(z)\big)\,dz \ , \tag{3}$$

where B is the width of the beam. The resultant tensile force, T, is located at a distance from the top of the beam that is proportional to d, denoted by a constant, K_0, times d. Summing moments about point O, we get the following:

$$0 = K_0 Td + \frac{mgS}{8} - \frac{PS}{4} - \frac{mgS}{4}. \tag{4}$$

Rearranging equation (4), we get:

$$\frac{S}{4}\left(P + \frac{mg}{2}\right) = K_0 Td \ . \tag{5}$$

Defining the load function P(δ) = P + mg/2, we get:

$$\frac{P(\delta)S}{4} = K_0 Td \ . \tag{6}$$

We know from the geometry in Figure 3 (a) that w can be related to d as the following:

$$w = \frac{z}{d}w_c \ ; \ z = \frac{wd}{w_c} \ . \tag{7}$$

Substituting equation (7) into equation (3), we get:

$$T = B \int_{w=0}^{w_c} f(w) \frac{d}{w_c} \, dw \ . \tag{8}$$

We also know from the definition of G_F that

$$G_F = \int_{w=0}^{w_c} f(w) \, dw \ . \tag{9}$$

With d being an independent variable, and w_c a constant, equation (8) becomes:

$$T = dB \frac{G_F}{w_c} \ , \tag{10}$$

and thus, T is proportional to d. Knowing this, and solving for P(δ) in equation (6), the equation becomes:

$$P(\delta) = K_0 \frac{4BG_F}{Sw_c} \, d^2 \ , \tag{11}$$

Substituting in d from equation (2) into equation (11), and knowing that w_c, S, G_F and K_0 are constants, for simplicity we can combine them into a single constant, K_1, and equation (11) becomes:

$$P(\delta) = \frac{K_1}{\delta^2} \ , \qquad K_1 = \frac{1}{4} BSK_0 G_F w_c \ . \tag{12}$$

Referring back to Figure 2, we now have an approximate function of the curve over area A_3 for large deformations. A_3 can be calculated by integrating the function as follows:

$$A_3 = \int_{\delta_0}^{\infty} P(\delta) d\delta \ = \ \int_{\delta_0}^{\infty} \frac{K_1}{\delta^2} d\delta \ = \frac{K_1}{\delta_0} \ = \ \frac{K_1}{\delta_0^2} \delta_0 \ , \tag{13}$$

which then, knowing that $P(\delta_0) = P_R$, and substituting equation (12) into equation (13), we find:

$$A_3 = P_R \delta_0 = \ A_2 \ . \tag{14}$$

Now that all the areas are approximately accounted for, the fracture energy can be calculated as the entire area under the curve in Figure 2 divided by the cross-sectional area of the cracked section as follows:

$$G_F = \frac{(A_1 + 2P_R \delta_0)}{B(D - a_0)} \ , \tag{15}$$

where B is the beam width, D is the beam depth, and a_0 is the notch depth.

However, equation (15) assumes that when $\delta=\delta_0$, the specimen is very close to the complete failure. This is an incorrect assumption, especially for larger beams where P_R can be a significant fraction of the peak load, due to the beam failing dynamically due to self-weight before a satisfactory softening curve can be developed. Thus, size dependence is expected for this testing method.

It should be noted that Hillerborg gave an alternate method and equation where the beam can be tested upside-down to eliminate self-weight as the cause of size dependence. However, not only was this method relatively unsafe, but size dependence was still observed in tests following this procedure [Shah et al., 1995]. In an attempt to eliminate size dependence, the far tail of the softening curve needs further examination. To achieve this, significant data from the far tail of the softening curve is needed, and thus weight compensation must be used in some form to counter-act the tendency of beams to fail prematurely due to self-weight before the curve can be satisfactorily developed. The use of counterweights at the ends of the beams to create a balancing negative moment has proven to be the most practical solution to this problem. However, this creates some other challenges in the calculation of G_F.

Ideally, a beam would have weight compensation so that no internal moment exists at center span. This is unrealistic due to the variability in casting of specimens and the heterogeneity of concrete, and thus it is more practical to provide a slight overcompensation, which achieves stability toward the end of the test and is also easier to correct for in the calculations. The correction terms for the calculation of G_F used in Chapter 4 of ACI 446-5 are in part related to the derivation developed in the book by Bazant and Planas, which is summarized below [Bazant & Planas, 1998].

Figure 4 depicts a typical load-deformation curve for a load-compensated beam similar to that of Figure 2, with a few key differences. The test is ended at the point δ_R and the curve asymptotically approaches a load, P'_0, which is the equivalent center-span downward force necessary to equilibrate the negative moment provided by the counterweights.

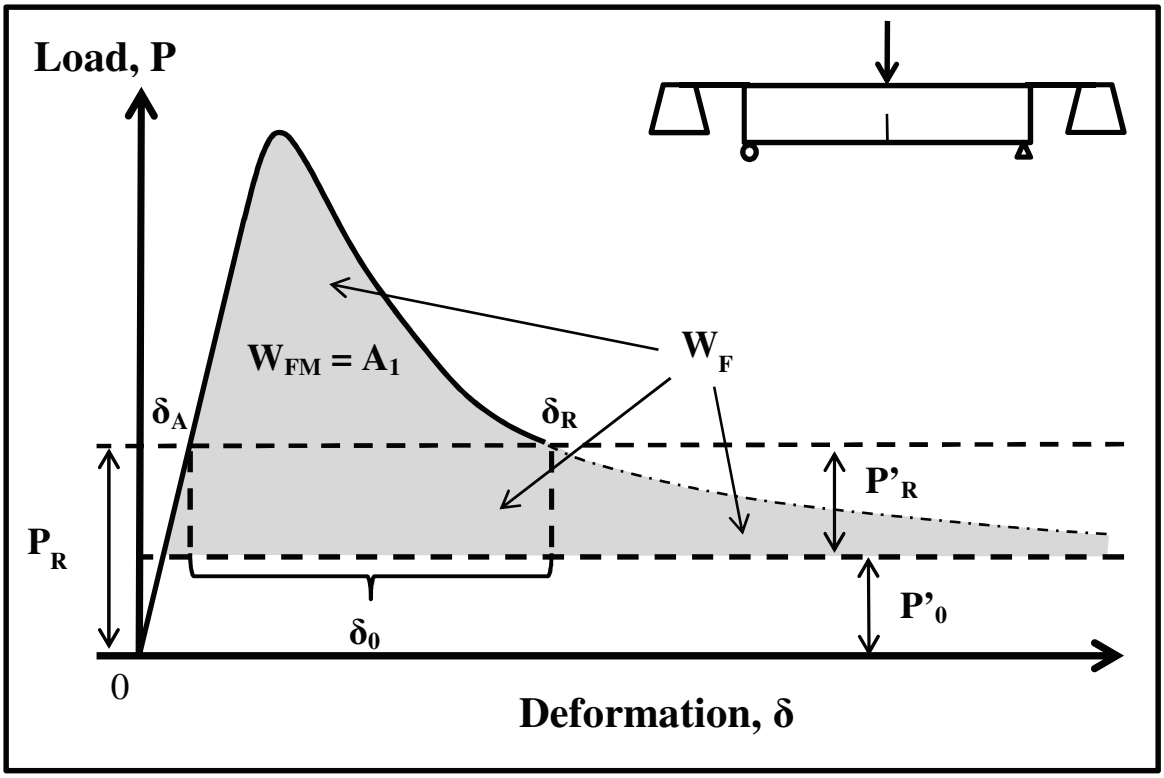

Figure 4: Load-deformation curve for overcompensated three-point bend test

P_R is defined, once again, as the residual load at the end of the test, which is taken directly from the testing data. P'_R then is the difference between P_R and P'_0. For illustrative purposes, P'_0, P'_R and P_R are all grossly exaggerated, as with slight overcompensation they would only be small fractions of the peak load. It should also be noted that P'_0 is difficult to know in advance, but as will be shown is not necessary in the final calculation of area. For convenience, another term is also introduced, known as the work of fracture, W_F, which represents the entire shaded area under the load-deformation curve in Figure 4, similar to the sum of the areas from Figure 2 ($A_1 + A_2 + A_3 + A_4$). The term W_{FM} represents the area under the curve obtained directly from the test data through trapezoidal integration, which is equivalent to A_1 in Figure 2. Lastly, δ_A represents the displacement at a load P_R near the beginning of the test, and δ_R represents the displacement at the end of the test. δ_R is known from the test data, and δ_A can be interpolated from the data lying in the initial linear portion of the curve. Using the same logic to determine A_3, employed in equation (14), and with the new

definition of W_F and W_{FM}, the total area of under the curve can be calculated as follows:

$$W_F = W_{FM} + 2P'_R\delta_0 \ . \tag{16}$$

From equation (12), without weight compensation, it is approximated that at the end of the test that $P(\delta) = K_1/\delta^2$, where K_1 is a constant. With weight compensation and for the large displacements at the far tail of the curve, equation (12) is then modified as follows:

$$P - P'_0 = \frac{A}{(\delta - \delta_A)^2} \ , \tag{17}$$

where $A = K_1$, and is referred to as the far tail constant. Note that equation (17) is slightly different from that of equation (12) since the curve has been shifted upward by an amount P'_0 and to the right by an amount δ_A due to the overcompensation by the counterweights.

The far tail constant, A, can then be calculated using the least squares method with data obtained from the far end of the curve. P'_0 is technically not necessary for the calculation of A, and the fitting curve can be forced through the point δ_R. Thus, equation (17) can be manipulated as follows:

$$P_R - P'_0 = P'_R = \frac{A}{(\delta_R - \delta_A)^2} \ . \tag{18}$$

Eliminating P'_0, and with some algebraic manipulation, equation (18) then becomes:

$$P - P_R = A\left[\frac{1}{(\delta - \delta_A)^2} - \frac{1}{(\delta_R - \delta_A)^2}\right] \ . \tag{19}$$

Then, data obtained from the end of the test can be used to perform a least-squares fit to determine A. Once A is known, the work of fracture can be calculated by substituting P'_R from equation (18) into equation (16), which yields:

$$W_F = W_{FM} + 2\frac{A}{(\delta_R - \delta_A)} \ . \tag{20}$$

Finally, the fracture energy is calculated as:

$$G_F = \frac{W_F}{B(D - a_0)} \ . \tag{21}$$

Note that equations (20) and (21) correspond to the equations in Sections 9.6.4 and 9.6.5 respectively in Chapter 4 of ACI 446-5.

However, equation (19) does not match up exactly to the equation in Section 9.3.4 of Chapter 4 of ACI 446-5, which is used to calculate the far tail constant, A. ACI 446-5 switches values of displacement for those of crack mouth opening displacement (CMOD), with a geometrical factor to relate CMOD to δ. It is noted that the reasoning for this cannot be found in the literature. Above, we assumed that toward the end of the test the beam acts as two rigid pieces, and therefore CMOD is proportional to δ. However, the forgoing assumption is only an approximation, and due care should be taken by ACI 446-5 to justify this assumption of proportionality, as even small errors and approximations can have significant influence on the fracture parameters (discussed further in Chapter 4 of this thesis).

With the above assumption, the manipulation of equation (19) to that of the equation in Section 9.3.4 in Chapter 4 of ACI 446-5 is fairly straight forward. By using the same logic employed in equation (2), and substituting the cohesive zone depth, d, for the full depth of the beam, D, and the critical crack opening displacement, w_c, for the crack mouth opening displacement, w_M, and, finally, solving for the displacement, δ, we get:

$$\delta = \frac{S w_M}{4D} \quad . \tag{22}$$

For simplicity, the term $P - P_R$ from equation (19) is replaced with what ACI 446-5 refers to as the corrected load, P_1, where P is the recorded load data, and P_R is the known residual load at the end of the test. As will be discussed in Chapter 3, a pre-load of 5-10% of the recorded peak load is also applied before testing begins to allow for testing setup seating. Data is not recorded during pre-loading, and thus the test begins at a load P equal to the pre-load. Testing is completed when the final CMOD reaches a value of 4D/300, as per Section 7.6.3 of Chapter 2 of ACI 446-5.

Section 9.3 of Chapter 4 of ACI 446-5 details the method to obtain A by least squares analysis. First, P_1 is first plotted against measured values of

CMOD. A typical plot of P_1 vs. CMOD is shown in Figure 5, where w_{MA} is the CMOD corresponding to a corrected load of $P_1 = 0$, and w_{MR} is the last point of CMOD on record.

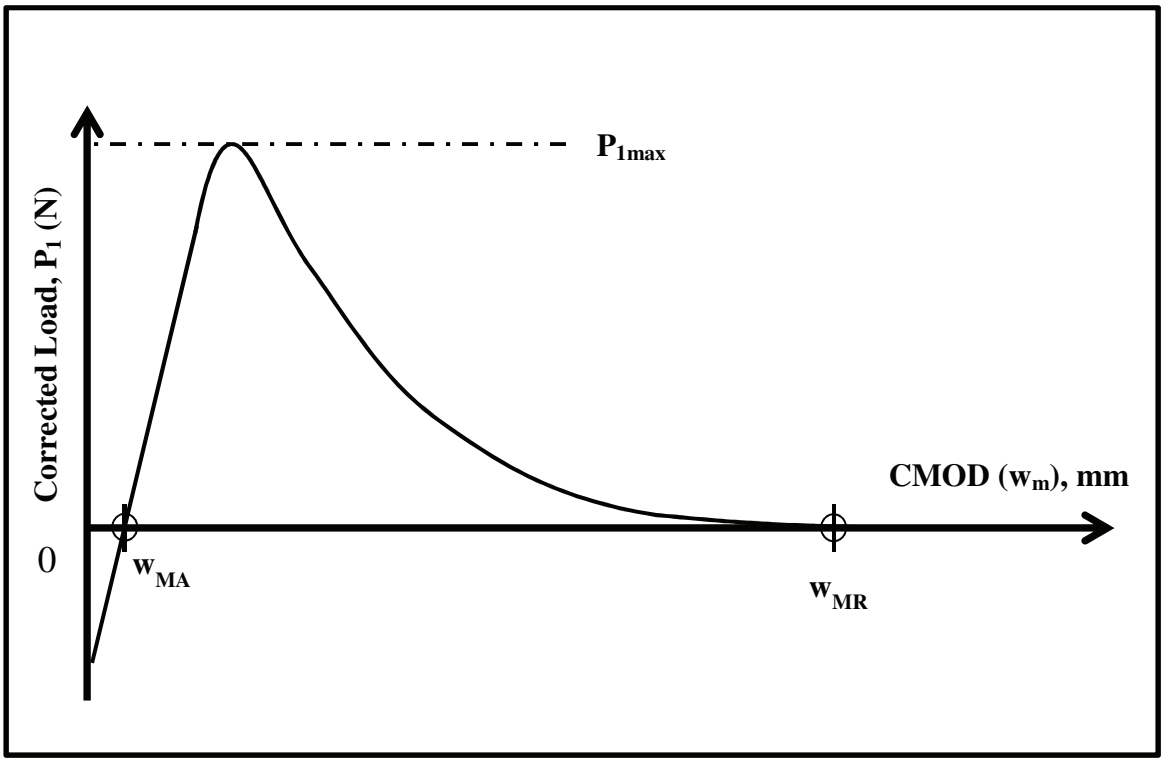

Figure 5: Plot of corrected load, P1 vs. CMOD

It should be noted that Section 9.3.1 of Chapter 4 of ACI 446-5 contains some confusing language, where it appears to suggest that all data corresponding to a CMOD greater than 2 mm should be excised. This requirement is curious, as there's no obvious reason to excise data collected beyond CMOD = 2 mm. Also, with larger depth specimens, Chapter 2 of ACI 446-5 allows for data to be collected to CMOD = 4D/300, which could easily exceed the 2 mm requirement. The author recommends that this requirement be removed.

Note in Figure 5 that the corrected load-deformation curve appears nearly asymptotic to a corrected load of zero. This is due to the expectation that with weight compensation, it is possible to achieve a long tail of the softening curve. Also, it is expected that some of the initial linear portion of the corrected curve will be negative, as the overcompensation by the counterweights will cause a

slightly positive residual load at the end of the test, which when adjusted for will move the curve downward. The value w_{MA} then is determined through interpolation of the corrected data where the initial linear portion of the curve crosses the x-axis in Figure 5. Substituting equation (22) into equation (19), and P_1 for $P - P_R$ we get:

$$P_1 = A\left(\frac{4D}{S}\right)^2\left[\frac{1}{(w_M - w_{MA})^2} - \frac{1}{(w_{MR} - w_{MA})^2}\right], \quad (23)$$

where w_M is CMOD data taken from the far tail of the curve. In accordance with Section 9.3.4 of Chapter 4 of ACI 446-5, data corresponding to loads less than or equal to 5% of P_{1max} from the far tail of the curve is collected for the least squares analysis to determine A.

To assist in the calculation of A, ACI 446-5 creates another term, X, so that $P_1 = AX$. X is calculated as follows for each data point of w_M:

$$X = \left(\frac{4D}{S}\right)^2\left[\frac{1}{(w_M - w_{MA})^2} - \frac{1}{(w_{MR} - w_{MA})^2}\right]. \quad (24)$$

Section 9.3.5 of Chapter 4 of ACI 446-5 allows for a simple linear regression to determine A. However, when plotting P_1 vs. X, ACI 446-5 suggests the curve more closely resembles a quadratic equation as follows:

$$P = X(A + KX), \quad (25)$$

where K is a constant that is not needed for any further calculations. Note that equations (24) and (25) are exactly those of the equations in Section 9.3.4 and 9.3.5 respectively of Chapter 4 of ACI 446-5. Performing a least-squares fit of equation (25) provides A, and is recommended by ACI 446-5 over a simple linear regression (although a linear regression is allowed). It should be noted the reasoning for this is not cited, and the author recommends that ACI 446-5 provide some explanation for using a quadratic equation over a linear one.

The far tail constant, A, can now be plugged into equation (20) to obtain W_F, and then G_F. As will be discussed in Section 2.2, A will also be used, in part, to calculate the initial portion of the softening curve, the fracture energy, and the critical crack opening displacement.

One area of contention is that should the residual load be less than that of the pre-load (the small amount of un-recorded loading before testing to eliminate seating non-linearities, usually between 5-10% of the expected peak load), there will be no initial negative *corrected* load data. Instead, the first corrected load data point will be positive. This particular circumstance was observed in specimens with a well-developed softening tail, and will be discussed further in Chapter 4. ACI 446-5 does not have any provisions for this situation, so using a value of $w_{MA} = 0$ in this case is a practical assumption given that a typical value of w_{MA} is usually between 10 to 20 microns, which is on the order of $w_{MR} \times 10^{-5}$.

Although G_F is a useful fracture parameter, it alone is not entirely sufficient in describing the post-peak behavior of concrete, as the shape of softening curve is never taken into account. It's well within the realm of possibility that two concretes with the same G_F could exhibit different post-peak behavior, and thus more parameters are needed to better describe the fracture process.

2.2 Bilinear Cohesive Crack Model

As discussed above, G_F represents the energy condition required for crack propagation and completely controls fracture when the fracture process zone is considerably smaller than the size of the specimen [Elices et al. 2002]. However, it alone is not enough to fully describe the post-peak behavior of concrete. By contrast, when the fracture process zone is large compared to size of the specimen, the tensile strength and initial slope of the softening curve begin to control several properties, such as the strength of the specimen [Elices et al. 2002]. The reason is that for relatively small specimen sizes, the peak load occurs at very small crack opening displacement values, and therefore the strength of the specimen relies entirely on the initial portion of the softening curve. Thus to better describe the post-peak behavior of concrete, a new model must be created that provides fracture parameters that also take into account the initial portion of the softening curve. Guinea et al. proposed such a model with four fracture parameters that approximate the stress vs. crack opening

displacement softening curve of concrete as bilinear, described as the bilinear cohesive crack model [Guinea et al., 1994].

As discussed in Chapter 1, ACI 446-5 uses the bilinear cohesive crack model as the basis for calculations of the fracture parameters determined from NBLII tests. The calculation of these fracture parameters are an adaptation of the equations and methods developed by Hillerborg, discussed above in Section 2.1, and by Guinea et al., discussed further below. These methods have gone through many modifications over the years, which have led to changes of several of the original equations found in the literature. In select cases, the equations listed in Chapter 4 of ACI 446-5 cannot be found in the literature. In general, the equations are also complex and in some cases sensitive to small changes, discussed further in Chapter 4, making them error-prone. Thus, careful consideration of the assumptions of each of the equations listed in ACI 446-5 is required.

The bilinear cohesive crack model developed by Guinea et al. is a simple approximation of the softening curve shown in Figure 1, where the softening curve of concrete is approximated by two linear functions, as shown in Figure 6. This bilinear approximation is completely defined by the following terms, which are represented graphically in Figure 6:

- The total fracture energy: G_F
- The splitting tensile strength: f_t
- The initial horizontal intercept: w_1
- The critical crack opening: w_c
- The initial fracture energy: G_f

The first term, G_F, is calculated from load-deformation curve data using equation (21), derived in Section 2.1. The other terms are discussed in detail below, with the initial portion of the softening curve discussed in Section 2.2.1, and the critical crack opening displacement, w_c, discussed in Section 2.2.2.

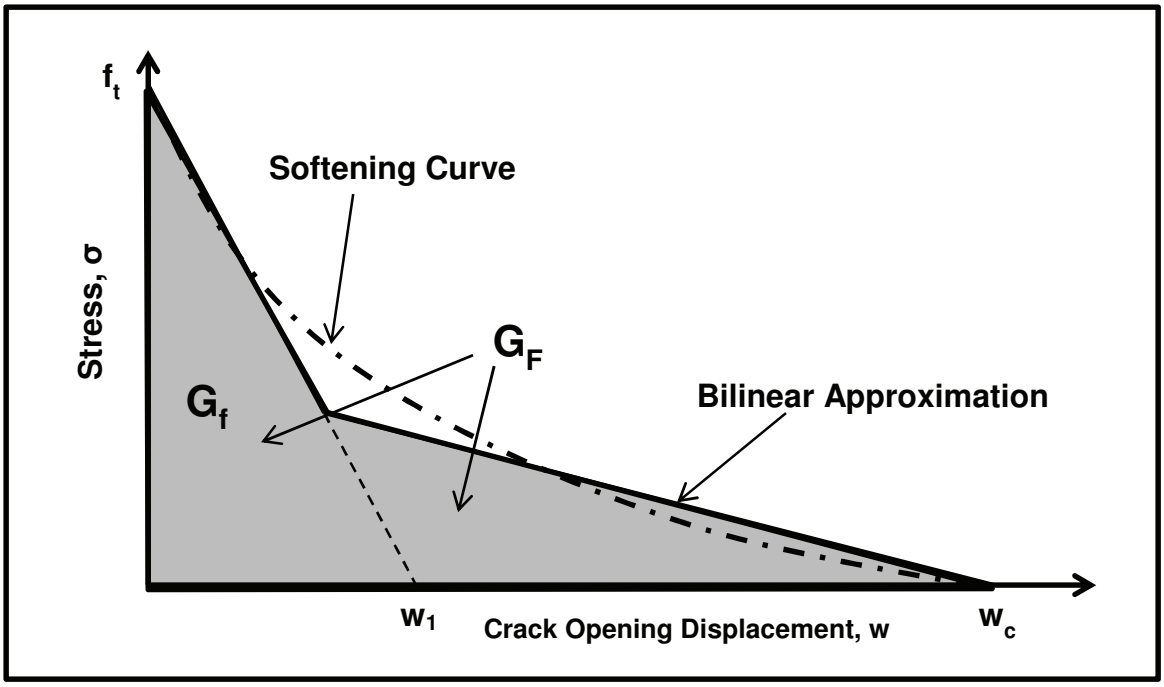

Figure 6: Bilinear approximation of softening curve

2.2.1 The Initial Portion of the Softening Curve

The term f_t, shown in Figure 6, represents the tensile strength of the concrete which is obtained from Brazilian split cylinder tests. It should be noted that the experiments and theoretical analysis performed by Rocco et al. determined that the Brazilian tests show a great deal of dependence on the size of the specimen with respect to the width of the wooden strips used along the top and bottom of the specimen [Rocco et al., 1999]. Rocco et al. also showed that f_t asymptotically approaches a minimum value as the size of the specimen becomes large compared with the width of the strips. Thus, as long as sufficiently slender strips are used, the Brazilian test provides a valid measure for the tensile strength of the concrete.

The term w_1 represents the horizontal intercept of the initial linear portion of the softening curve. As discussed above, this term, combined with f_t, can fully describe the post-peak behavior of relatively small specimens. However, it is still of interest to determine the initial fracture parameters for specimens of larger size. Thus, to describe the peak load dependence of geometrically similar specimens on their size, Elices et al. introduced another term known as the

brittleness length, l_1 [Elices et al. 2002]. l_1 is similar to the characteristic length of concrete, in that it is a material property proportional to the length of the fracture process zone, and thus can be used in adjusting the fracture parameters for specimens of larger sizes, discussed further below. Elices et al. defined l_1 as a function of w_1 and f_t by the following equation:

$$l_1 = \frac{Ew_1}{2f_t}, \tag{26}$$

where E is the elastic modulus of the material [Elices et al. 2002].

As one can see, in order to determine w_1, l_1 must first be known. Knowing that l_1 is a material property independent of specimen size, the peak load of the specimen must be a function of l_1 and the specimen geometry. We create a non-dimensional equation relating the peak load (translated to a peak stress, σ_{NU}) and the tensile strength to a characteristic dimension of the specimen (in this case, the beam depth, D). The resulting equation is:

$$\frac{\sigma_{NU}}{f_t} = \varphi\left(\frac{D}{l_1}\right), \tag{27}$$

where φ is a dimensionless function. Equation (27) can then be numerically inverted to aid in the calculation of l_1 as follows:

$$\frac{D}{l_1} = \chi\left(\frac{\sigma_{NU}}{f_t}\right), \tag{28}$$

where χ is the inverse function of φ. Solving for l_1, we get:

$$l_1 = \frac{D}{\chi(\sigma_{NU}/f_t)}. \tag{29}$$

Using inverse numerical methods, and a specific span-to-depth ratio of 4, Planas et al. determined that l_1 can be calculated explicitly through known values as the following:

$$l_1 = \kappa D\left[\frac{13.11}{(x-1)^2} + \frac{2.68}{x}\right], \tag{30}$$

where:

$$\kappa = 1 - \alpha_0^{1.45}, \quad x = \eta_0\frac{f_t}{\sigma_{NU}}, \quad \eta_0 = (1-\alpha_0)^2, \quad \text{and} \quad \alpha_0 = \frac{a_0}{D},$$

where a_0 is the notch depth [Planas et al., 1998]. Then, w_1 can then be calculated as the following:

$$w_1 = \frac{2 f_t l_1}{E}, \tag{31}$$

which is the equation in Section 9.5.2 of Chapter 4 of ACI 446-5.

However, the NBLII experimental procedures of ACI 446-5 require a span-to-depth ratio of 3, which alters the forgoing equation for l_1 slightly. Equation 4.3 of ACI 446-5, which calculates l_1, cannot be found in the literature, and thus some measure of confidence for the altered equation must be provided.

To determine the brittleness length, ACI 446-5 provides the following equation:

$$l_1 = \kappa D \left[\frac{11.2}{(x^2 - 1)^2} + \frac{2.365}{x^2} \right], \tag{32}$$

where

$$\kappa = 1 - {\alpha_0}^{1.7}, \quad x = \frac{f_t}{f_p}, \quad \text{and} \quad \alpha_0 = a_0 / D$$

The term f_p is introduced by ACI 446-5, defined as the net plastic flexural strength, and is analogous to the maximum nominal applied stress, σ_{NU}, for very small specimens. In the limiting case where l_1 is very large with respect to the beam depth, D, the beam behaves as if it were perfectly plastic in tension and rigid in compression, as shown graphically in Figure 7.

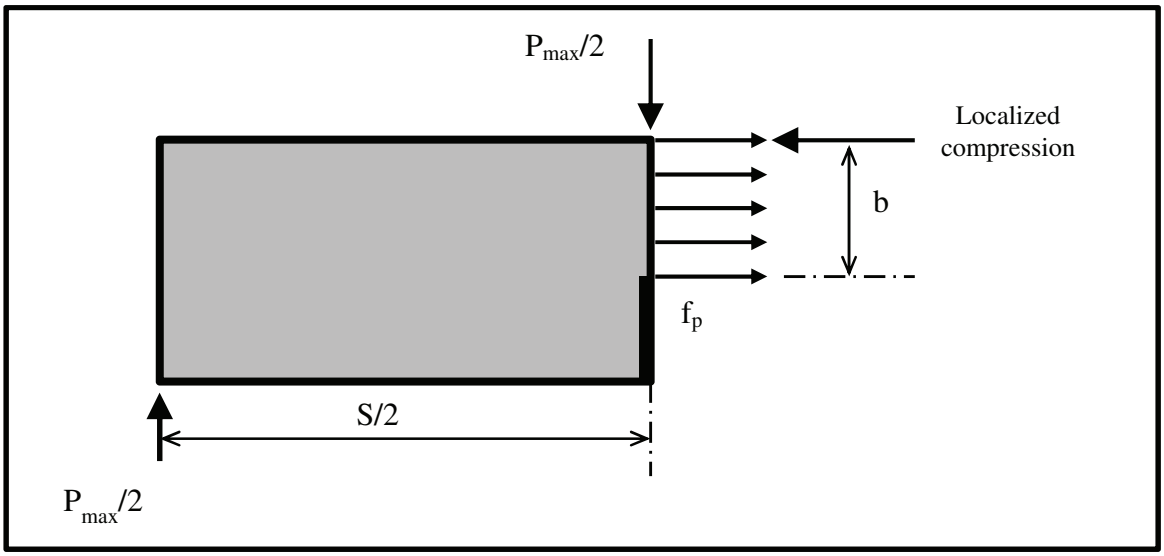

Figure 7: Graphical description of net plastic strength

Using static equilibrium and solving for f_p, we get:

$$f_p = \frac{P_{max} S}{2Bb^2} \ , \tag{33}$$

where P_{max} is the effective maximum peak load. Note that equation (33) is exactly that of Equation 4.2 in ACI 446-5.

To obtain P_{max}, we must add the corrected peak load (P_{1max} shown in Figure 5) to the residual load *excluding* any additional load to counteract the counterweights, which is P'_R shown in Figure 4. From equation (18), we know that:

$$P'_R = \frac{A}{(\delta_R - \delta_A)^2} \ , \tag{34}$$

where A is the far tail constant defined above in Section 2.1. Thus, the equation to calculate P_{max} is:

$$P_{max} = P_{1max} + \frac{A}{(\delta_R - \delta_A)^2} \ . \tag{35}$$

However, the equation in Section 9.4.1 from Chapter 4 of ACI 446-5 uses values of CMOD instead of displacement, and is as follows:

$$P_{max} = P_{1max} + \frac{A}{(w_{MR} - w_{MA})^2} \ . \tag{36}$$

The author believes that equation (36) is incorrect, as no translation from values of CMOD to displacement is included. It is possible that this was simply an oversight by ACI 446-5 due to the change of a span-to-depth ratio from 4 to 3. For S/D = 4, the term 4D/S = 1, and thus is eliminated. However, with a different S/D ratio, equation (36) becomes:

$$P_{max} = P_{1max} + \left(\frac{4D}{S}\right)^2 \frac{A}{(w_{MR} - w_{MA})^2} \ . \tag{37}$$

Equation (37) is then substituted into equation (33) to determine f_p. Note that the difference between equations (36) and (37) is not trivial (with the term $[4D/S]^2 \approx 1.8$ for S/D = 3) and the effects of this difference will be explored further in Chapter 4 of this thesis.

Knowing f_p, the brittleness length now can be determined through similar logic applied in equation (27), where f_p is normalized to f_t as a dimensionless function of l_1 and D as follows:

$$\frac{f_p}{f_t} = \varphi\left(\frac{D}{l_1}\right) \tag{38}$$

Once again, inverse numerical methods are needed to determine l_1 explicitly as a function of f_p. An email correspondence with Dr. Jaime Planas of the Universidad Politéncia de Madrid gave some insight as to how the equation shown in ACI 446-5 was determined using inverse numerical methods, which are outside the scope of this thesis. Therefore, a finite element code modeling a notched beam under center-span loading with a span-to-depth ratio of 3 developed by Dr. Walter H. Gerstle of the University of New Mexico was run to provide a measure of confidence of Equation 4.3 of ACI 446-5,. For simplicity, the program creates a half-beam, utilizing symmetry, and translates the beam mesh into a super-element, retaining nodes only along the crack face, top, and at the support, shown in Figure 8. Nodal displacements are then applied at the top of the beam above the notch, and using non-linear Newton-Rhapson iteration the element is solved to calculate stresses and displacements at each node, from which P_{max} can be determined.

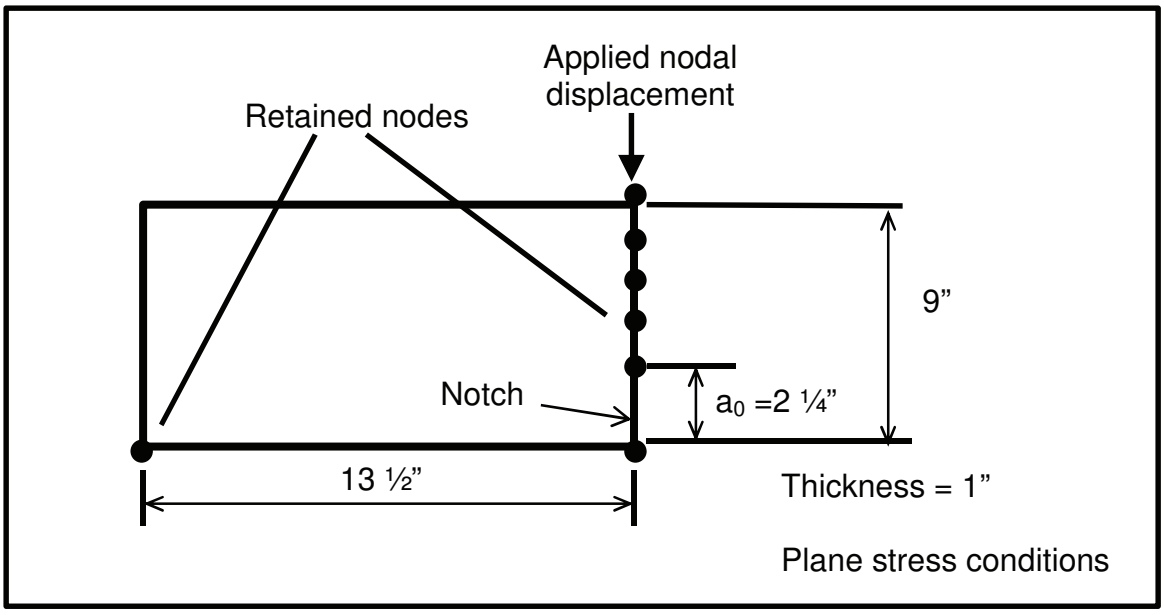

Figure 8: Sketch of half-beam FEM

Figure 9 shows values calculated by the program during its first iterations for, in this case, a 29X29 element half-beam mesh, and Figure 10 shows the final values for the same beam.

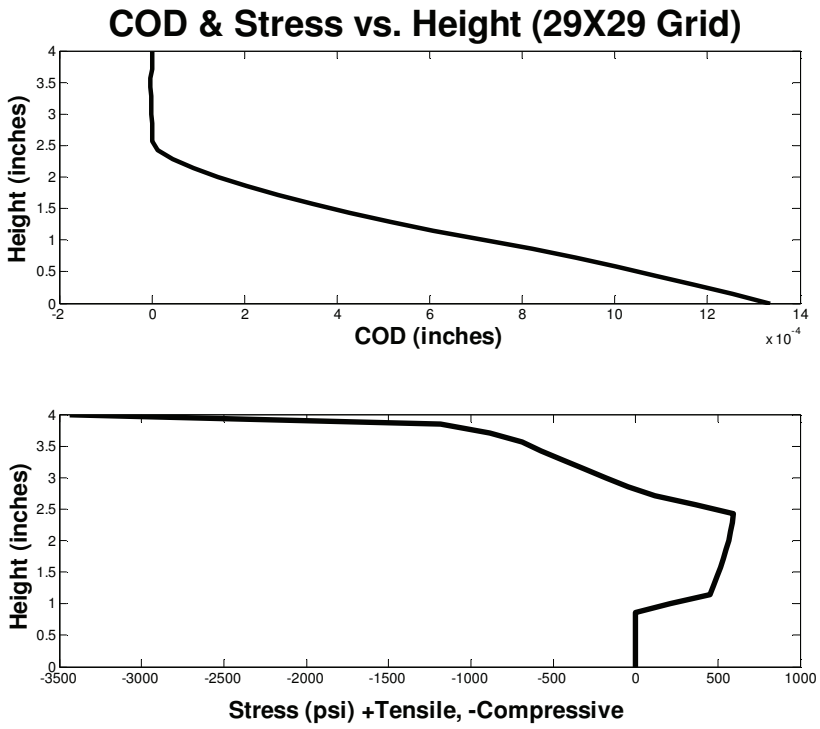

Figure 9: COD opening and cohesive stresses at start of program

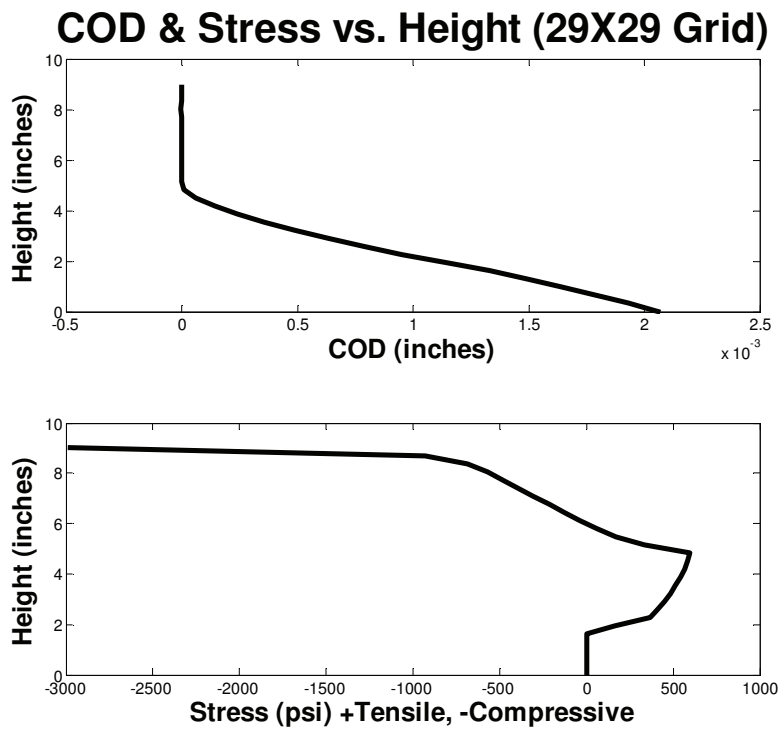

Figure 10: COD opening and cohesive stresses at end of program

As expected, the crack opening, calculated as twice the horizontal displacement from the node at the top of the notch, grows as larger displacements are applied. The stress profile also takes a reasonable shape and, as expected, the point of maximum stress occurs upwards along the notch tip with further iteration.

Once a solution has converged on P_{max}, the brittleness length is then calculated for several different depths, and plots of the normalized process zone length, l_1/D, versus the normalized strength, f_p/f_t, are created and compared to values using the Equation 4.3 of ACI 446-5. The program was run several times for different mesh sizes, and some measure of confidence can be provided so long as finer meshes appear to converge on Equation 4.3 of ACI 446-5. Lastly, Figure 11 shows the normalized curves for the solutions calculated by the program for several different sized meshes, where the rows and columns of elements of each mesh are specified.

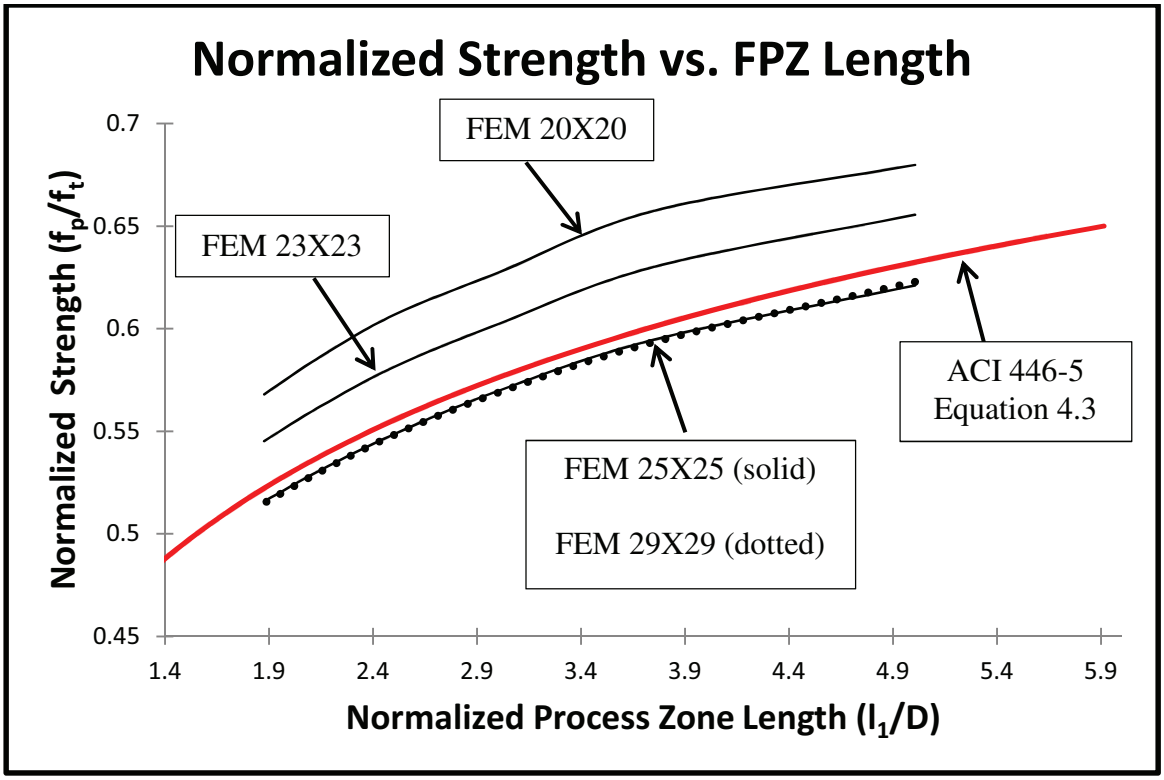

Figure 11: Comparison of FEM analysis to ACI equation

Unfortunately, processing time for the calculations became exponentially longer as the meshes became finer, and thus a grid of 29X29 elements was the

finest mesh that the computer available could handle. However, it is seen as the meshes get finer that the results appear to converge very close to the equation given by ACI 446-5. Although this should not be used as a definitive or exclusive measure of provenance, it does show that the equation is realistic and conforms to conventional fracture mechanics theory.

Lastly, the modulus of elasticity, E, must be calculated before w_1 can be determined. While the modulus of elasticity can be determined through standardized tests of concrete cylinders, it can also be determined from the initial linear portion of the load-CMOD curve. This is desirable, as the casting of additional cylinders for modulus of elasticity tests is then unnecessary. The calculation of E can be determined through some straight-forward manipulations of equations provided by the work of Guinea et al., recounted below [Guinea et al., 1998]. Guinea et al. showed the relationship between CMOD and E as follows:

$$w_M = \frac{4\sigma_N a_0}{E} V_1(\alpha) \ , \tag{39}$$

where w_M is the CMOD as a function of the maximum applied stress, σ_N, at center span of the beam, a_0 is the notch depth, and $V_1(\alpha)$ is function representing the geometry of the beam, specified as:

$$V_1(\alpha) = 0.8 - 1.7\alpha + 2.4\alpha^2 + \frac{0.66}{(1-\alpha)^2} + \frac{4D}{S}(-0.04 - 0.58\alpha + 1.47\alpha^2 - 2.04\alpha^3) \ , \tag{40}$$

where S is the span length and $\alpha = a_0/D$ [Guinea et al. 1998].

Using statics analysis of a three-point bend beam, the maximum applied stress is related to the applied center-span point load, P, as follows:

$$\sigma_N = \frac{3PS}{2BD^2} \ , \tag{41}$$

where B is the width of the beam. Substituting equation (41) into equation (39), the expression for w_M becomes:

$$w_M = \frac{6PSa_0}{BD^2E} V_1(\alpha) \ . \tag{42}$$

Finally, solving for E we get:

$$E = \frac{6Sa_0}{C_i BD^2} V_1(\alpha) \ , \tag{43}$$

where C_i is the initial compliance of the specimen, defined as w_M/P for the initial linear portion of the load-CMOD curve, shown in Figure 12. To determine C_i, Section 9.2.1 and 9.2.2 of Chapter 4 of ACI 446-5 states that data from the initial linear segment of the load-CMOD curve be taken to determine the compliance, using data values between 15 and 55% of the recorded maximum peak load, P_{max} [ACI, 2010]. A plot of CMOD vs. P is then created for said initial values, and the compliance is determined as the slope of the function as follows:

$$C_i = \frac{\Delta(CMOD)}{\Delta P}, \tag{44}$$

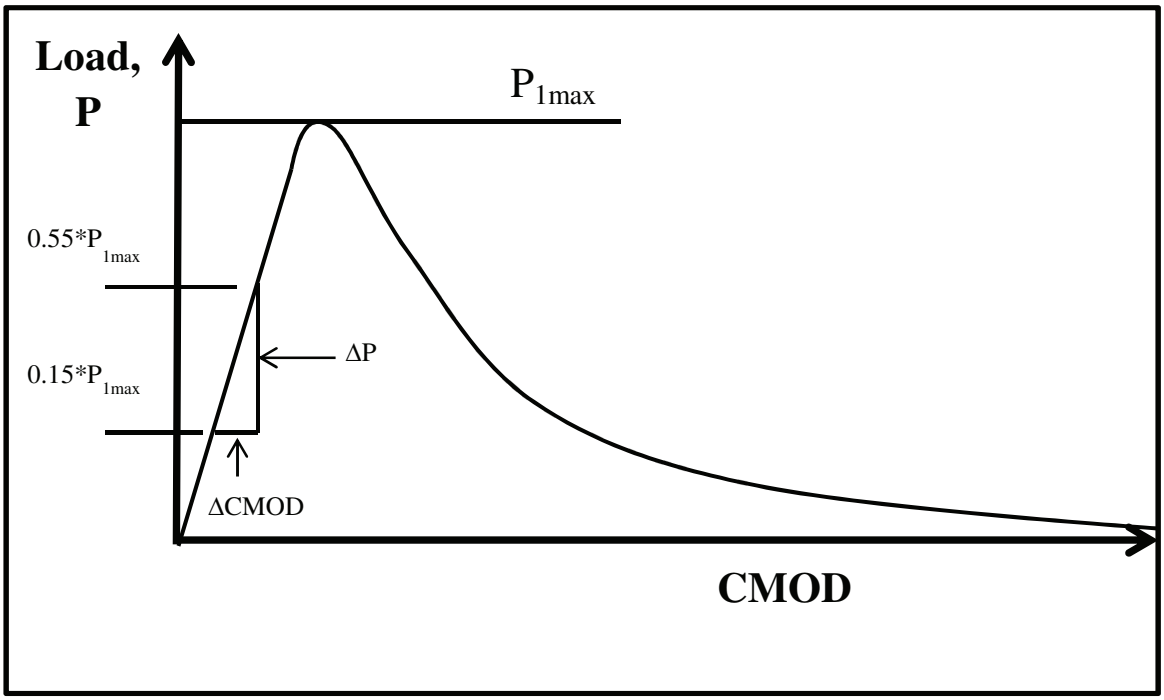

Figure 12: Initial compliance taken from the linear portion of the curve.

Finally, equation (44) is slightly modified to include the depth of the knife edges used to hold the clip gauges in places as follows:

$$E = \frac{6Sa_0}{C_i BD^2} V_1(\alpha_0') \ , \tag{45}$$

where α'_0 is:

$$\alpha_0' = \frac{a_0 + h}{D + h}, \tag{46}$$

where h is the thickness of the knife edges, or the distance from the measured CMOD to the specimen surface. Note that equations (45) and (46) are exactly that of the equations listed in Section 9.2.3 in Chapter 4 of ACI 446-5.

Thus, with l_1 and E known, the initial horizontal intercept, w_1, can now be calculated using equation (31).

2.2.2 The Critical Crack Opening Displacement

The last point on the softening curve, w_c, is calculated using the geometric configuration of the bilinear approximation. By introducing a new term representing the abscissa of the center of gravity of the area under the bilinear approximation, w_G, the full approximation of the bilinear curve can be defined and will allow us to solve for w_c. Figure 13 (a) shows a graphical representation of w_G and where it lies on the stress-COD softening curve.

Using the geometry shown in Figure 13 (b), we can relate the crack opening displacement, w, to any distance, z, from the top of the beam through the following equation:

$$w = 2\theta z \ , \tag{47}$$

where θ is assumed to be small (i.e. sin θ ≈ θ.)

Following similar logic to that employed in equation (3), the resultant tensile force of the cohesive zone is as follows:

$$T = \int_0^d \sigma\big(w(z)\big)\, dz \ , \tag{48}$$

where d is the depth of the notched cross-section. Then, summing moments about point O, we get:

$$\frac{PS}{4} = B \int_0^d \sigma\big(w(z)\big)\, z\, dz \ , \tag{49}$$

where B is the width of the beam. Substituting values of w for z and solving for P we get:

$$P = \frac{B}{S\theta^2} \int_0^{w_n} \sigma(w)\, w\, dw \ , \tag{50}$$

where w_n is the crack opening displacement at the initial notch tip.

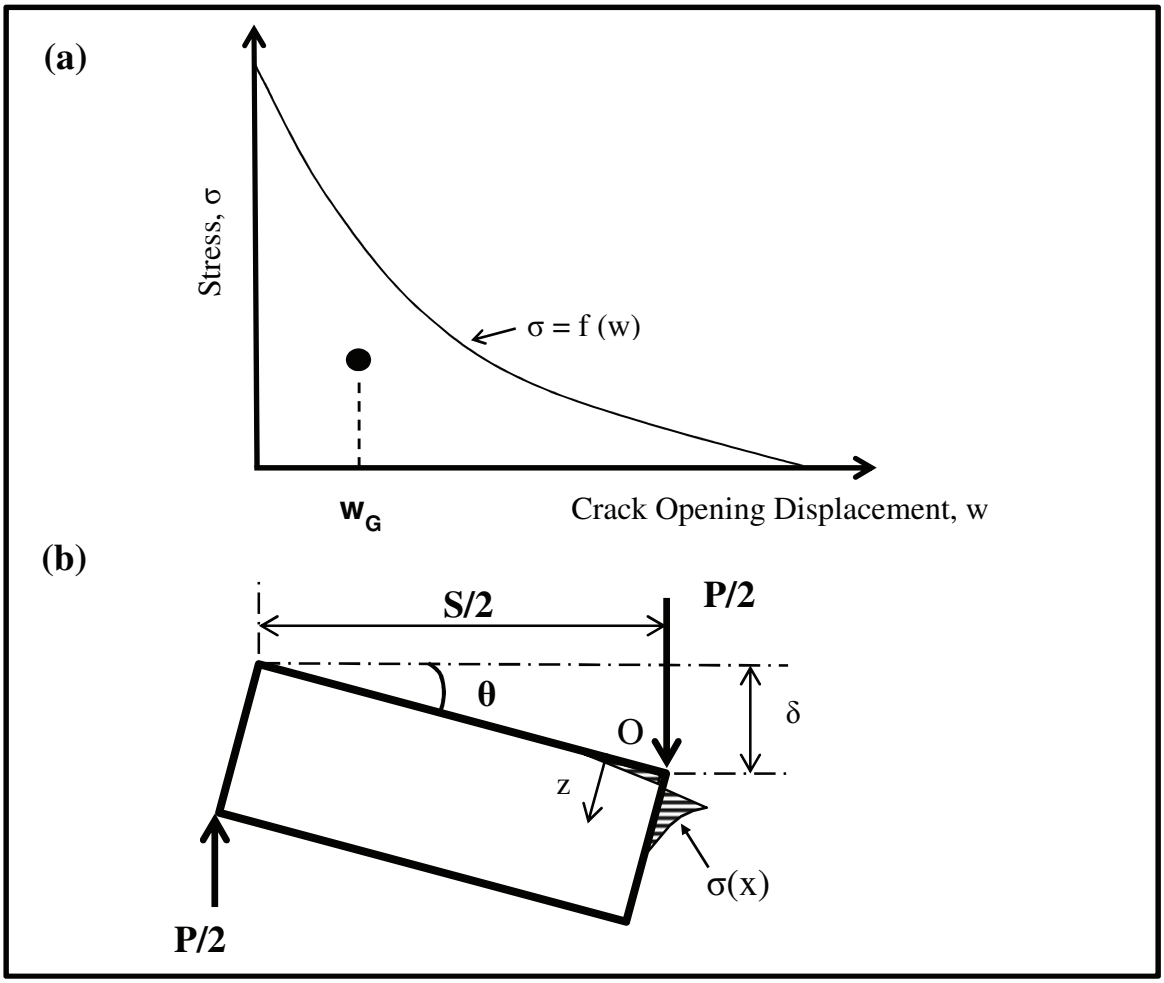

Figure 13: a) Abscissa of the center of gravity of the area under the σ-COD curve, b) free-body diagram of the half-beam section

When $w_n > w_c$ (i.e. after the full softening function has been developed), by the definition of center of gravity, we know w_G from the graph in Figure 13 (a) is the following:

$$w_G = \frac{\int_0^{w_n} \sigma(w)\, w\, dw}{\int_0^{w_n} \sigma(w) dw} \ . \tag{51}$$

Also, knowing that G_F is the area under the stress-COD curve, or:

$$G_F = \int_0^{w_n} \sigma(w) dw \ , \tag{52}$$

we can conclude that by multiplying w_G and G_F we get:

$$G_F w_G = \int_0^{w_n} \sigma(w) w \, dw \ , \tag{53}$$

and thus, substituting equation (53) into equation (50), we get:

$$P = \frac{B G_F w_G}{S\theta^2} \ . \tag{54}$$

Recall from Figure 3 (a) that θ can be related to the displacement δ by the following equation:

$$\theta = \frac{2\delta}{S} \ , \tag{55}$$

and thus substituting equation (55) into equation (54), we get:

$$P = \frac{BSG_f w_G}{4\delta^2} \ . \tag{56}$$

Then, substituting equation (17) for P, we get:

$$\frac{A}{(\delta - \delta_A)^2} + P'_0 = \frac{BSG_f w_G}{4\delta^2} \ . \tag{57}$$

Since P'_0 is very small (assuming perfect weight compensation), it along with δ_A can be neglected. Then finally, solving for w_G, we get:

$$w_G = \frac{4A}{BSG_F} \ , \tag{58}$$

which is the equation in Section 9.7.1 of Chapter 4 of ACI 446-5.

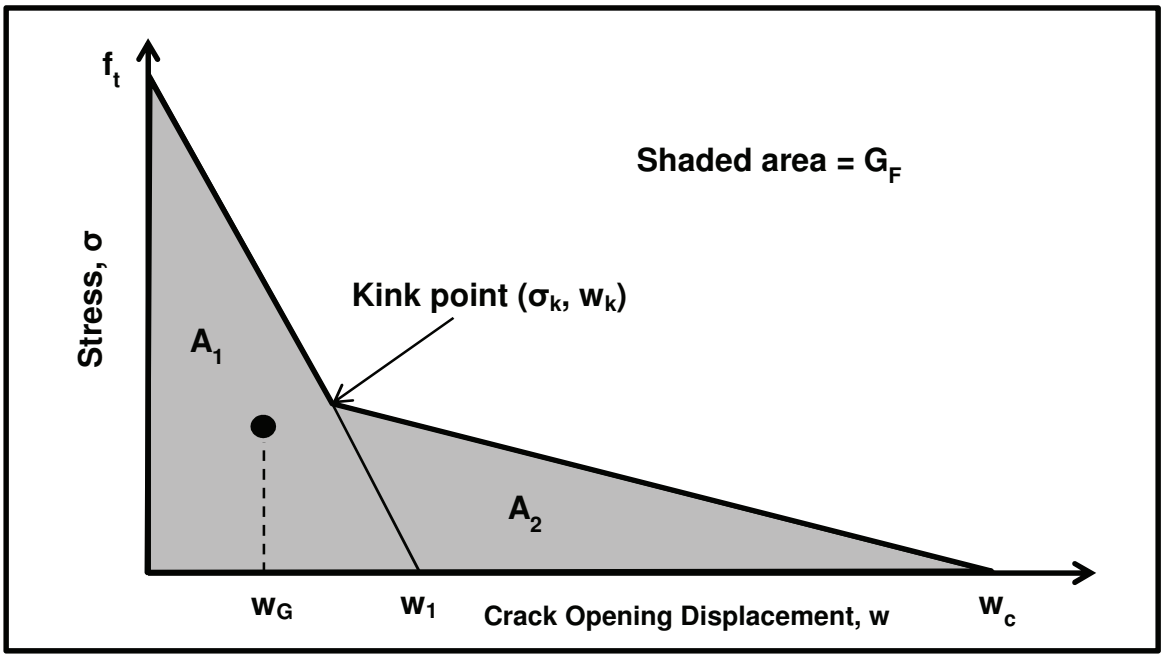

Figure 14: Geometry of the bilinear approximation

Knowing w_G, w_1 and G_F it is now possible to calculate w_c using the geometry of the bilinear approximation, shown in Figure 14, where A_1 represents the area of the initial linear portion of the softening curve (defined in Figure 6 as the initial fracture energy, G_f) and A_2 is the remaining area, so that $A_1 + A_2 = G_F$.

The geometry of Figure 14 is defined entirely by the following equations, representing the linear equations of the initial and tail sections of the bilinear approximation:

$$\begin{aligned} \sigma &= f_t\left(1-\frac{w}{w_1}\right) \quad , \qquad \text{for } 0 \le w \le w_k \\ \sigma &= \sigma_k\left(\frac{w-w_c}{w_k-w_c}\right) \quad , \quad \text{for } w_k \le w \le w_c \\ \sigma &= 0 \quad , \qquad\qquad \text{for } w > w_c \quad , \end{aligned} \tag{59}$$

where w_k and σ_k are the COD and stress coordinates respectively of the kink point. Knowing these coordinates, the areas can be found through simple geometry as follows:

$$A_1 = \frac{f_t w_1}{2} \text{ and } A_2 = \frac{\sigma_k(w_c - w_1)}{2} \ . \tag{60}$$

Then, knowing that G_F is the sum of A_1 and A_2, we get:

$$G_F = \frac{f_t w_1}{2} + \frac{\sigma_k(w_c - w_1)}{2} \ . \tag{61}$$

Solving for σ_k and simplifying algebraically, we get:

$$\sigma_k = f_t \frac{2G_F/f_t - w_1}{w_c - w_1} \ . \tag{62}$$

It should be noted that section 9.8.2 of Chapter 4 of ACI 446-5 introduces a simplifying term, known as the characteristic crack opening, $w_{ch} = G_F/f_t$, which has units of length. Inserting w_{ch} into equation (62), we get:

$$\sigma_k = f_t \frac{2w_{ch} - w_1}{w_c - w_1} \ , \tag{63}$$

which is the equation in Section 9.8.4 of Chapter 4 of ACI 446-5

Next, equation (63) can be substituted into the top expression of equation (59) to obtain the following:

$$f_t\left(1-\frac{w_k}{w_1}\right) = f_t \frac{2w_{ch} - w_1}{w_c - w_1} \ . \tag{64}$$

Solving for w_k, we get:

$$w_k = w_1 \frac{w_c - 2w_{ch}}{w_c - w_1} \quad , \tag{65}$$

which is the equation in Section 9.8.5 of Chapter 4 of ACI 446-5.

The last unknown is the critical crack opening displacement, which can be found by utilizing the definition of w_G. The abscissa of the center of gravity of the geometry shown in Figure 14 is defined as:

$$w_G = \frac{A_1 w_{GA1} + A_2 w_{GA2}}{A_1 + A_2} \quad , \tag{66}$$

where w_{GA1} and w_{GA2} are the abscissa of the center of gravity of areas A_1 and A_2 respectively, represented by dots in Figure 15 . Using this geometry, w_{GA1} and w_{GA2} are as follows:

$$w_{GA1} = \frac{w_1}{3} \quad \text{and} \quad w_{GA2} = \frac{w_k + w_1 + w_c}{3} \quad . \tag{67}$$

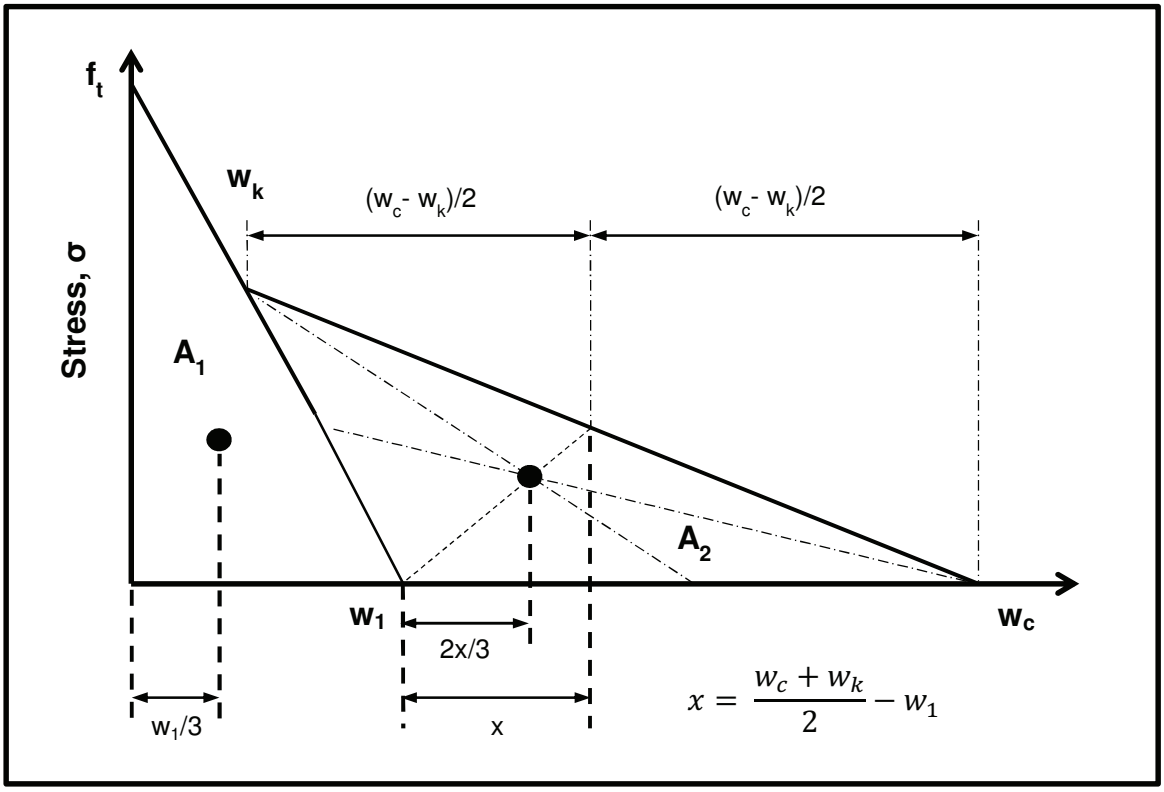

Figure 15: Geometry of the center of gravity of areas A_1 and A_2 (not to scale)

Then, substituting A_1 and A_2 from equation (60) and w_{GA1} and w_{GA2} from equation (67) into equation (66), and knowing $G_F = A_1 + A_2$, we get:

$$w_G = \frac{f_t {w_1}^2 + \sigma_k (w_c - w_1)(w_k + w_1 + w_c)}{6G_F} \quad . \tag{68}$$

Then, by substituting σ_k and w_k from equations (63) and (65) respectively into equation (68), and w_{ch} for G_F/f_t we get:

$$w_G = \frac{{w_1}^2 + (2w_{ch} - w_1)\left(w_1 \frac{w_c - 2w_{ch}}{w_c - w_1} + w_1 + w_c\right)}{6w_{ch}} \quad . \tag{69}$$

Equation (69) can then be arranged into a binomial format, which can then be solved for w_c. It should be noted that the algebra required to do this is not trivial, and thus many steps are omitted for the sake of brevity. The binomial rearrangement of equation (69) is as follows:

$$w_c^2 - w_c \frac{6w_G(w_{ch}) - 2w_1(w_{ch})}{2(w_{ch}) - w_1} + \frac{6w_G w_1(w_{ch}) - 4w_1(w_{ch})^2}{2(w_{ch}) - w_1} = 0 \quad , \tag{70}$$

which is the same equation provided in the work by Guinea et al. [Guinea et al., 1994]. The quadratic equation can now be used to solve for the roots of w_c in equation (70) using the following:

$$w_c = -b + \frac{\sqrt{b^2 - 4ac}}{2a} \quad , \tag{71}$$

where:

$$a = 1 \quad ,$$

$$b = \frac{6w_G(w_{ch}) - 2w_1(w_{ch})}{2(w_{ch}) - w_1} \quad \text{and} \tag{72}$$

$$c = \frac{6w_G w_1(w_{ch}) - 4w_1(w_{ch})^2}{2(w_{ch}) - w_1}$$

Note that we are only interested in the positive root, as w_c must be positive. By substituting the parameters from equation (72) into equation (71), we can get an exact expression for w_c with known values. Once again, the algebraic simplification is not trivial, and for the sake of brevity many steps have been omitted. After simplifying, we get the following:

$$w_c = w_{ch}\frac{3w_G - w_1}{2w_{ch} - w_1}\left[1 + \sqrt{1 - \frac{2w_1(3w_G - 2w_{ch})(2w_{ch} - w_1)}{w_{ch}(3w_G - w_1)^2}}\right] \quad , \tag{73}$$

which is the equation in Section 9.8.3 of Chapter 4 of ACI 446-5.

With w_c calculated exclusively using previously determined parameters, it is now possible to calculate the kink point coordinates using equations (63) and (65), and the bilinear approximation is then completely defined. Knowing the four parameters defining the bilinear approximation of the cohesive curve, it should now be possible to replicate the original test data (P vs. δ and P vs. CMOD) using a nonlinear finite element analysis. This is advisable, given the complexity of the foregoing inverse analysis procedure, and the many approximations that have been made. Knowing the derivation and background of the equations to calculate the fracture parameters of the bilinear cohesive crack model, we can now explore the experimental procedures of the notched beam tests, discussed next in Chapter 3.

3 NOTCHED BEAM TESTS

One of the purposes of ACI 446-5 is to provide a relatively simple and reliable way of determining key fracture parameters of concrete in what it describes as “Notched Beam Level II (NBLII)” testing of concrete [ACI, 2010]. The NBLII testing procedure requires that notched concrete beams are placed under three-point bending and run under closed-loop CMOD control. During the course of the experiment, load, CMOD and load point displacement (LPD) are recorded versus time. From this data, fracture parameters of the bilinear cohesive crack model can then be determined. A graphical depiction of the test setup and control system is shown in Figure 16.

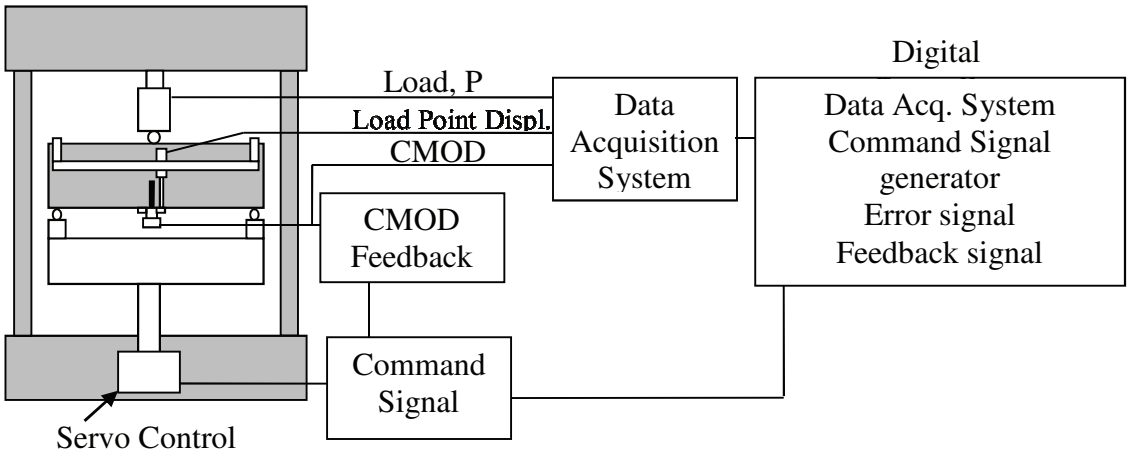

Figure 16: Schematic of Test Setup and Control System [ACI, 2010]

Following Chapter 2 of ACI 446-5, NBLII tests were performed on beams of three different sizes. In the remainder of this chapter, Section 3.1 discusses the specimen properties, Section 3.2 discusses the test setup, Section 3.3 discusses the loading procedure, and Section 3.4 reports the results from the experiments.

3.1 Specimen Properties

Specimens for the NBLII tests were cast in accordance with ASTM C192 “Practice for Making and Curing Concrete Test Specimens in the Laboratory” as

required by Chapter 2 of ACI 446-5. Section 3.1.1 discusses the concrete characterization, and Section 3.1.2 discusses the specimen geometries.

3.1.1 Concrete Characterization

All concrete specimens were cast on March 15th, 2010 with concrete mix proportions to achieve an expected 28 day compressive strength, f'_c, of 28 MPa. Table 1 shows the concrete mix proportions

Table 1: Concrete mix design

Ingredient	Amount / yd^3
Rio Grande type I/II cement	566 lbs.
SRMG Class F Fly Ash	168 lbs.
Placitas Fine Aggregate	960 lbs.
Placitas Coarse Aggregate #6	1067 lbs.
Placitas Coarse Aggregate #8	640 lbs.
Water	270 lbs.
BASF Glenium Superplasticizer	58 oz.
Air entrainer	34 oz.

Target Slump:	3 in.
Water/Cementitious Ratio:	0.37

The specimens were cast in two separate batches due to limited size of the concrete mixer. Twelve beams were cast for notched beam testing, along with eight 4" diameter cylinders to determine the compressive and splitting tensile strength of the concrete. Figure 17 shows the concrete being mixed on the day of casting, Figure 18 shows the slump of the concrete, and Figure 19 shows the casting of the beam specimens.

Figure 17: Mixing of concrete, day of casting

Figure 18: Concrete slump on day of casting

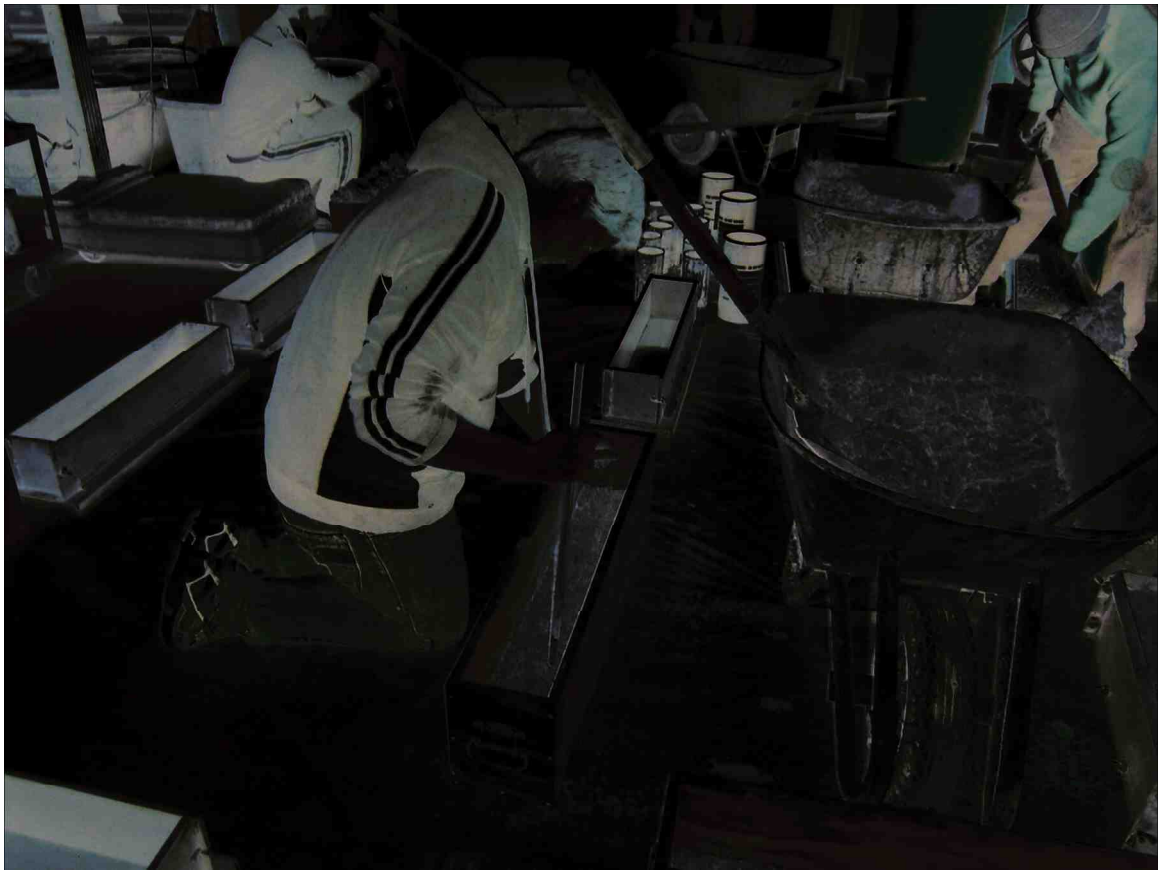

Figure 19: Casting of beam specimens

Compressive strength tests were performed after 100 days of moist curing on the first batch of concrete in accordance with the ASTM C39 / C39M - 10 “Standard Test Method for Compressive Strength of Cylindrical Concrete Specimens” specifications. Under ideal circumstances, compressive strength tests would be performed for both batches. However, to conserve cylinder specimens, compressive tests were only performed on the first batch of concrete. The parameters of the cohesive crack model do not require the compressive strength, and thus learning the compressive strength of the concrete is only a curiosity, not a necessity. Table 2 shows the compressive strength of three 4” diameter cylinders taken from the first batch of concrete, their average strength, and standard deviation. It is assumed that the second batch of the same mix proportions had similar compressive strength properties.

Table 2: Concrete compressive strength

Sample	f'c (psi)
S1	5756
S2	5016
S3	5774
Average	5515
Standard Deviation	432.7

The splitting tensile strength of the concrete, f_t, of both batches was also tested after 100 days of moist curing in accordance with ASTM C496 / C496M - 04e1 "Standard Test Method for Splitting Tensile Strength of Cylindrical Concrete Specimens" specifications. Figure 20 and Figure 21 show the split specimens from the first batch of concrete.

Figure 20: Splitting tensile test specimen

Figure 21: All splitting tensile specimens from Batch 1

Wooden loading strips ½" wide were used between the loading plate and the cylinders. For the 4" cylinders, it is assumed that the wooden loading strips were sufficiently slender in comparison to the cylinder diameter to assure minimization of size effect on the results, as discussed in Chapter 2. Table 3 shows the splitting tensile strength of both batches. It should be noted that the third sample for Batch 1 was unavailable due to a miscalculation of the amount of concrete needed for a third sample.

Table 3: Concrete splitting tensile strength

Batch 1

Sample	f_t (psi)
S1	399.0
S2	548.5
S3	N/A
Average	473.7
Standard Deviation	105.7

Batch 2

Sample	f_t (psi)
S1	406.1
S2	514.8
S3	594.6
Average	505.2
Standard Deviation	94.59

3.1.2 Specimen Dimensions

ACI 446-5 test requires that the specimens conform to a specific geometry based upon the depth of the specimen. The geometry of the beams is specified in Figure 22.

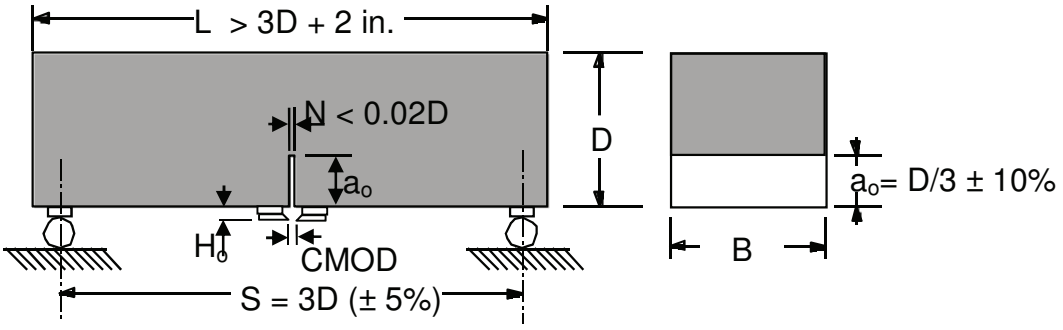

Figure 22: Specimen geometry, Figure 2.1 ACI 446-5 [ACI, 2010]

The total length, L, of the specimen must be larger than the span length, S, to accommodate room for the supports, as well as room to attach counterweights. According to Section 7.3.3 of Chapter 2 of ACI 446-5, to prevent unstable failure before the end of the test, counterweights are to be placed to create a small negative bending moment at mid-span, M, such that $WS/32 < M < WS/16$, where S is the span length and W is the total weight of the specimen [ACI, 2010]. ACI 446-5 provides guidance for selecting the total length of the specimen, which is detailed in Figure 23. Figure 23 (a) shows the specimen dimensions required when using the beam's self-weight as a counterweight, while Figure 23 (b) shows specimen dimensions when using attached counterweights, where W_c represents the weight of a counterweight, and Q represents the distance from the support to the center of gravity of the counter weight.

For specimens requiring counterweights, calculations were made on the day of testing to assure the placement of the counterweights created a negative moment at the center of the beam within the range specified above in Section 7.3.3 of Chapter 2 of ACI 446-5. This procedure is discussed further in Section 3.2.2.

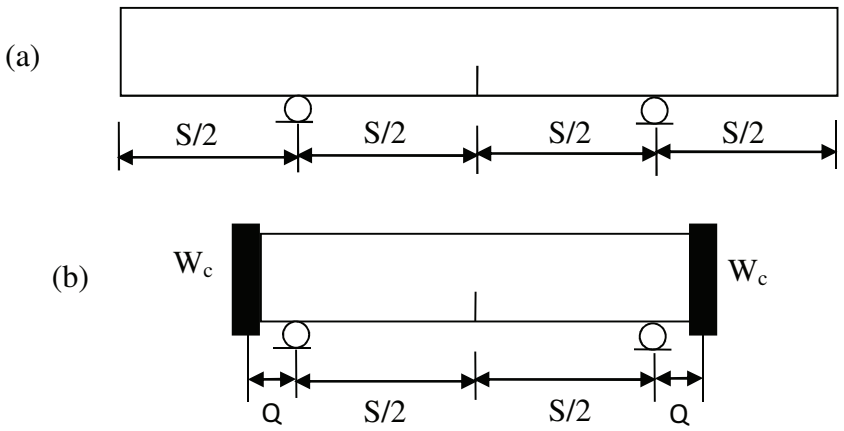

Figure 23: Counterweight system for a.) self-weight; b.) attached counterweights, Figure 2.5, ACI 446-5 [ACI 2010]

As discussed in Section 3.1.1, twelve beam specimens were cast in three different sizes, with four beams per size. Their nominal dimensions are listed in Table 4.

Table 4: Nominal beam dimensions

Beam Group	Depth (mm)	Width (mm)	Length (mm)	Span (mm)	a_0 (mm)	Notch Width (mm)
D3	76.2	152.4	558.8	228.6	25.4	2.54
D6	152.4	152.4	762.0	457.2	50.8	2.54
D9	228.6	152.4	889.0	685.8	76.2	2.54

It should be noted that the author believes there was an oversight in Figure 2.5 of ACI 446-5 regarding the suggested dimensions in Figure 23. Note that the total length of the specimens in Beam Group D3 should be 2S, or 457.2 mm. However, a uniform specimen with the total length twice the span length would create zero moment in the middle of the beam, instead of the negative moment that is required. Thus, the specimens were cast with a slightly longer total length of 558.8 mm to create the required negative bending moment in the middle of the beam conforming to Section 7.3.3 of Chapter 2 of ACI 446-5.

After the beams in group D3 had cured, they were weighed to assure that an appropriate negative moment would be achieved during testing. It should also be noted that notch width of Beam Group D3 does not conform to ACI 446-5

specifications in Section 6.3.6 of Chapter 2, where the required saw blade maximum width is 0.02*D, or 1.52 mm. The actual notch was 2.54 mm wide, as it was the thinnest concrete blade available. It should be noted, however, that this requirement is not explained or referenced. It could prove useful to relax this requirement for the testing of smaller beam sizes.

Lastly, measurements of the cross-sectional dimensions were taken once testing had been completed, as the dimensions of interest are along the cracked cross-section. Section 8.3.2 of Chapter 2 of ACI 446-5 requires four measurements of each dimension to be taken to the nearest 0.1 mm; two measurements from each half of the beam. For these experiments, a digital caliper with a precision of 0.01 mm was used to take all the measurements of the cracked beam cross-sections. The four measurements were then averaged, and are shown in Table 5 for each beam group. The naming convention for each specimen shows which concrete batch, and which sample from each batch (e.g. B1S1 represents Sample 1 of Batch 1.) Figure 24 shows an example of the locations of two measurements for notch depth on one half of a cross section of a specimen after testing.

Table 5: Average measured beam dimensions

Beam Group D3

Specimen	Depth (mm)	Width (mm)	a_0 (mm)
B1S1	77.43	154.12	25.53
B1S2	77.22	154.91	24.43
B2S1	76.77	155.05	24.80
B2S2	76.96	156.65	24.46

Beam Group D6

Specimen	Depth (mm)	Width (mm)	a_0 (mm)
B1S1	154.55	155.56	49.88
B1S2	152.97	157.69	49.14
B2S1	153.37	153.45	49.10
B2S2	151.35	154.33	49.17

Beam Group D9

Specimen	Depth (mm)	Width (mm)	a_0 (mm)
B1S1	231.85	151.28	80.11
B1S2	228.50	151.48	78.76
B2S1	231.39	151.28	80.40
B2S2	233.41	152.12	80.99

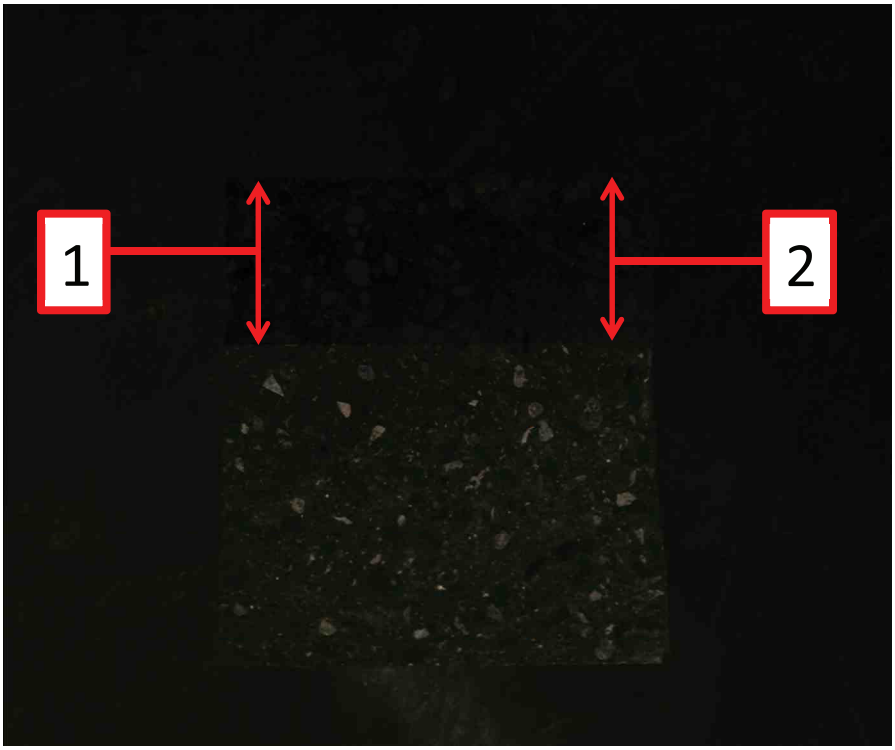

Figure 24: Example of the location of measurements taken for notch depth, a_0, in two places on one half of the fractured cross-section. Two more measurements were then taken on the other half, totaling four measurements.

3.2 Test Setup

The test setup requires that the beams be placed under three-point bending with CMOD control for the duration of the entire test, as shown in Figure 16. The test setup elements fall into two broad categories: those needed for the support system, and those needed to record the measurements of LPD, CMOD, and load for the duration of the test. Previous experimentation performed by Larry Lenke at the University of New Mexico using the NBLII tests had only used specimens 152 mm deep, and thus this experimental program required the manufacture of several new elements for the test setup. Section 3.2.1 discusses the loading apparatus and support system, Section 3.2.2 discusses the development of the counterweight system, Section 3.2.3 discusses the development of the reference frame to hold the LVDTs, and Section 3.2.4 discusses the final specimen preparation prior to testing, including the notching of the beams and the clip gauge placement.

3.2.1 Loading Apparatus and Support System

Figure 25 shows a graphical representation of the beam placed in the testing apparatus upon the supports.

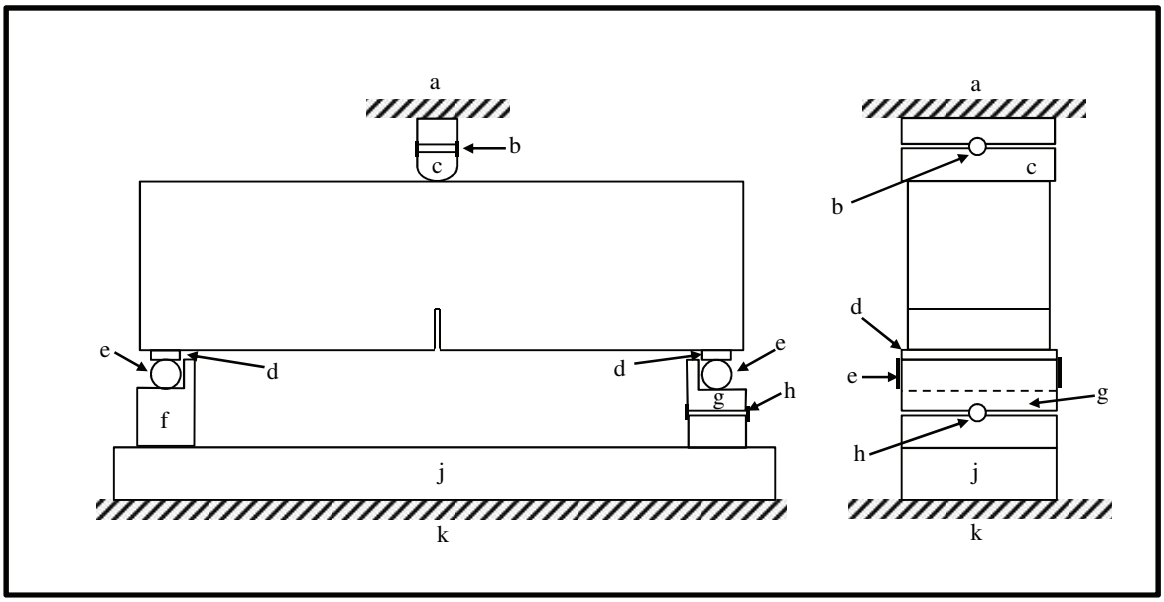

Figure 25: Sketch of loading apparatus, Figure 1.2 ACI 446-5 [ACI 2010]

The points of interest in Figure 25 are as follows: (a) load cell; (b) hardened steel shaft; (c) rotating loading block; (d) hardened steel bearing plates; (e) hardened steel rollers; (f) fixed support; (g) rotating support; (h) hardened steel shaft; (j) stiff steel beam; (k) machine frame. It is important to note that one of the supports is free to rotate in both lateral and transverse directions to minimize torsional forces. The rollers and support surfaces are also machined so that frictional forces are minimized. The parts listed in Figure 25, with the exception of the stiff steel beam in Figure 25 (j), were previously manufactured by Larry Lenke, and used in prior NBLII tests that were not part of this experimental program.

A new support beam was manufactured to accommodate the different sizes of beams and span lengths, as the previous support beam only had bolt holes for the supports in one position, used for the 152 mm (6 in.) deep specimens. The new support beam was taken from a section of W6X16 Steel beam, 48” in length, and had markings scored on the top flange to accommodate

the supports at the three required span lengths. Figure 26 shows a photograph of the support beam and Figures 27 through 29 show each different beam size resting upon the supports.

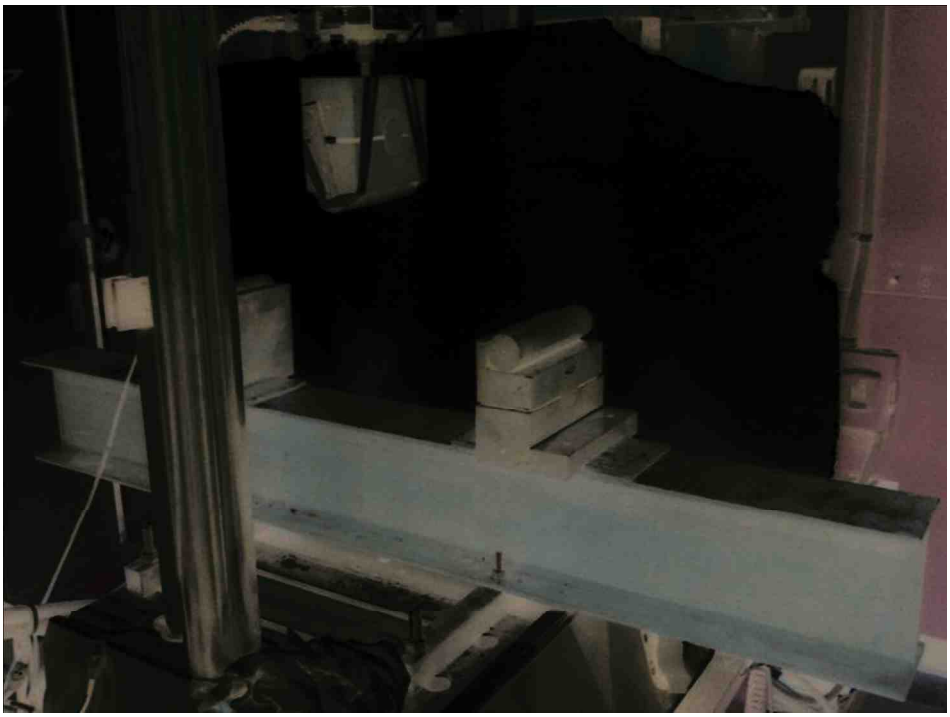

Figure 26: Photograph of support beam

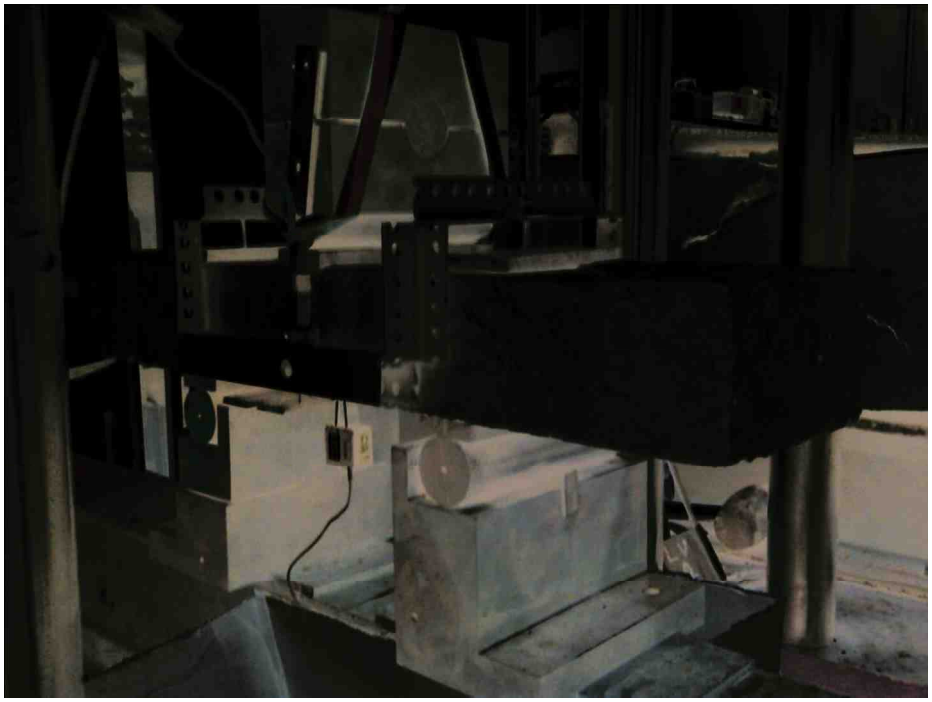

Figure 27: Setup for 76 mm (3 in) deep beam

Figure 28: Setup for 152 mm (6 in) deep beam

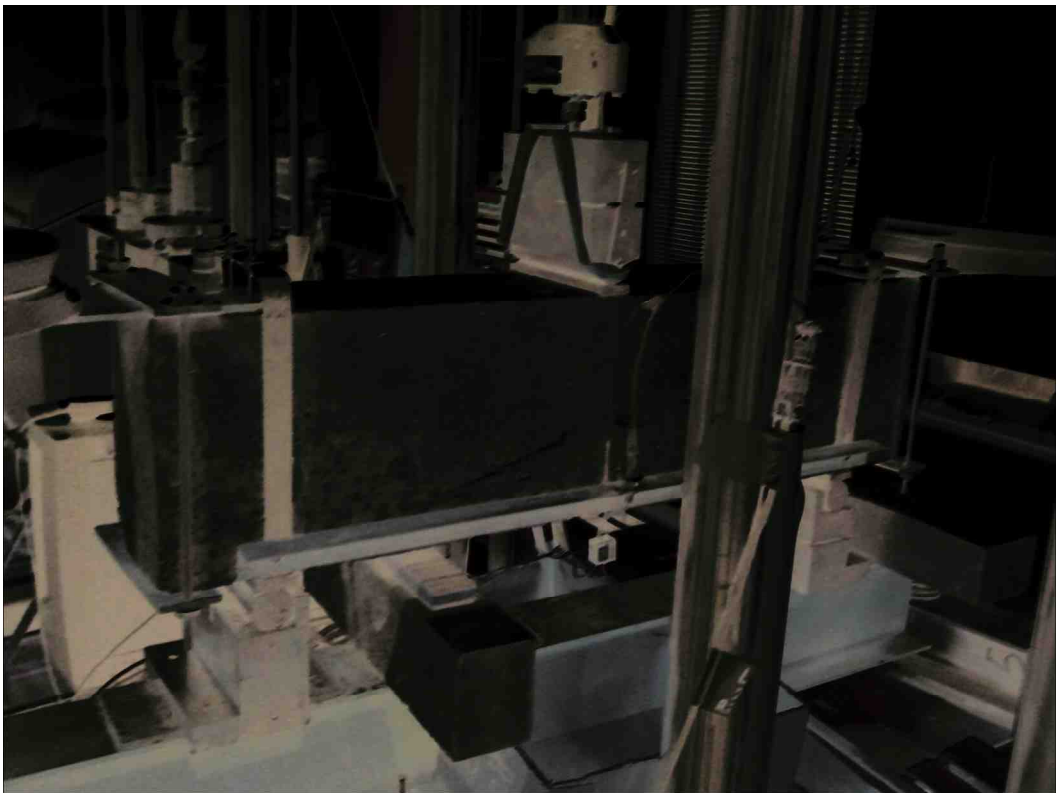

Figure 29: Setup for 229 mm (9 in) deep beam

As shown in Figure 26, the W6X16 beam was not wide enough to use the bolt holes to secure the support blocks, so the supports were instead glued into place using cyanoacrylate-based glue.

3.2.2 Counterweight System

As discussed in Chapter 2, it is desirable to provide a slight over-compensation for self-weight for stability purposes, creating a small negative moment at mid-span. To assure a negative moment at center span of the concrete beams, a counterweight system was developed. As discussed in Section 3.1.2, the procedures for the NBLII tests outlined in ACI 446-5 contained an error regarding the specimen length. This led to previous NBLII tests achieving zero moment in the middle as opposed to the required negative moment. Preliminary testing using dummy specimens 152 mm deep had weights stacked perilously upon the overhangs, as shown in Figure 30.

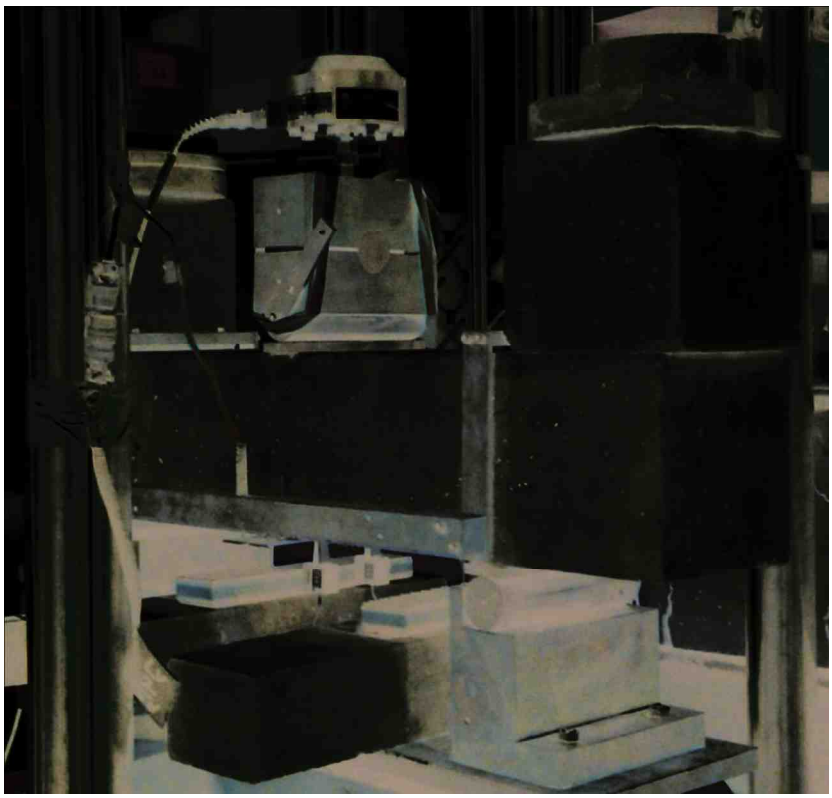

Figure 30: Dummy specimen with stacked counterweights on overhangs

The above setup is not sufficient for safety reasons. At the end of the test, the specimen experienced dynamic unstable fracture, which caused the loose weights to dangerously fall to the floor. Combined with safety concerns was the discovery of the need for negative moment at the center of the beam, requiring much more weight to be stacked. Thus, the stacking of weights upon the overhangs was no longer acceptable for the experiment, and a new counterweight system was constructed.

With safety concerns at the forefront of the counterweight system development, the weights needed to be clamped to the beam without interfering with the test, and the moment arm had to be increased significantly to reduce the amount of weight needed to create the required negative moment. Figure 31 and Figure 32 show the new counterweight system. A ¼" thick, 4" wide and 12" long steel plate was used to hold the counterweights, while smaller steel plates with machined holes were bolted to threaded rods that clamped to the top and bottom of the beam.

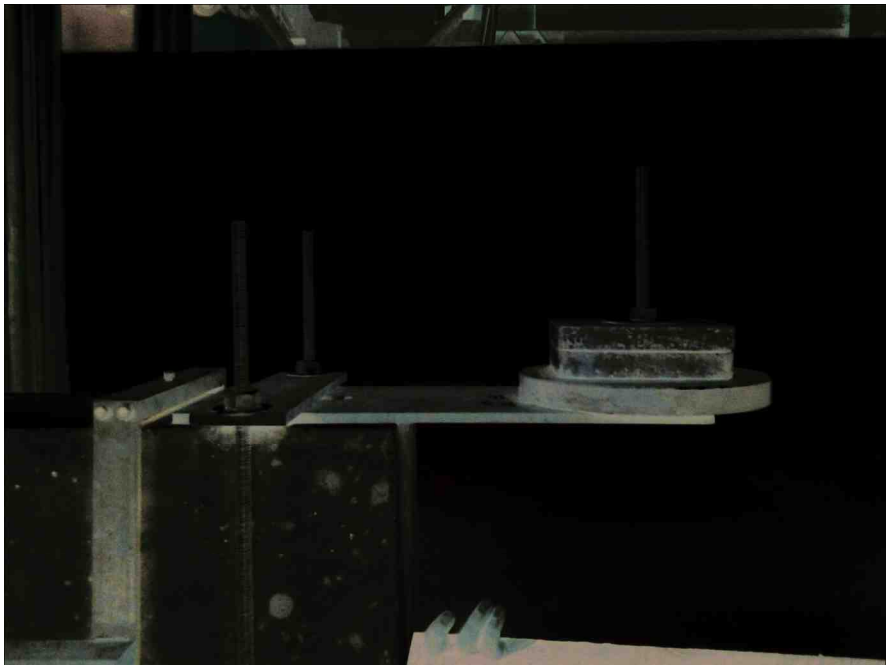

Figure 31: New counterweight system clamped to beam

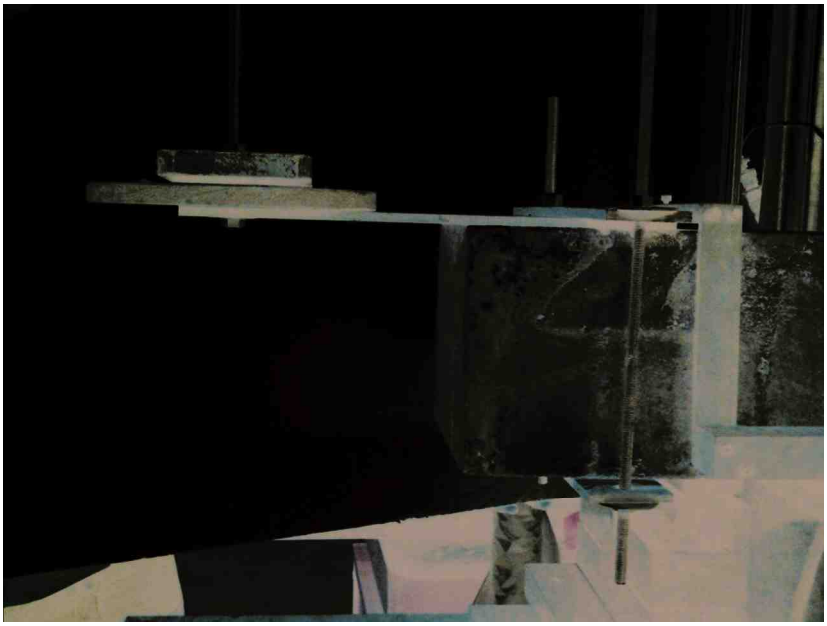

Figure 32: View of counterweights and clamping by threaded rods bolted to steel plates

Figure 33: Detail showing counterweight holding plate does not interfere with LVDT reference frame

To assure the safest configuration, the counterweight holding-plate was placed as close as possible to the LVDT reference frame without interfering with it. Figure 33 shows the plate positioned roughly ¼" clear of the edge of the LVDT reference frame.

Several dummy tests of 152mm (6") deep specimens showed the new counterweight system provided a much safer alternative to stacking the weights on the overhangs. However, dynamic instability still caused the weights to fall perilously to the floor. Concrete blocks were placed on the end of the support beam to "catch" the specimens in the event of dynamic instability, but these efforts proved inadequate in most cases. For safety, a method to catch the broken halves of the specimen is still needed.

To determine the needed amount of counterweight, a simple closed-form equation was developed, using statics analysis, given the weight of the counterweight system, the weight of the beam, and the placement of the counterweights. Figure 34 depicts a free-body diagram of the half-beam with the following definitions: M is the negative internal moment at the center of the beam, C is the added counterweight, W_1 is the weight of the plates holding the counterweight, Z_1 is the distance from the support to the center of gravity of C, Z_2 is the distance of the center of the support to the center of gravity of W_1, S is the span length, W_B is the weight of the half-beam, and Q is the length of the overhang from the end of the beam to the support.

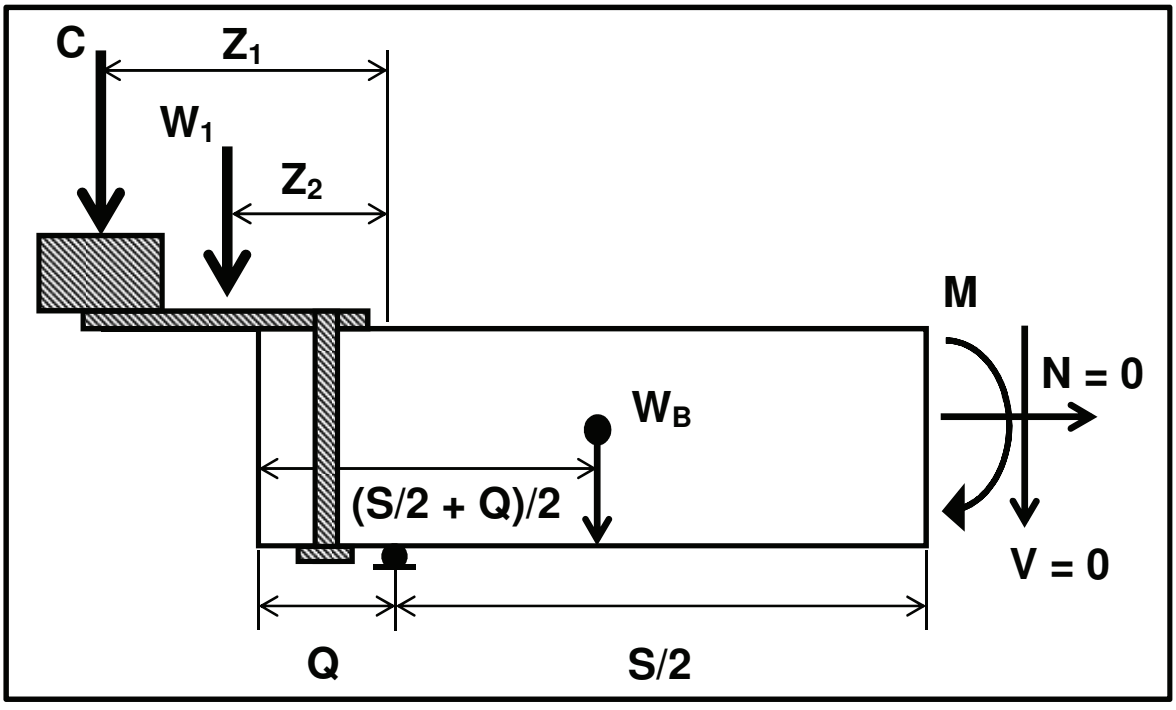

Figure 34: Half-beam dimensions used to calculate counterweight values

Assuming static equilibrium and by summing moments about the support, the following equations determine the range of counterweight needed, as well as the internal negative moment developed at the center of the beam once the counterweights are attached:

$$C = \left[M - W_1 Z_2 + \frac{mg}{2L}\left(\frac{S^2}{4} - Q^2\right)\right] / Z_1 \ , \tag{74}$$

and

$$M = W_1 Z_2 + C Z_1 + \frac{mg}{2L}\left[Q^2 - \frac{S^2}{4}\right] \ , \tag{75}$$

where m is the mass of the beam, g is the acceleration due to gravity, and L is the total length of the beam. After determining the range of the center-span negative moment required for the beam, as discussed in Section 3.1.2, the first equation is then used to determine the range of the required counterweight. Once an appropriate counterweight is chosen, the second equation is then used as a check to assure the internal moment at midspan is within the required range.

Table 6 shows the calculated values for internal center-span moment of each beam group and the counterweight masses used. Note that for the calculations of internal center-span moment, the counterweight masses were converted into Newtons.

Table 6: Counterweights and internal moment ranges

Beam Group D3

Specimen	Mass (kg)	Counterweight Mass (kg)	Allowable Internal Moment Range (N-mm)	Center-Span Moment (N-mm)
B1S1	14.8	0	1,040 < M < 2,070	1,840
B1S2	14.8	0	1,040 < M < 2,070	1,840
B1S3	14.8	0	1,040 < M < 2,070	1,840
B1S4	14.8	0	1,040 < M < 2,070	1,840

Table 6 (cont.)

Beam Group D6

Specimen	Mass (kg)	Counterweight Mass (kg)	Allowable Internal Moment Range (N-mm)	Center-Span Moment (N-mm)
B1S1	40.4	4.53	5,660 < M < 11,300	9,120
B1S2	40.4	4.53	5,660 < M < 11,300	9,120
B2S1	40.4	4.53	5,660 < M < 11,300	9,120
B2S2	40.1	4.53	5,630 < M < 11,300	9,220

Beam Group D9

Specimen	Mass (kg)	Counterweight Mass (kg)	Allowable Internal Moment Range (N-mm)	Center-Span Moment (N-mm)
B1S1	70.8	20.40	14,890 < M < 29,800	22,300
B1S2	68.9	20.40	14,490 < M < 29,000	23,400
B1S3	68.9	20.40	14,490 < M < 29,000	23,400
B2S1	70.7	20.40	14,860 < M < 29,700	22,300

3.2.3 LVDT Reference Frame

As discussed in Chapter 2, the load vs. load point displacement curve is needed to determine the work of fracture of the beam. This is achieved by rigidly fastening LVDT's to a reference frame placed upon the beam, with the moving LVDT rods resting upon steel plates (knife edges) as shown in Figure 35. The LVDT measurements of load point displacement were taken from opposite sides of the notch on either side of the beam, which were averaged. Figure 35 also shows both knife edges, where the second LVDT (not in view) would be resting upon the opposite knife edge on the opposite side of the beam.

Figure 35: Photograph of LVDT attached to reference frame, resting upon knife edge

To obtain an accurate load point displacement, measurements need to be taken so that no local deformations or settlements of the testing equipment interfere with the readings. The energy dissipated by local deformations and settlements can be a significant percentage of G_F and is not of interest, so care was taken to assure that the reference frame rests directly above the center of the supports. Sections 7.5.1 and 7.5.3 of Chapter 2 of ACI 446-5 also require that a sufficiently stiff LVDT reference frame be placed upon the top of the beam so that it rests directly above the supports on conical screws (two over one support, one over the other.) Section 7.5.2 requires that the reference frame must also be adequately stiff so that it does not deflect under self-weight more than 0.002 mm (8×10^{-5} in.) A frame had been previously manufactured for 152 mm (6 in) deep specimens for notched beam testing conforming to these requirements, and was used again in this experimental program.

Unfortunately the frame was not useable for the span lengths for the other sizes of specimens, so new reference frames had to be constructed. Due to cost concerns, a similar machined reference frame for the other sizes was not possible, and a more economical solution was needed.

For the 76 mm (3") deep specimens, a reference frame was constructed using perforated steel angle, cut and bent so that the two ends could be connected into the proper shape for a reference frame. These parts were then

connected by gluing them together with pieces of aluminum angle with holes drilled to accommodate the LVDTs. Figure 36 shows a photo of the completed frame.

To mount the LVDTs, metal collars with set screws were glued to the tops of the aluminum angles. The set screws proved adequate to assure the LVDTs were fixed properly to the frame. Lastly, the conical screws used to rest upon the beam were bolted to the frame through the perforated holes in the steel angle with washers and nuts.

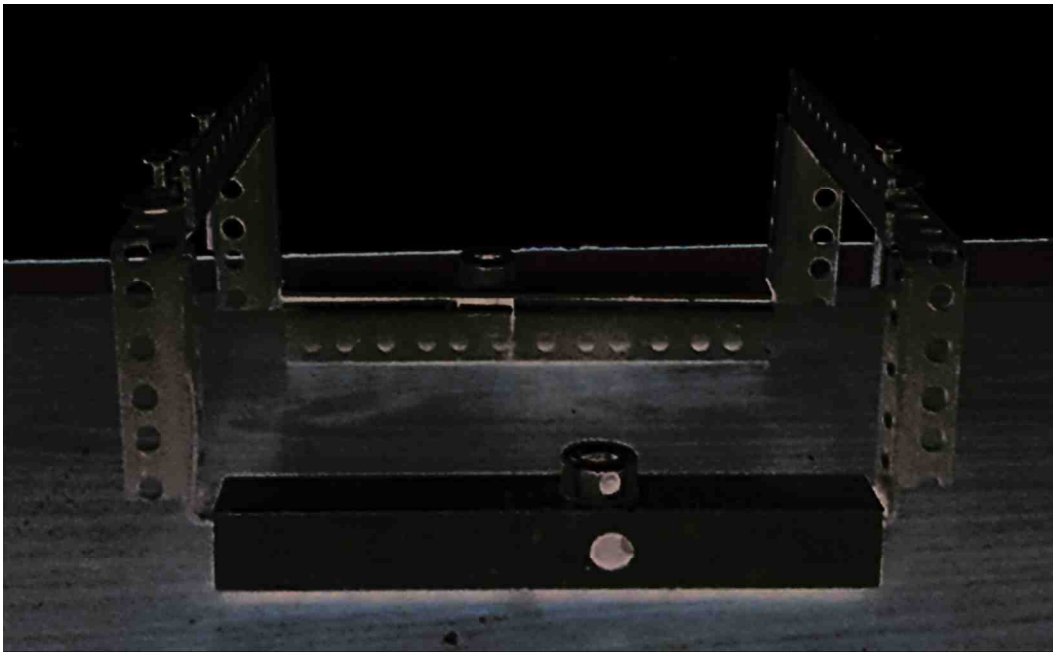

Figure 36: LVDT reference frame for 76 mm (3 in) deep specimens

The LVDT reference frame for the 229 mm-deep (9") specimens was crafted using pieces of steel angle bolted to bent pieces of steel plate. Holes were drilled in the steel angle to accommodate the LVDTs, as well as in the steel plate to accommodate the conical screws. Once again, metal collars with set screws were glued to the tops of the steel angles to provide for fixing the LVDTs to the frame, and the conical screws were attached to the steel plates by washers and nuts. Figure 37 shows a picture of the LVDT reference frame used for the 229 mm (9 in) deep specimens. It should be noted that the frame in Figure 37 was damaged after the last test of the experimental program, and thus is misaligned in the photograph.

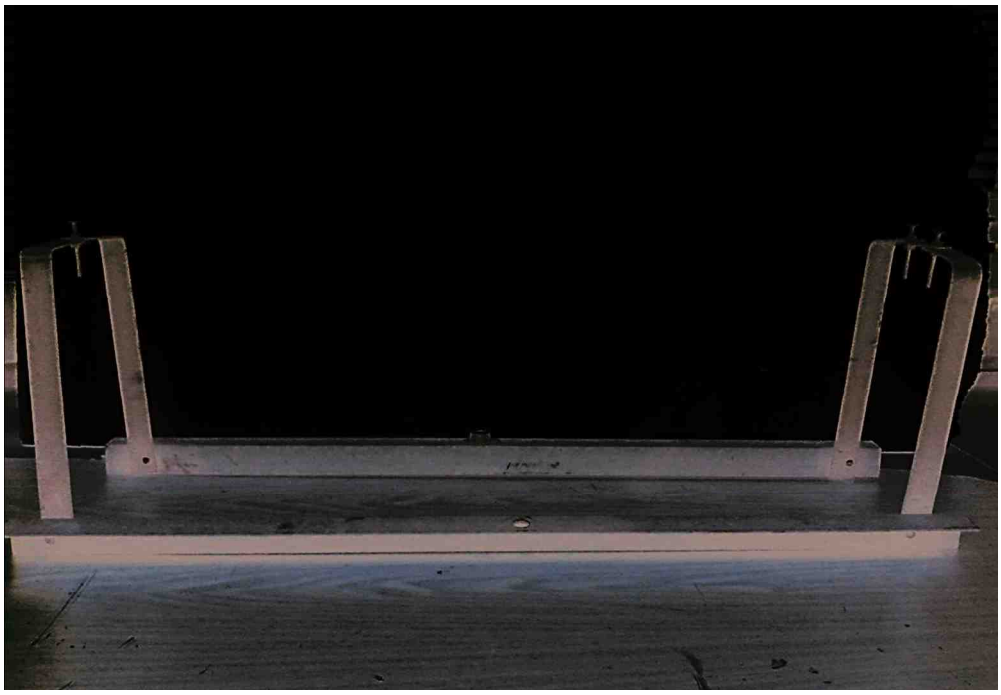

Figure 37: LVDT reference frame for 229 mm (9 in) deep specimens

3.2.4 Specimen Preparation

On the day of testing, several preparations were made before testing could begin. According to Section 6.4.2 of Chapter 2 of ACI 446-5, the specimens are to be kept wet during pre-test preparation through the use of spray bottles and wet towels to assure the concrete remains moist. Due to the potential of electrical interference, the specimens were not kept wet once the clip gauges and LVDTs were attached. In the author's opinion, keeping the beams moist throughout the test is rather impractical, and suggestions are made to change this requirement in ACI 446-5.

The rest of this section discusses the process of beam preparation in full. Section 3.2.4.1 discusses the beam notching, Section 3.2.4.2 discusses the attachment of the knife edges, and Section 3.2.4.3 discusses the clip gauge and LVDT attachment and preparation.

3.2.4.1 Beam Notching

Notching was performed several days before testing. Beams were taken from the curing tank and kept moist during the entire notching procedure before

being placed back into the curing tank. Each specimen was notched with a saw blade with nominal thickness of 2.54 mm (0.1 in) to the nominal depths specified in Table 4.

To obtain an even notch depth, the saw blade was set in a fixed position, and the beam, resting on a traveling table, was slowly pushed into the blade, cutting away material until the notch depth was even across the specimen. After the first pass through, the depth of the notch was checked using a digital caliper, and adjustments were made to the saw blade height if the notch depth was too shallow. Special care was taken to avoid creating a notch that was too deep to begin with, and often multiple passes were needed to obtain the correct notch depth for each specimen.

3.2.4.2 Knife Edges

On the day of testing, specimens were taken from the curing tank so that the knife edges could be attached using a cyanoacrylate-based glue. The knife edges were placed on both sides of the notch so that clip gauges could be attached to measure the crack mouth opening displacement. Figure 38 shows a conceptual detail of the clip gauge and knife edges attached to both sides of the notch.

The beam was then placed on a platform, and the area near the notch was dried with towels to clear all standing water so the glue could set. Although the concrete around the notch was still somewhat moist, there were no problems with the glue setting so long as no standing water was visible in the area to be glued. Figure 39 shows a picture of the beam on the platform before the knife edges were glued to the surface. A liberal layer of glue was then applied to one knife edge, and placed on one side of the notch, with care taken to assure it was parallel to the notch.

Once the glue had cured on one side, glue was applied to the other knife edge. The second knife edge was then placed, using spacers 2.54 mm (0.1 in) thick to assure even spacing between the knife edges along the notch. Figure 40 shows the knife edges after they had been glued into place.

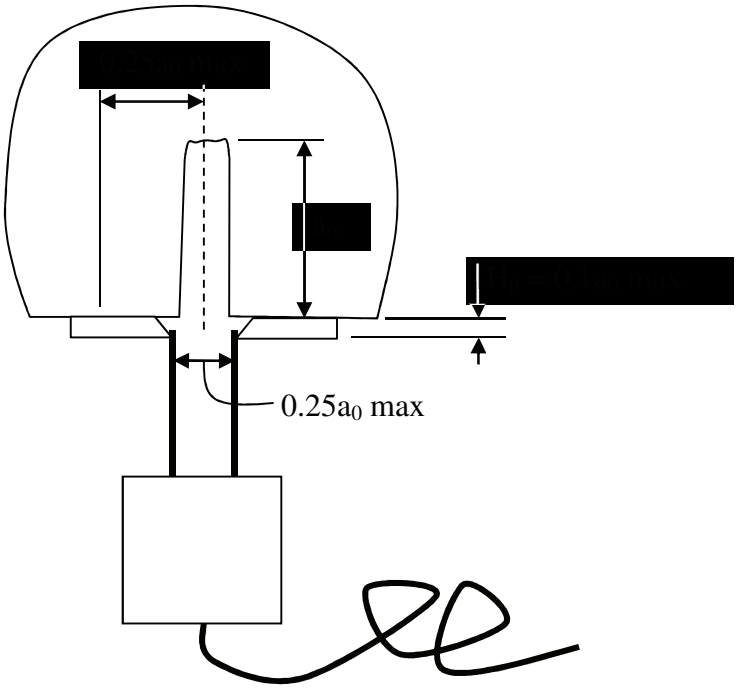

Figure 38: Detail of clip gauge and knife edges [ACI, 2010]

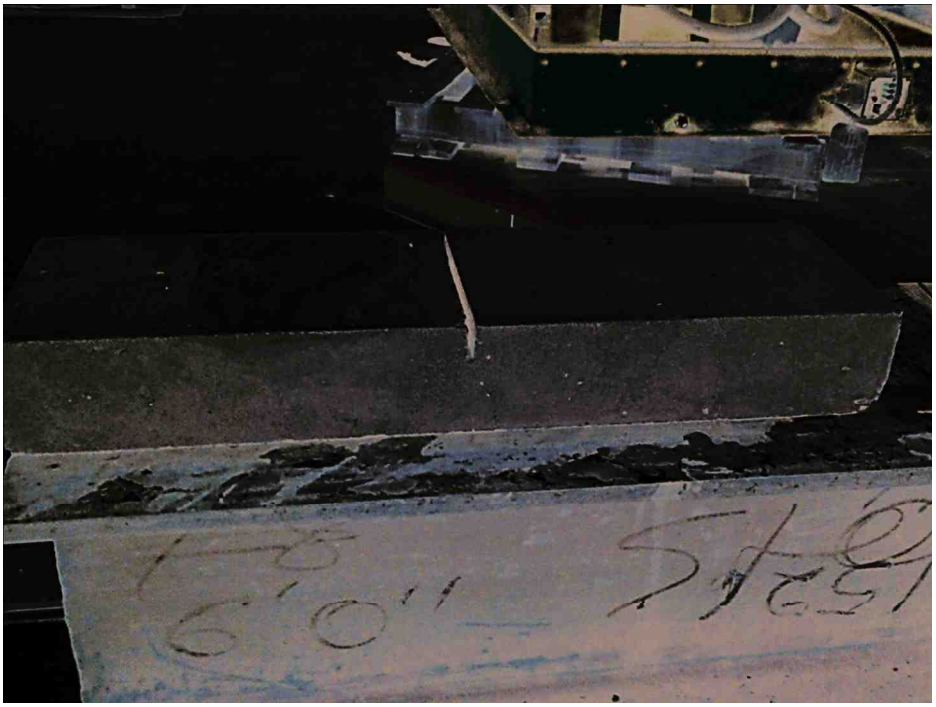

Figure 39: Picture of beam before attaching knife edges

Figure 40: Photograph of beam after gluing knife edges

Lastly, a clip gauge was placed at several points along the notch with readings taken to assure that the spacing was even and that the knife edges would not pop loose from the force exerted by the clip gauge. It should be noted that it was impractical to keep this area of concrete moist until after the glue had cured. However, whenever possible the concrete was sprayed with water or had wet towels draped over it to hold in as much moisture as possible until testing.

3.2.4.3 Clip Gauge and LVDT Attachment

Before attachment of the knife edges, two MTS Model 632.02 clip gauges and two LVDTs were calibrated using readings from the testing machine software and a conventional micrometer as a reference. The clip gauges were calibrated to operate between -0.5 to 2 mm, while the LVDTs were calibrated to operate between -10 to 10 mm.

After attaching the knife edges, the beam was immediately placed upon the steel bearing plates on the supports in the testing apparatus. The beam was

then centered on the supports, and the placement measured and adjusted if needed to assure the proper overhang. Figure 41 shows a photograph of the specimen in the testing apparatus.

Figure 41: Picture of specimen after being placed upon the supports

At this point, if necessary, the counterweights were attached as discussed in Section 3.2.4.1. The LVDT reference frame was then placed so that the conical screws rested directly above the supports. From here, the LVDTs were attached and adjusted in the steel collars with set screws so that they produced close to zero-voltage through the machine readings. The clip gauges were then inserted between the knife edges on opposite sides of the notch. Figure 42 shows a photograph of the LVDT reference frame with the attached LVDTs, and Figure 43 shows the attached clip gauges.

Figure 42: Photograph of LVDT reference frame attached to beam

Figure 43: Photograph of clip gauges attached to knife edges on underside of beam

Once the instrumentation had been attached, the specimen was ready for testing. At this point, it was no longer practical to keep the concrete moist, as the spray bottles could cause electrical interference with the clip gauges or LVDTs.

3.3 Loading Procedure

In order to calculate key fracture parameters of the concrete, ACI 446-5 requires that specimens be placed under closed-loop CMOD control for the duration of the test. Theoretically, this should allow for the specimen to achieve a well-developed softening curve as the machine adjusts the stroke of the loading apparatus to achieve specific a CMOD at a specific time.

First, to minimize any seating non-linearity, each specimen was placed under an initial pre-load. Section 8.2.3 of Chapter 2 of ACI 446-5 requires that the pre-load be between 5-10% of the estimated peak load, not to exceed 15% of the peak load. Table 7 shows the pre-load used for each specimen.

Table 7: Pre-load for each specimen

Beam Group D3

Specimen	Pre-Load (N)
B1S1	392
B1S2	230
B1S3	257
B1S4	287

Beam Group D6

Specimen	Pre-Load (N)
B1S1	48
B1S2	10
B2S1	37
B2S3	146

Beam Group D9

Specimen	Pre-Load (N)
B1S1	678
B1S2	730
B1S3	698
B1S4	932

It should be noted that the specimens in Beam Group D6 do not conform to the specifications because the pre-load is too small. The specimens in Beam Group D6 were the first specimens tested, and due to a misunderstanding of the specifications an inadequate pre-load was applied, which should have been in the range of 600 to 1,200 N. However, as will be discussed in Chapter 4, this did not severely affect the outcome of the experiments. Thus, it may be practical to remove the pre-loading requirement in ACI 446-5.

Once the pre-load had been applied and recorded, all the measurement instrumentation was zeroed, and testing could begin, which was typically around 30-40 minutes after the specimen had been removed from the curing room. However, during preliminary testing, it was discovered that using CMOD control was not an optimal solution for achieving the full softening curve. In order to overcome this problem, a different testing technique was developed. Section 3.3.1 discusses the difficulties in achieving the full softening curve, Section 3.3.2 discusses the use of CMOD control, and Section 3.3.3 discusses the use of machine stroke control

3.3.1 Achieving the Full Softening Curve

During preliminary testing, it was discovered that the specimen experienced dynamic instability rapidly leading to failure of the test setup before a complete softening curve could be developed. Section 7.6.3 of Chapter 2 of ACI 446-5 declares that testing may be terminated when the CMOD reaches a value of 4D/300, where D is the depth of the specimen. For the 152 mm (6") deep specimens, this translates to a CMOD ≈ 2.0 mm.

However, the preliminary tests revealed that using CMOD control would achieve a final CMOD as low as 0.3 mm at the point when dynamic instability took place. This phenomenon is illustrated in Figure 44, which shows a typical load-CMOD curve for a 152 mm (6") specimen, where the test ends prematurely around 0.3 mm, with the dotted line representing what the curve should look like if a full softening curve were achieved.

It appears that this problem is not isolated to the testing done in this experimental program, as ACI 446-5 contains a figure that shows similar behavior. Figure 45 shows the typical response curve of load vs. CMOD as seen in Section 8.3.2 of Chapter 2 of ACI 446-5. As one can see, the CMOD only reaches 0.4 mm, and does not appreciably approach being asymptotic before the test has ended.

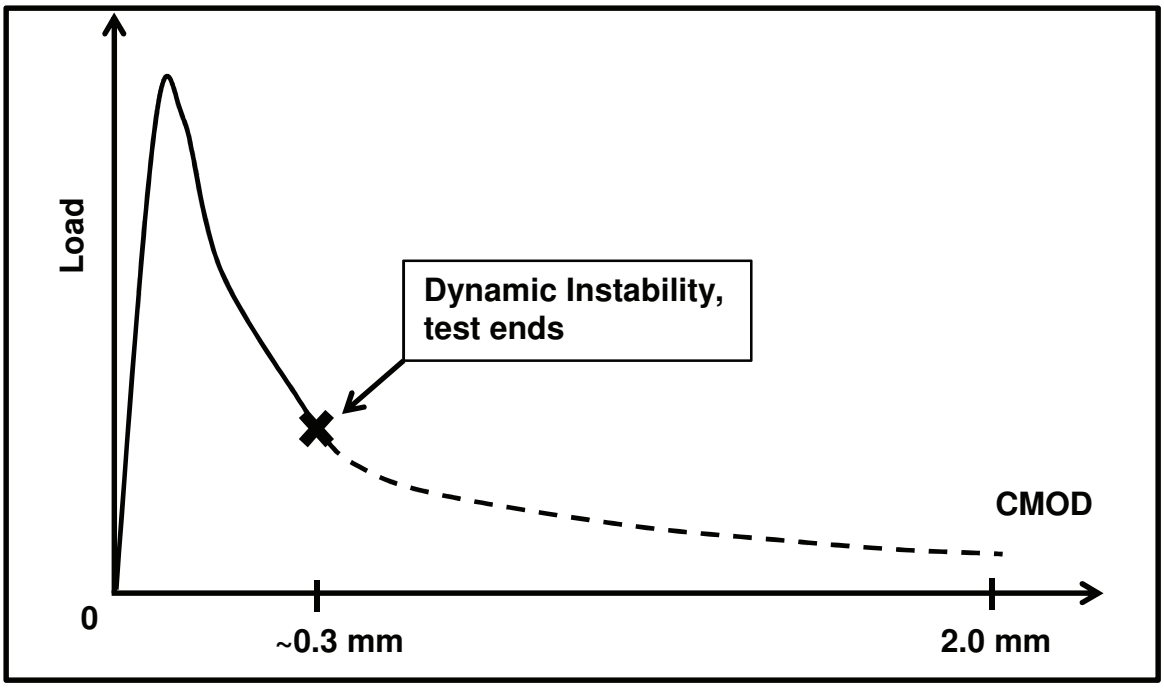

Figure 44: Typical load-CMOD curve of 152 mm (6") specimens for CMOD controlled test

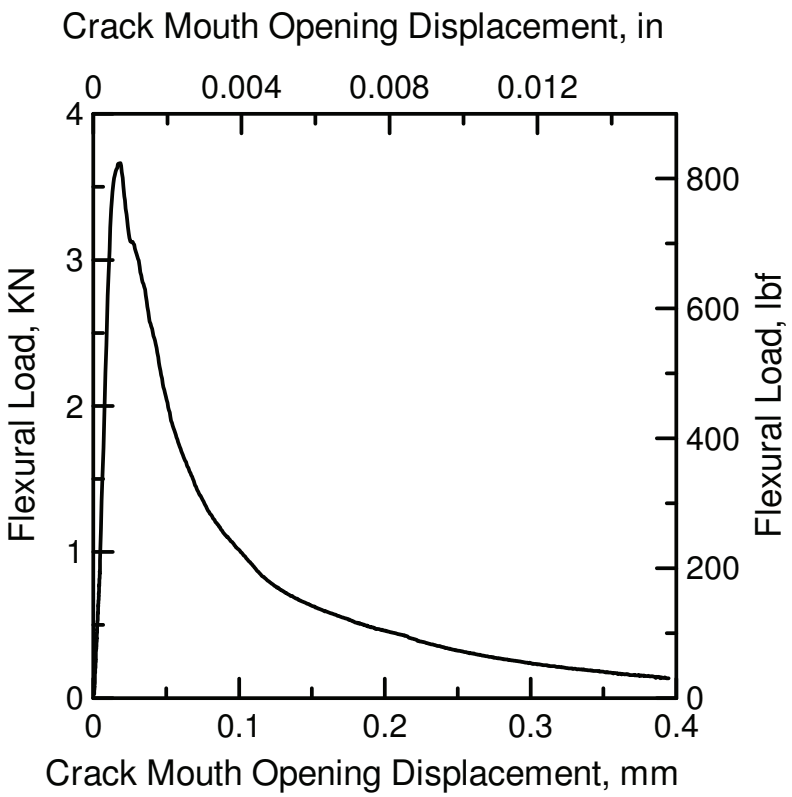

Figure 45: Load vs. CMOD response, Figure 2.9 in ACI 446-5 [ACI, 2010]

Investigation into this phenomenon revealed that the machine would over-compensate for unpredictable jumps in CMOD, which would lead to dynamic

instability, thus ending the test. Video of this phenomenon was taken, showing that the specimen would suddenly fracture, causing the clip gauges to fall from the knife edges, and the machine would turn off due to tripping pre-defined safety measures set up to prevent the machine from displacing beyond the boundaries of the experiment. Several methods were attempted to correct this dynamic instability, described next.

3.3.2 CMOD Control

The loading procedure from the testing machine's software followed a simple algorithm for CMOD control. Section 8.2.5 of Chapter 2 of ACI 446-5 suggests the following piecewise functions for the closed-loop servo-hydraulic machine to achieve a specific CMOD at a specific time:

$$CMOD = w_0 \, t/t_0 \quad \text{for } \mathrm{t} < \mathrm{t}_0 \,, \tag{76}$$

and

$$CMOD = \, w_0 \, e^{\frac{t-t_0}{t_0}} \quad \text{for } \mathrm{t} > \mathrm{t}_0 \,, \tag{77}$$

where

w_0 = nominal CMOD at the peak load

t = time

t_0 = nominal time to peak load (3 to 5 minutes.)

Given these functions, the expected time to completion, according to Section 8.2.5 of Chapter 2 of ACI 446-5, should be between 15 and 25 minutes.

It should be noted that the software used in this experimental program did not average the readings from the clip gauges during testing, so only one of the clip gauges was used to measure the CMOD.

During the test, the machine software recorded data points for load, CMOD, LPD, machine stroke, and time every 0.1 seconds for each specimen until the test completed. Data points were taken from the CMOD and LPD using two clip gauges and two LVDT's respectively, which were later averaged during data analysis. In general, the first specimen of the series was used to determine and adjust the expected nominal CMOD at the peak load, w_0, if the peak load was not achieved within the specified time of 3 to 5 minutes.

The loading procedure was split up into 3 to 4 minute time frames, where the machine would try to achieve a specific CMOD by the end of a time period. As an example, Table 8 shows the loading procedure used for specimen B1S2 from Beam Group D6.

Table 8: Example of testing machine CMOD control procedure for specimen B1S2 from Beam Group D6

Time range (minutes)	Target CMOD (mm)
0 < t < 5	0.0350
5 < t < 9	0.0750
9 < t < 12	0.140
12 < t < 16	0.220
16 < t < 20	0.460
20 < t < 25	1.000
25 < t < 30	2.000

As discussed above, it was observed that this method pre-maturely ends the test through dynamic full fracture well before a full softening curve can be developed. In the case of specimen B1S2 from Beam Group D6, the test ended when the CMOD reached a value of 0.45 mm, occurring 19 minutes and 40 seconds into the test. An alternative loading procedure was therefore developed, as discussed further in Section 3.3.3.

The testing procedure above also does not closely follow the equations outlined in Section 8.2.5 of Chapter 2 of ACI 446-5 for CMOD control. In an attempt to prevent dynamic instability, the rate of CMOD growth was significantly slowed down, although to little effect. In the first run of experiments, all the specimens in Beam Group D6 relied solely on CMOD control before an alternative method was developed, described next.

3.3.3 Stroke Control

After testing of Beam Group D6 was completed, several more dummy tests were performed in an attempt to discover a way of achieving stable

behavior up to the maximum allowed final CMOD. Slowing down the rate of CMOD growth had little effect, so another approach was developed. While Section 8.2.5 of Chapter 2 of ACI 446-5 suggests that CMOD control be used throughout the experiment, the only requirement is to keep the CMOD growth rate at a value between 0.001 and 0.01 mm/s, stated in Section 7.6.1. This rate can theoretically be achieved through other means, such as LPD control or machine stroke control. The latter proved the most useful, since all machine procedures at their base software functions rely on the machine stroke (i.e. to increase force, the machine stroke displaces a certain amount until the force is achieved.) Applying this logic, a new loading procedure was created to use a hybrid of CMOD control to start the experiment, and switching to machine stroke control before the specimen entered dynamic instability. Table 9 shows the loading procedure for specimen B1S4 from Beam Group D3.

Table 9: Example of testing machine hybrid control procedure for specimen B1S4 from Beam Group D3

Time range (minutes)	CMOD (mm)
$0 < t < 5$	0.025
$5 < t < 9$	0.055
$9 < t < 12$	0.100
$12 < t < 16$	0.200
$t > 16$	Stroke Downward, 0.01 mm/min

Once the machine entered stroke control, the machine stroke was set to displace vertically downward at a rate of 0.01 mm/min. This rate kept the CMOD growth rate within the bounds specified above, while also preventing any dynamic instability from occurring. Figure 46 shows the load vs. CMOD curve from specimen B1S4 from Beam Group D3. As one can see, the softening curve is well developed, and becomes appropriately asymptotic out to 4D/300 = 1 mm of CMOD.

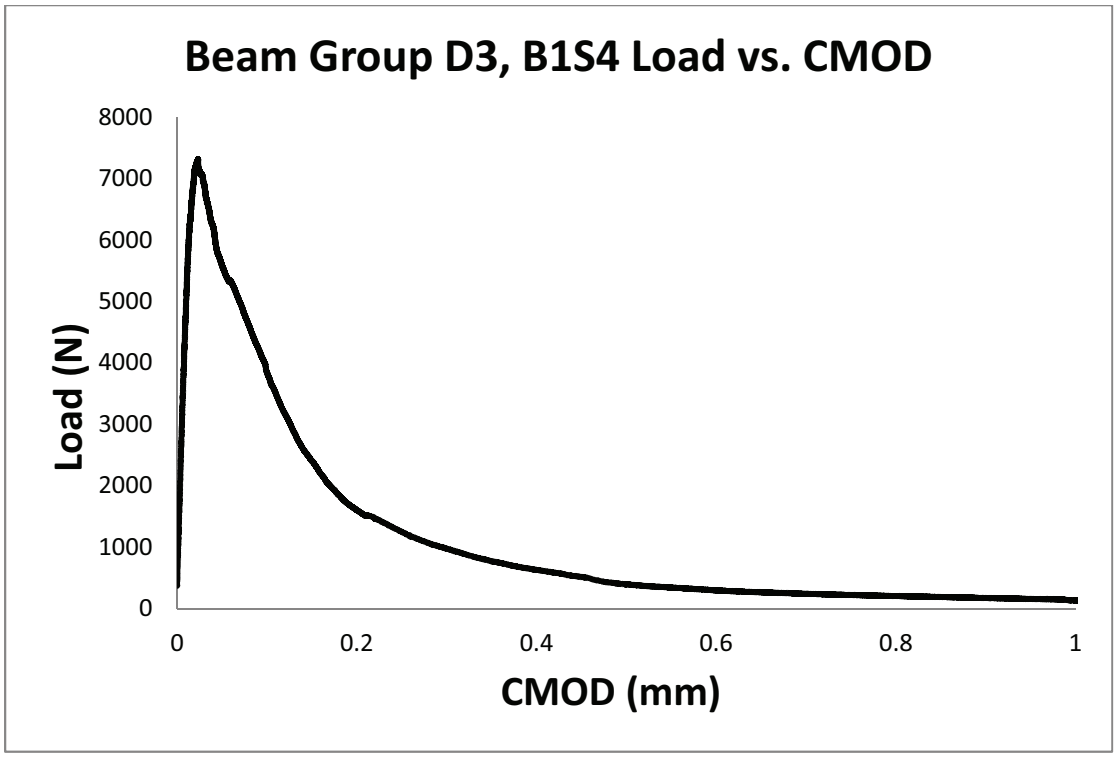

Figure 46: Load vs. CMOD curve for specimen B1S4 from Beam Group D3

This method was considered successful and was used for the remaining specimens in the experiment. However, no strict formula to determine when to engage stroke control has been developed yet. The process of determining when to enter stroke control and what rate of stroke control to use was determined largely by trial and error. Generally, the first specimen of the series was used to determine when stroke control was appropriate, along with adjusting the CMOD values for attaining the peak load within the 3 to 5 minute time frame.

Also, more recent NBLII experiments for high-strength concrete, performed by Ebadollah Honarvar Gheitenbaf of the University of New Mexico, that have attempted to use the stroke control method for high strength concretes have not been successful. Preliminary observations show that the CMOD opens rapidly at the start of stroke control, violating the provisions of Section 7.6.1 of Chapter 2 of ACI 446-5. This could be due to a number of phenomena, the most obvious being machine snap-back. Since the stiffness of high strength concrete is much higher than normal strength concrete, the ratio of stiffness between the machine and the specimen is much lower, and could cause a snap-back

phenomenon. It is possible that with higher machine stiffness stroke control could be useful for high strength concretes, but more research in this area is needed.

3.4 Experimental Results

In accordance with Section 7.6.2 of Chapter 2 of ACI 446-5, data was recorded during testing every 0.1 s for the LVDTs, clip gauges, force, and machine stroke. Immediately after testing, the completely fractured specimens were weighed and pertinent dimensions measured according to the procedure outlined in Section 3.1.2. Any anomalies during testing were also recorded in accordance with Section 9.1.6 of Chapter 2 of ACI 446-5.

Data was recorded for load, CMOD and LPD, where load was measured by a load cell, CMOD was measured using the clip gauges, and LPD was measured using LVDTs. This section primarily focuses on what is considered raw data of the loads and readings of the clip gauges and LVDTs.
At no point in Chapter 2 of ACI 446-5 is it specified that pre-loading data must be recorded, and thus for this experimental program, pre-loading data was not recorded. After pre-loading, the instrumentation was zeroed, and thus the recorded load data were adjusted by adding the zeroed-out pre-load back into each data point. Curves were then created of load vs. CMOD and load vs. LPD based upon the measurements from the instrumentation. The analysis and manipulation of these curves to obtain the key fracture parameters of the bilinear cohesive crack model are discussed further in Chapter 4.

For several specimens, pictures and video were taken during the final minutes of the test to record any machine instability as well as to observe whether the beam-halves lifted up at the center after complete fracture, proving that internal negative moment at center span was indeed available. In every case, video showed that negative moment was available at the center of the beam.

Table 10 reports the dates of each test, the recorded peak loads, and any anomalies observed on the day of testing. Figures 46 through 49 show the load

vs. CMOD curves for each specimen, while Figures 50 through 52 show the load vs. LPD curves for each specimen.

Lastly, Figure 53 and Figure 54 show the load vs. CMOD and load vs. LPD curves for each beam group, respectively.

Table 10: Dates of tests and record of anomalies

Beam Group D3

Specimen	Date of Test	Anomalies
B1S1	8/4/2010	None observed
B1S2	8/3/2010	-CMOD growth rate > 0.01 during stroke control -Data anomaly at 16 minutes and 40 seconds
B1S3	8/3/2010	None observed
B1S4	8/4/2010	None observed

Beam Group D6

Specimen	Date of Test	Anomalies
B1S1	6/25/2010	Dynamic unstable failure at CMOD = 0.45 mm
B1S2	7/8/2010	Dynamic unstable failure at CMOD = 0.46 mm
B2S1	7/9/2010	Dynamic unstable failure at CMOD = 0.53 mm
B2S2	7/9/2010	Hump in data at peak load Dynamic unstable failure at CMOD = 0.61 mm

Beam Group D9

Specimen	Date of Test	Anomalies
B1S1	8/4/2010	None observed
B1S2	8/3/2010	None observed
B1S3	8/3/2010	None observed
B2S1	8/4/2010	Dynamic unstable failure at CMOD = 0.47 mm

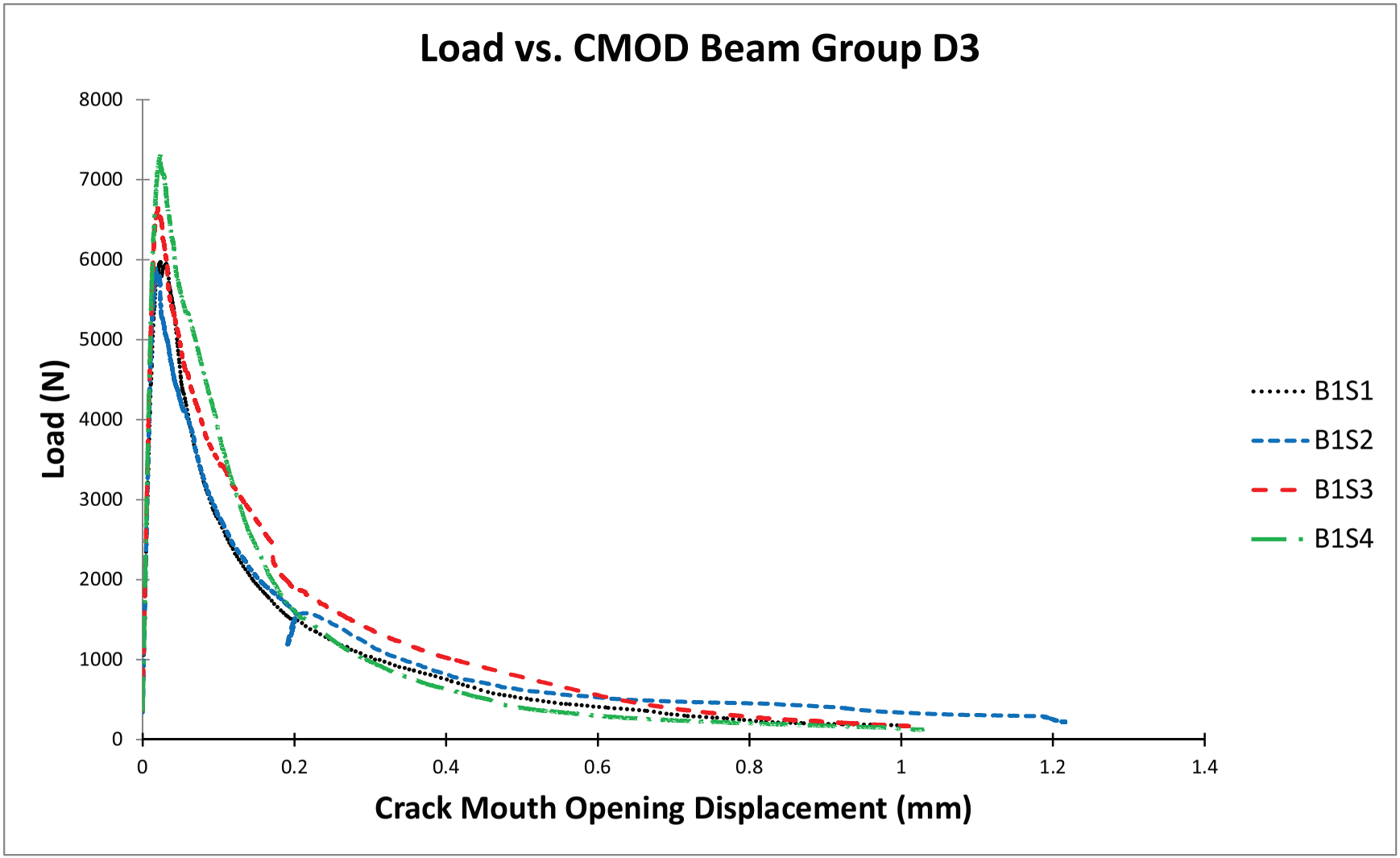

Figure 47: Load vs. CMOD curves, Beam Group D3

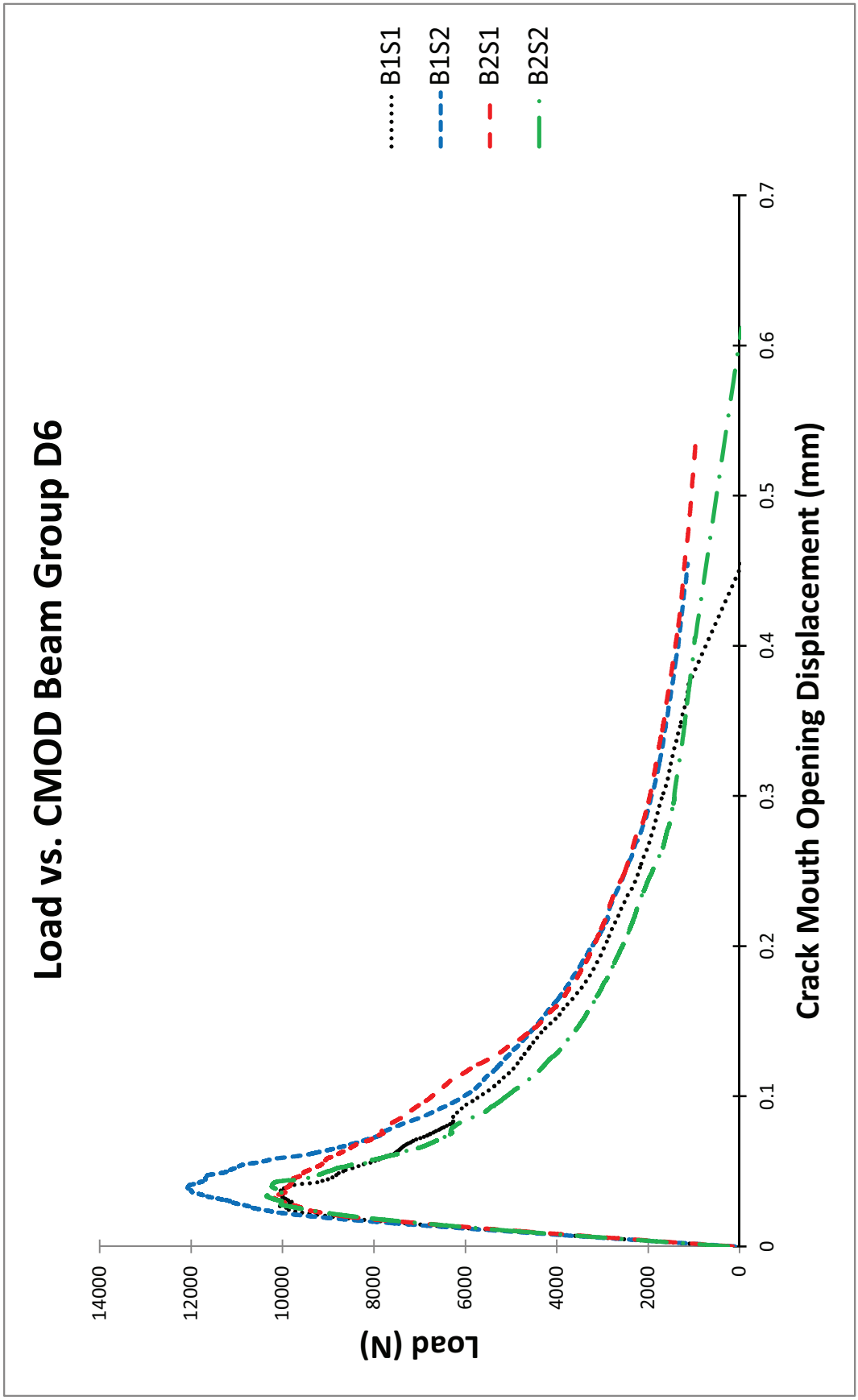

Figure 48: Load vs. CMOD curves, Beam Group D6

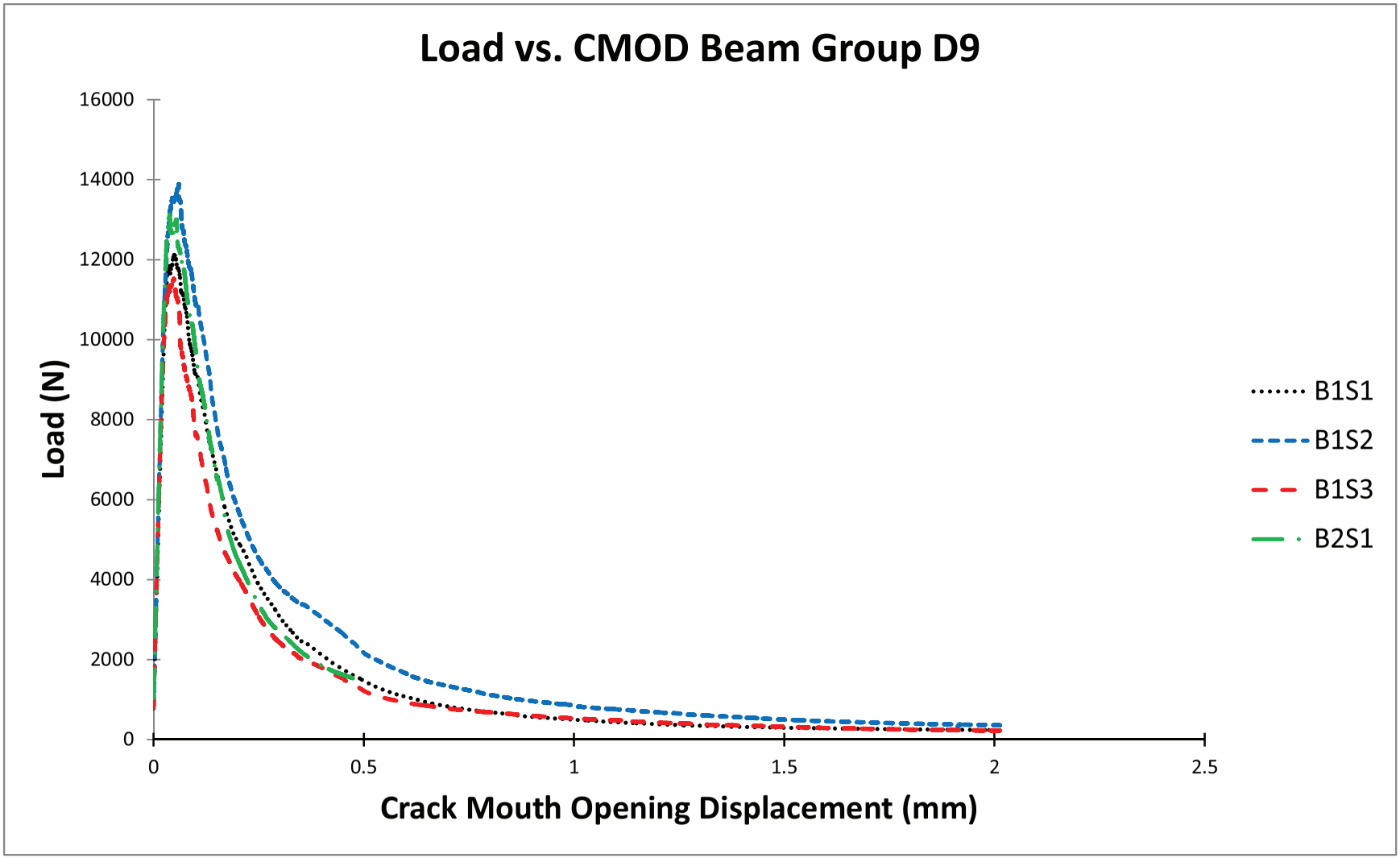

Figure 49: Load vs. CMOD curves, Beam Group D9

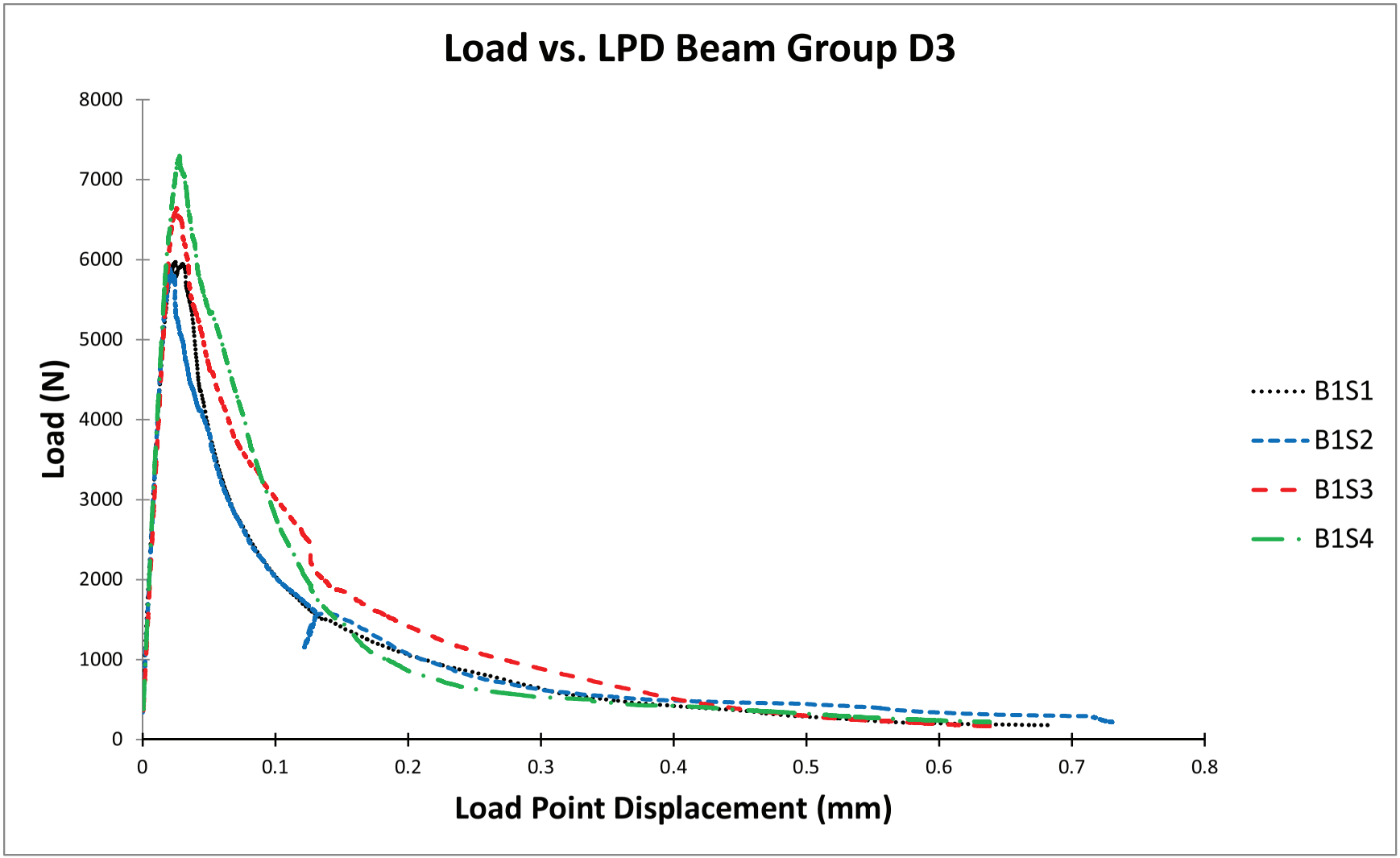

Figure 50: Load vs. LPD curves, Beam Group D3

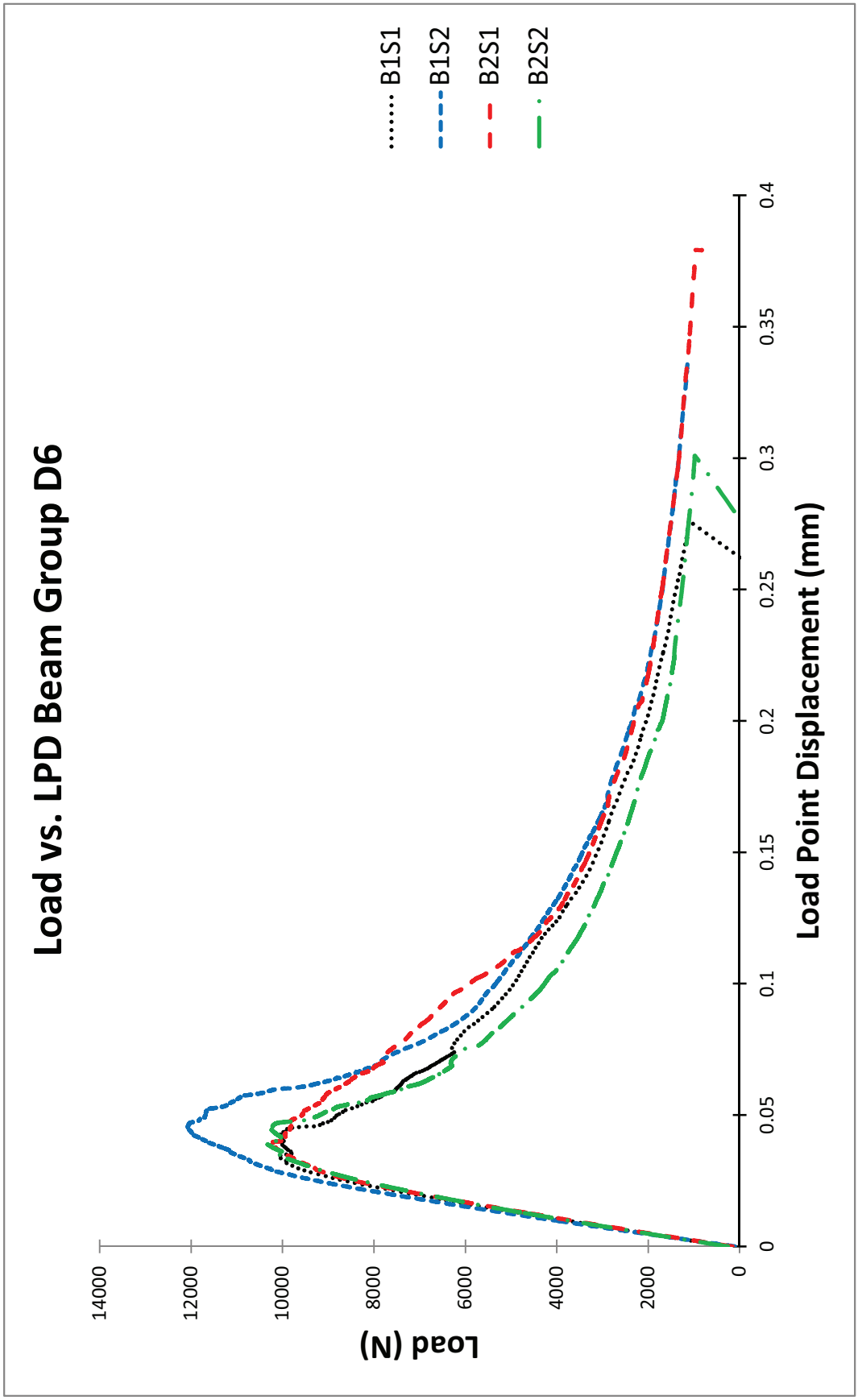

Figure 51: Load vs. LPD curves, Beam Group D6

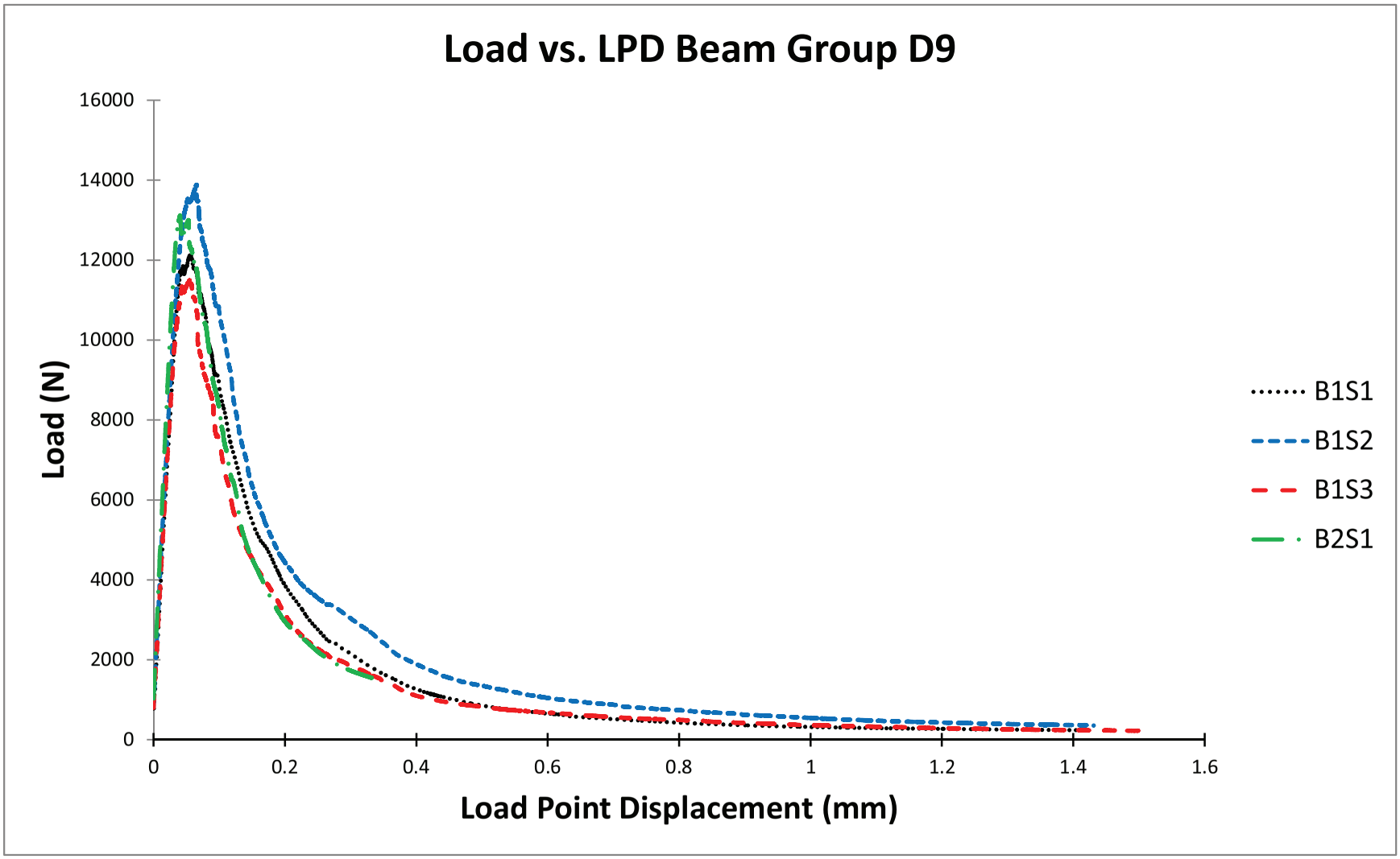

Figure 52: Load vs. LPD curves, Beam Group D9

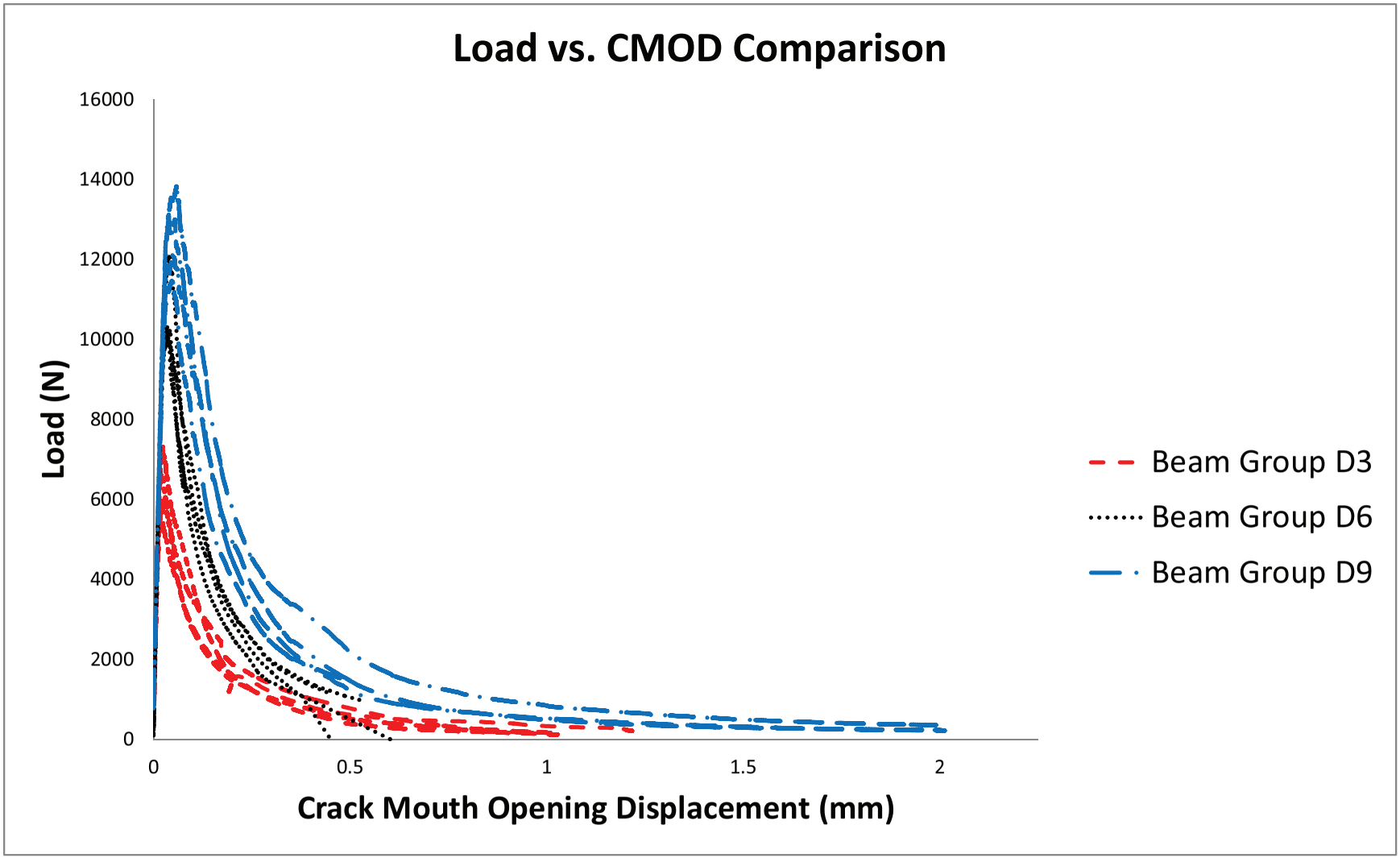

Figure 53: Load vs. CMOD comparison of all beam sizes

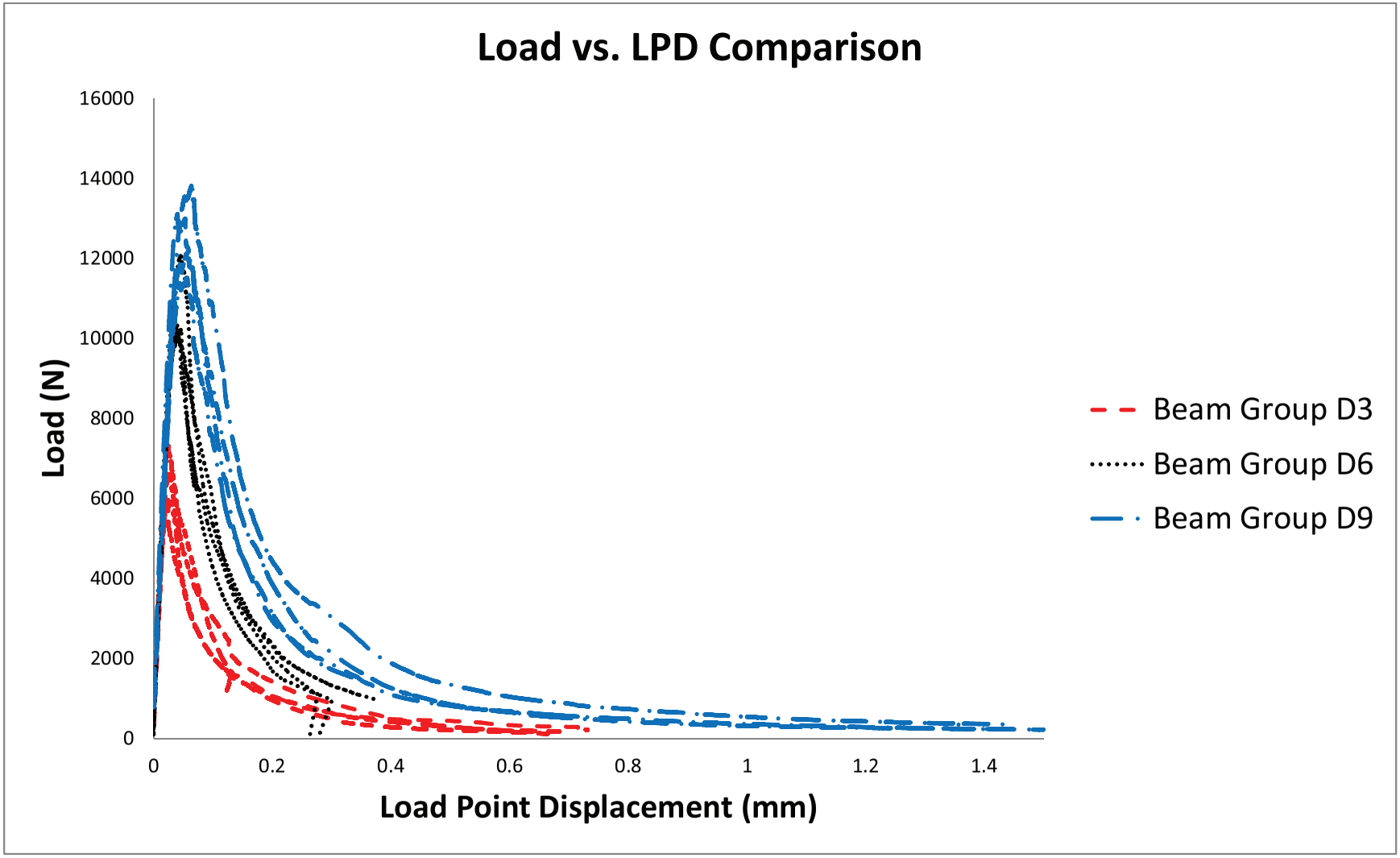

Figure 54: Load vs. LPD comparison of all beam sizes

Lastly, Table 11 shows the recorded peak load for each beam.

Table 11: Recorded peak loads

Beam Group A

Specimen	Peak Load (N)
B1S1	5,976
B1S2	5,897
B1S3	6,642
B1S4	7,315

Beam Group B

Specimen	Peak Load (N)
B1S1	10,071
B1S2	12,076
B2S1	10,213
B2S2	10,347

Beam Group C

Specimen	Peak Load (N)
B1S1	12,130
B1S2	13,885
B1S3	11,519
B2S1	13,318

As expected, the peak loads and the areas under both the load vs. CMOD and load vs. LPD curves increase with size. With the full curves, the data can be analyzed to procure the key fracture parameters of the concrete. Chapter 4 discusses the results and analysis of the data and the fracture parameters in detail.

4 RESULTS AND ANALYSIS

Given the load-deformation and load-CMOD curves of the specimens, the fracture parameters of concrete can be calculated using the equations in Chapter 4 of ACI 446-5, with their derivations and explanations provided in Chapter 2 of this thesis. The four parameters of interest to create the bilinear approximation of the softening curve of the concrete specimens are shown in Figure 55, and are defined as follows:

- f_t = tensile strength (obtained from splitting tension tests)
- w_1 = horizontal intercept of the initial portion of the softening curve
- w_c = critical crack opening displacement
- G_F = fracture energy, area under the softening curve

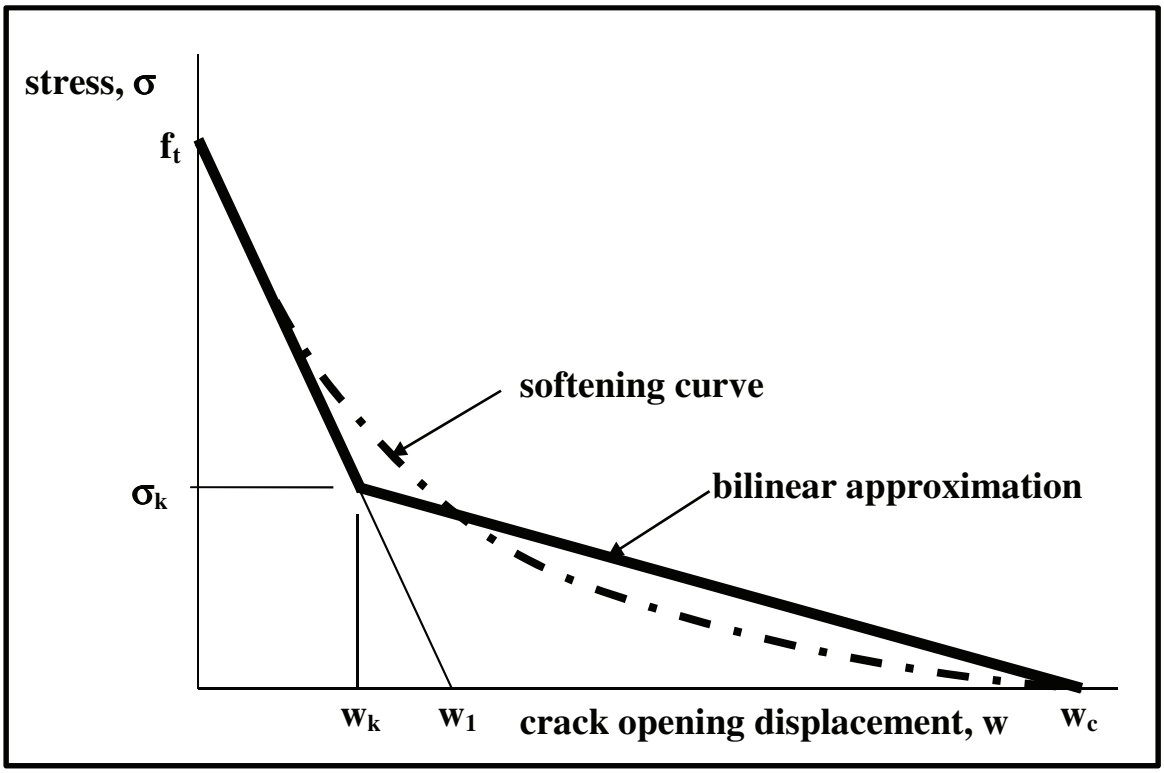

Figure 55: Bilinear approximation of the softening curve

Only the four above parameters are needed to completely define the bilinear approximation geometry, as w_k and σ_k are found through simple geometrical relationships. Also, in the calculation of these parameters, it will be shown that they are somewhat sensitive to small changes, and thus are prone to

measureable errors. The major contributor to these errors is the length of the far tail of the softening curve of the load-LPD and load-CMOD data. ACI 446-5 does not provide a lower limit either for the CMOD or LPD, only mentioning that the test may be ended after the CMOD has reached a value of 4D/300, as discussed above in Chapter 3. Due to having no restraint for minimum CMOD or LPD, tests with little data of the softening curve can be considered valid, which is an incorrect application of the cohesive crack model. Thus, a minimum achieved CMOD based upon the geometry of the specimen should be included in ACI 446-5 for the test to be valid. The author recommends a minimum final value of CMOD = D/100, based upon the acceptable data obtained from Beam Group D9 at a similar final CMOD values.

Section 4.1 of this chapter provides the bilinear approximations and analysis of the results for the specimens tested in Chapter 3, and Section 4.2 discusses the sensitivity of the fracture parameters to the length of the softening curve.

4.1 Bilinear approximations of the σ-COD curve

Using the corrected equations in Chapter 4 of ACI 446-5 (discussed in detail in Chapter 2 of this thesis), the fracture parameters for each specimen were calculated, and then for each beam size the results were averaged. The averaged values of the fracture parameters l_1, w_1, G_F, w_c, w_k, and σ_k are provided in Table 12.

Table 12: Fracture parameters for each beam series

Beam Group	l_1 (mm)	w_1 (μm)	G_F (N/m)	w_c (μm)	w_k (μm)	σ_k (MPa)	G_f (N/m)
D3	144.23	33.17	124.55	499.90	30.45	0.31	56.34
D6	125.79	27.90	88.95	280.04	25.24	0.35	47.38
D9	110.43	24.03	104.15	352.06	21.18	0.41	40.81

As noted in Section 2.2.1 of this thesis, the author believes the equation in Section 9.4.1 of Chapter 4 of ACI 446-5 for the calculation of P_{max} is incorrect. The values in Table 12 use equation (37) in lieu of the equation in ACI 446-5 to determine P_{max}. It is of interest to see what effect this change has on the final

calculation of the fracture parameters. For curiosity's sake, calculations were re-done using the incorrect equation to see the dependence of the fracture parameters upon the variation of P_{max}. The results are provided in Table 13.

Table 13: Fracture parameters using incorrect equation for P_{max}

Beam Group	l_1 (mm)	w_1 (µm)	G_F (N/m)	w_c (µm)	w_k (µm)	σ_k (MPa)	G_f (N/m)
D3	137.06	31.52	124.55	477.01	28.73	0.33	53.52
D6	111.20	24.66	88.95	248.85	21.73	0.43	41.88
D9	106.97	23.29	104.15	347.16	20.40	0.43	39.55

As expected, small variations are evident in the parameters that utilize P_{max}. Although the changes are small, the results of Table 13 are still an incorrect application of the theory of the bilinear cohesive crack model, and the equation in Section 9.4.1 of Chapter 4 of ACI 446-5 must still be changed.

Using the correct values in Table 12 , the data points were plotted on graphs of stress vs. crack-opening displacement. Bilinear approximations were determined for every specimen for comparison purposes. Figure 56, Figure 58 and Figure 60 show the averaged bilinear approximation for Beam Groups D3, D6 and D9 respectively, while Figure 57, Figure 59 and Figure 61 show bilinear approximations for each individual specimen compared to other specimens in that beam Group. Lastly, Figure 62 shows a comparison between beam groups of the averaged bilinear approximations.

As one can see, the results for each beam size match up fairly well. The major anomalies come from Beam Group D6, where there is a noticeable decrease in the fracture energy, G_F, and subsequently a drastic decrease in the critical crack opening displacement. This makes some sense, as due to the problems in achieving a full softening curve discussed in Chapter 3, the work of fracture was much less. Theoretically, the far tail constant should compensate for this problem, but it relies on the assumption that the tail is asymptotically approaching zero-load, which may not be the case for data close to the initial linear portion of the stress vs. COD curve.

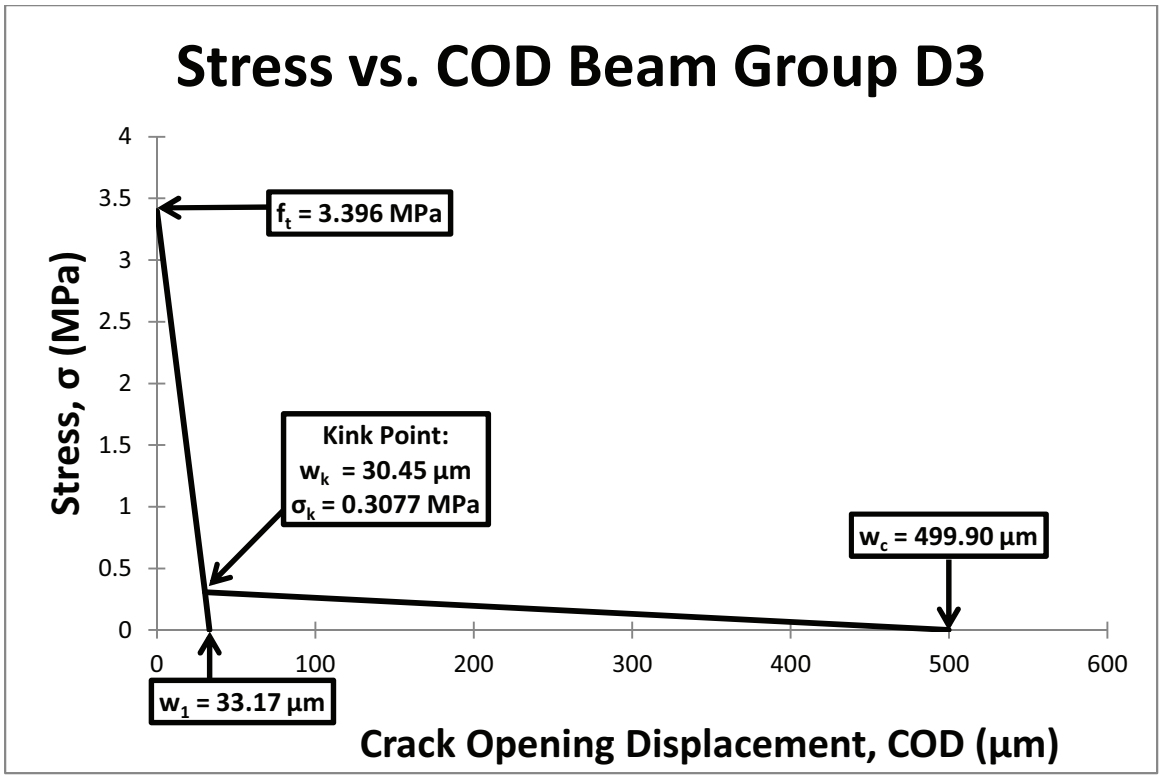

Figure 56: Bilinear approximation for Beam Group D3

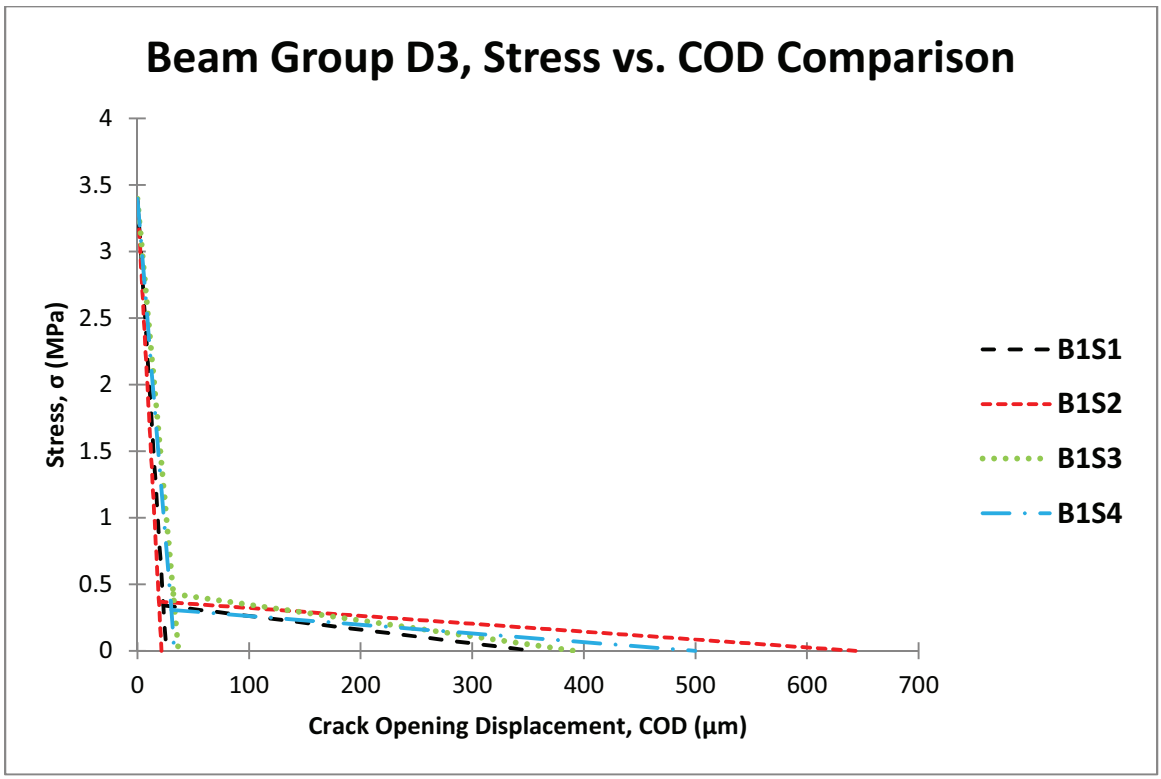

Figure 57: Comparison of bilinear approximations, Beam Group D3

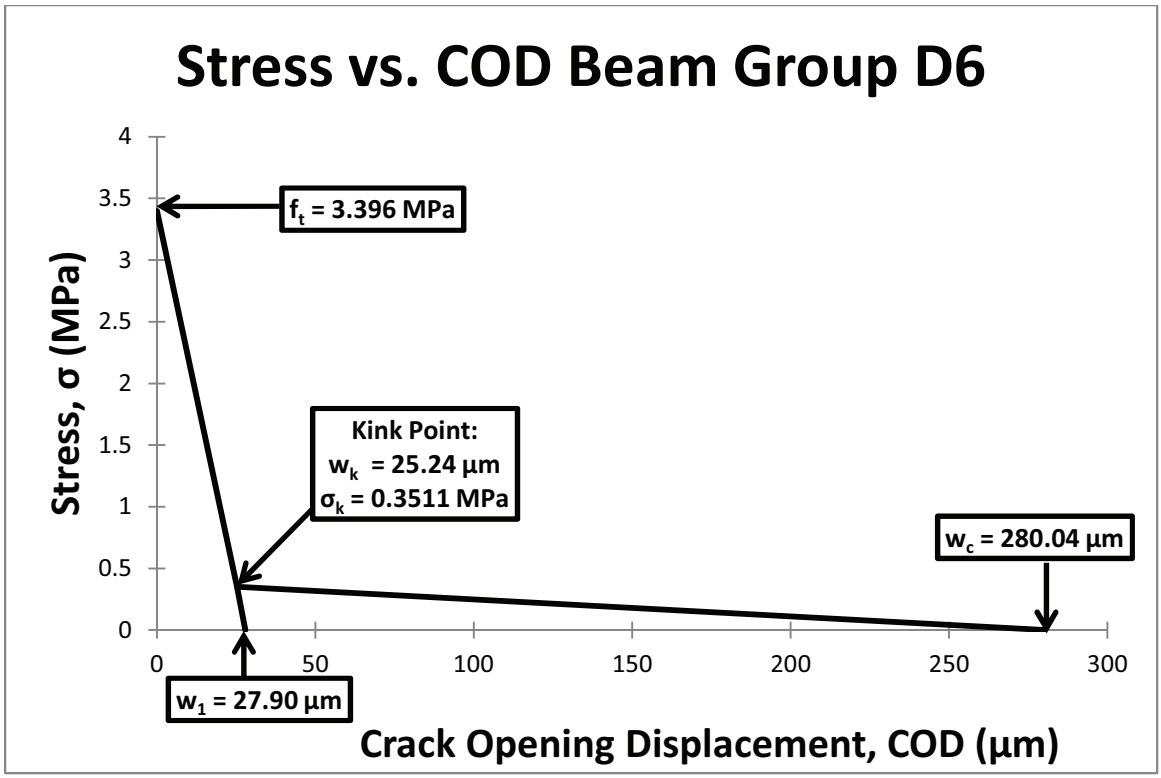

Figure 58: Bilinear approximation for Beam Group D6

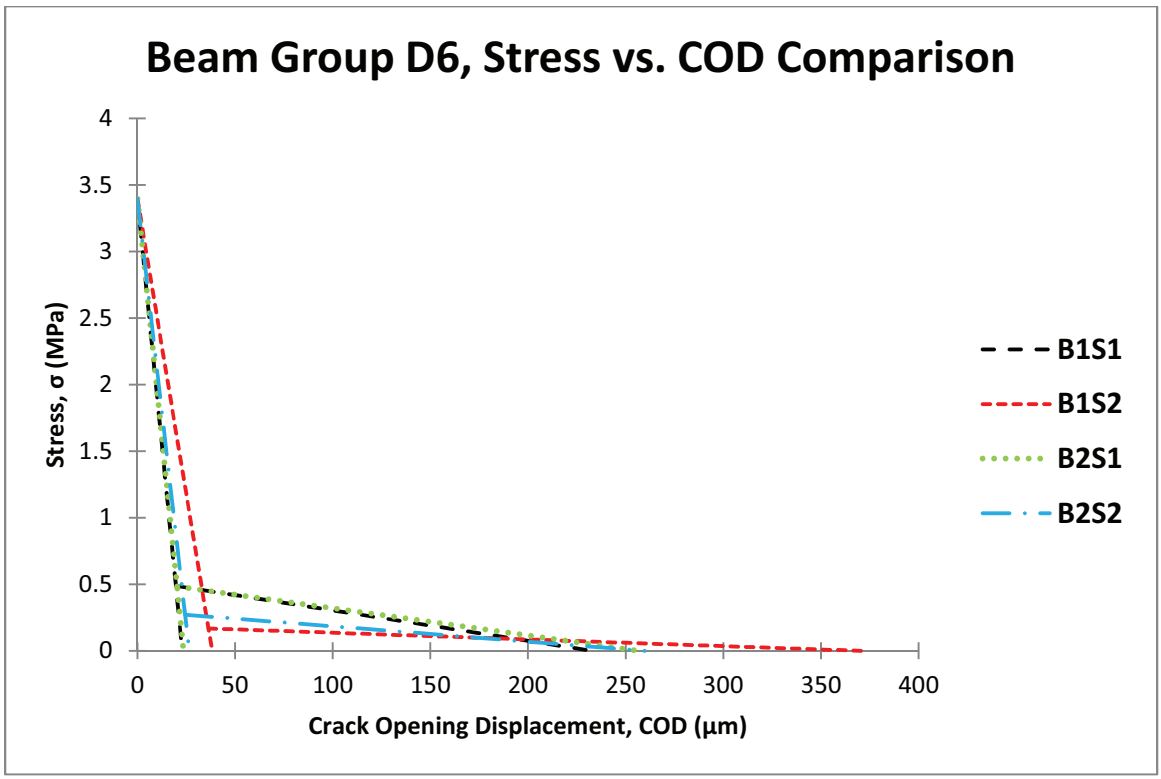

Figure 59: Comparison of bilinear approximations, Beam Group D6

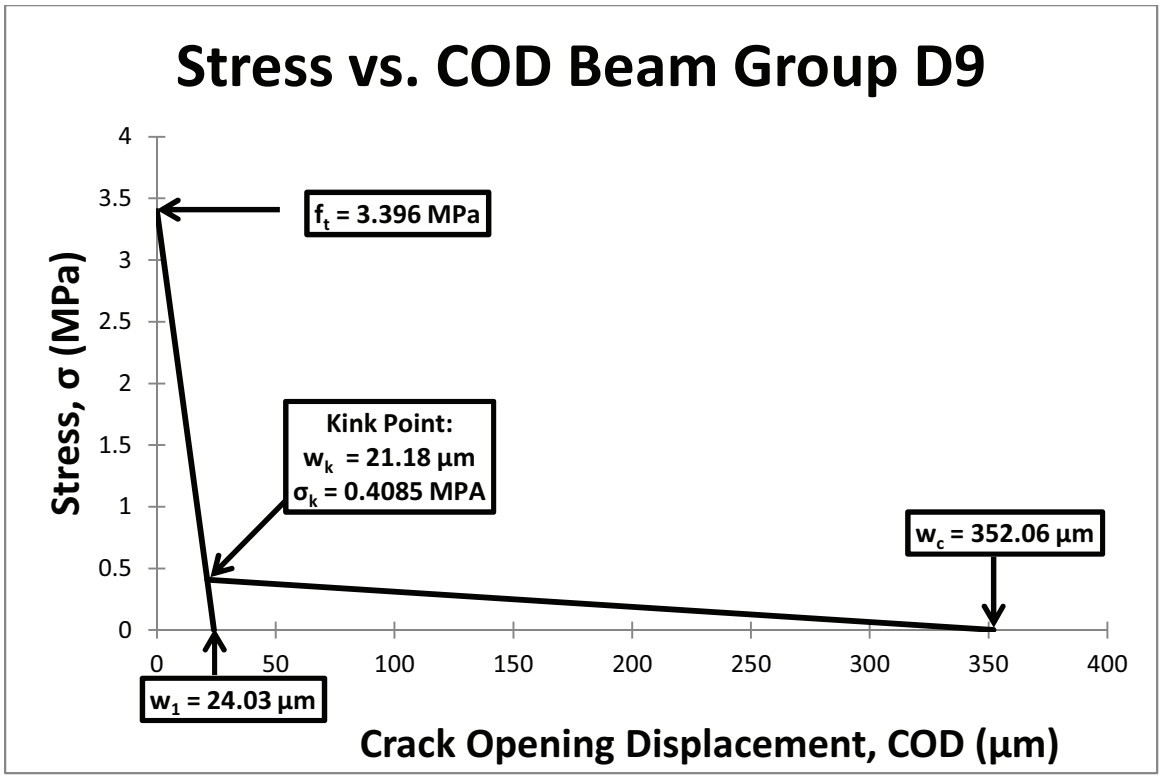

Figure 60: Bilinear approximation for Beam Group D9

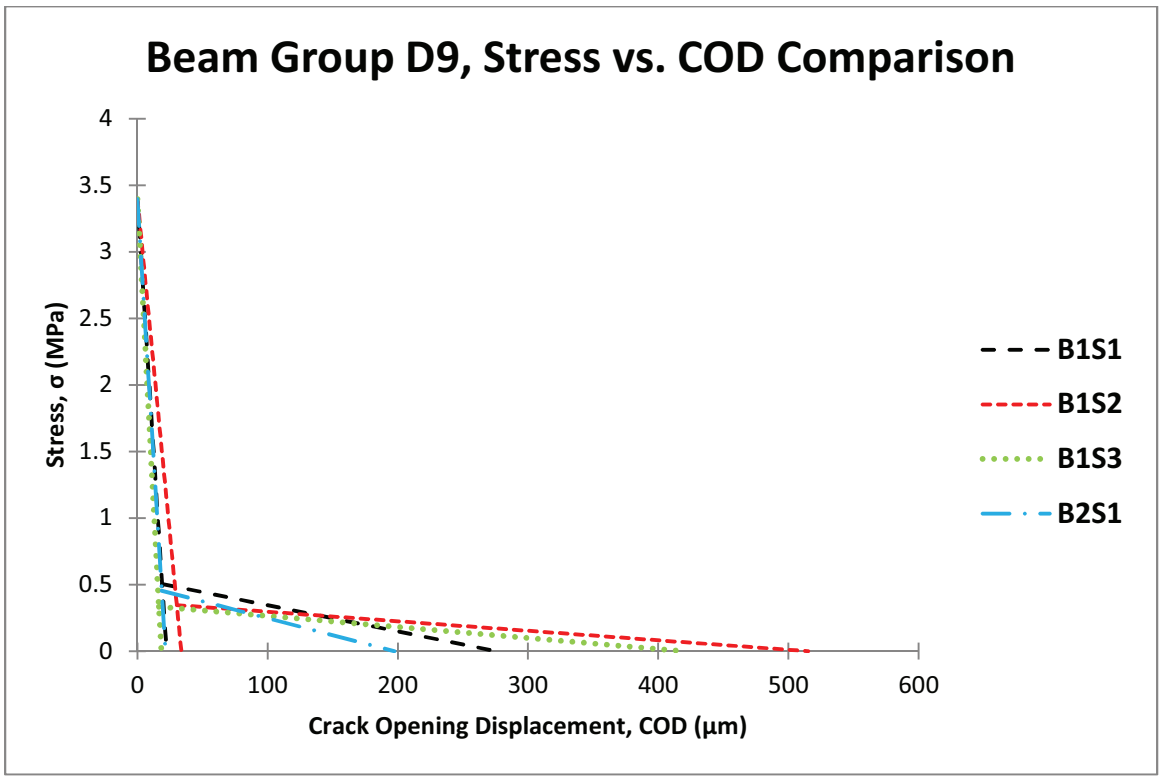

Figure 61: Comparison of bilinear approximations, Beam Group D9

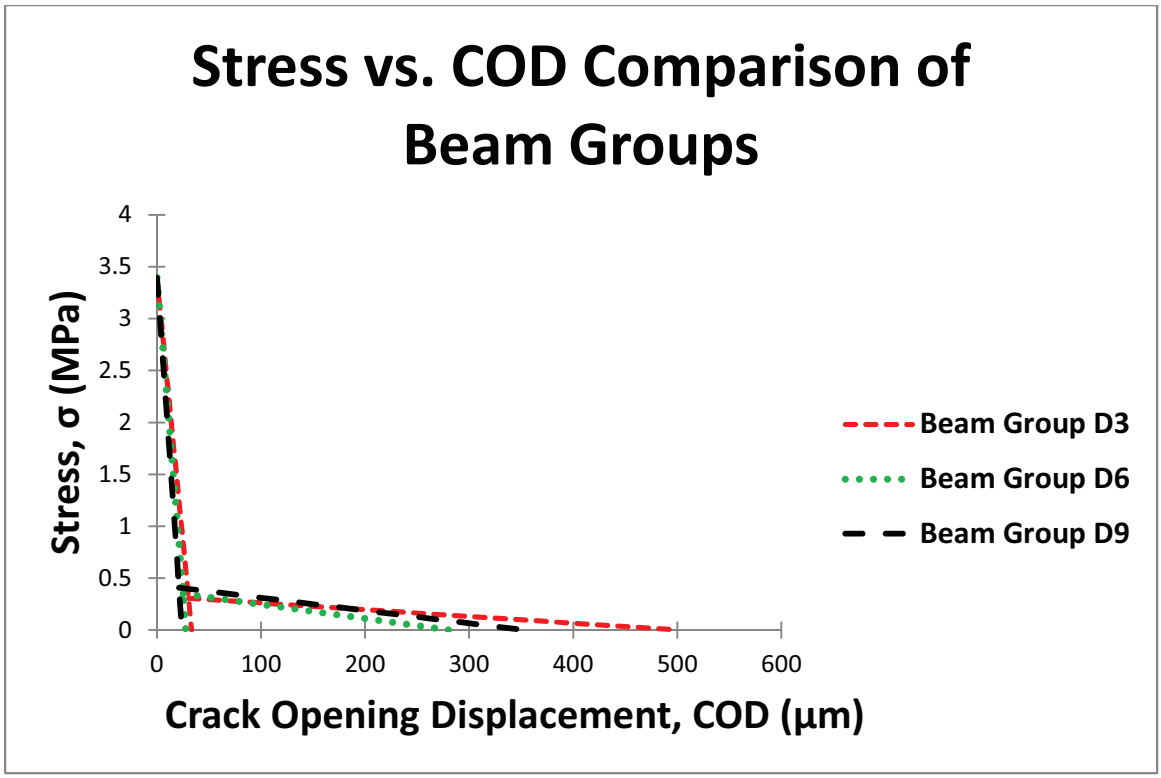

Figure 62: Comparison of bilinear approximations, all beam groups

Note that while the averages of the bilinear approximations do not show a great degree of variation, this cannot be said for the individual specimens in each beam group. The high degree of variability among the results of specimens within a beam group is concerning, and the author believes further testing using a large number of specimens should be conducted so a statistical analysis of the variability can be performed.

Initially, it appears that the far tail constant does not do a sufficient job in correcting for the lack of a long softening tail if a sufficiently large CMOD is not reached before testing is ended. However, before this can be concluded, further analysis must be done to determine the effect of the length of the tail of the softening curve on the calculation of the key fracture parameters. This is shown later in Section 4.2, which provides a sensitivity analysis of the tail of the softening curve for each of the major fracture parameters. Unfortunately, due to the anomalous data from Beam Group D6, it is not possible to draw definite conclusions about any potential size dependence of this test method.

However, it is possible to make some conclusions on size dependence for the initial portion of the softening curve, represented by the initial fracture energy G_f. The averaged values of Gf for each beam group are shown in Table 14.

Table 14: Values of G_f for each beam type

Beam Group	Gf (N/m)
D3	56.34
D6	47.38
D9	40.81
Standard Deviation	7.792

As one can see, there is a downward trend, showing some size dependence, with the difference between Beam Group D3 and D9 being over 20%.

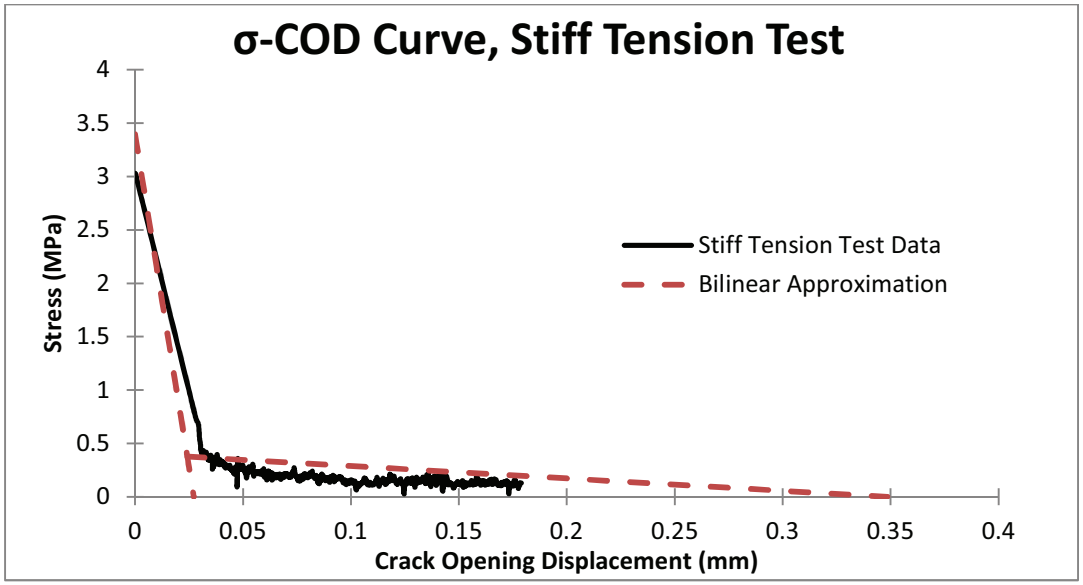

Figure 63: Stress-COD curve for Stiff Tension Test

Lastly, for comparison purposes, a stiff tension test conforming to the procedures of Lenke and Gerstle was performed using a 6 in. diameter concrete cylinder cast with Batch 1 of the concrete [Lenke & Gerstle, 2009]. This test provides an alternate method for determining the fracture energy, G_F, using a

notched cylinder under direct tension in a stiff testing apparatus that confines all but the central portion of the cylinder so that stable and predictable crack grown will occur [Lenke & Gerstle, 2001]. Using the data from the test, a stress vs. crack opening displacement curve was plotted, and the fracture energy, G_F found by integrating under the curve. The graph and results from the test are shown in Figure 63 alongside the average bilinear approximation of all the NBLII tests.

As one can see, the results are similar to that of the NBLII tests, with the stiff tension test resulting in a calculated G_F = 93.9 N/m. It is noted that w_c appears to be very different, however this is easily explained as the variability of w_c is high even amongst the NBLII tests (note from Table 12 the average value of w_c for Beam Group D6 is 0.242 mm, which appears to match well with the stiff tension test). Despite these obvious differences, the results received from the stiff tension test provide at least a measure of confidence of the validity of ACI 446-5 test method through the similarity of the calculated fracture parameters.

4.2 Sensitivity analysis of the softening curve

As discussed in the results above, investigation of the sensitivity of the calculation of the fracture parameters to the length of the softening curve is required in light of to the large difference in the fracture parameters calculated from the data in beam group D6 from the other sizes. In general, the specimens in beam group D6 obtained roughly 20% of the recommended final CMOD value, while the specimens from beam groups D3 and D9 in general performed much better with the utilization of the stroke control testing method. For comparison purposes, it is feasible to truncate data from beam groups D3 and D9 to mimic real tests that end before the maximum allowable CMOD is reached, and a sensitivity analysis can be performed to see how the fracture parameters change as more and more data is truncated. The methodology of this sensitivity analysis is explained below.

Figure 64 depicts a graphical representation of a typical load vs. CMOD curve from an NBLII test, where the test is cut off at a maximum value w_{MR}. For the sensitivity analysis, iterations were performed where larger and larger

portions of data were excised, and the parameters of G_F, w_1, and w_c were recalculated. The value X represents the amount of data excised, where all data corresponding to a CMOD greater than $w_{MR} - X$ would be excised. One hundred iterations were performed using this process, from $0.2w_{MR} \leq X \leq w_{MR}$.

A MATLAB® program was written by the author to automate this process, seen in Appendix A. The program reads in raw data from a text file specified by the user, as well as a text file with specimen dimensions, and then performs all the calculations of Chapter 4 of ACI 446-5, determining the fracture parameters. It also has the capability to perform the sensitivity analysis by truncating data at a user-specified interval.

The program was repeated for six specimens in total, three from beam group D3, and three from beam group D9. Specimen B1S2 from group D3 was not used due to an anomaly in the data curve, and Specimen B2S1 from group D3 was not used due to the specimen having an insufficiently long softening curve.

Figures 65 through 67 show the sensitivity of G_F, w_1, and w_c respectively from beam group D3, while Figures 68 through 70 show the same values for beam group D9.

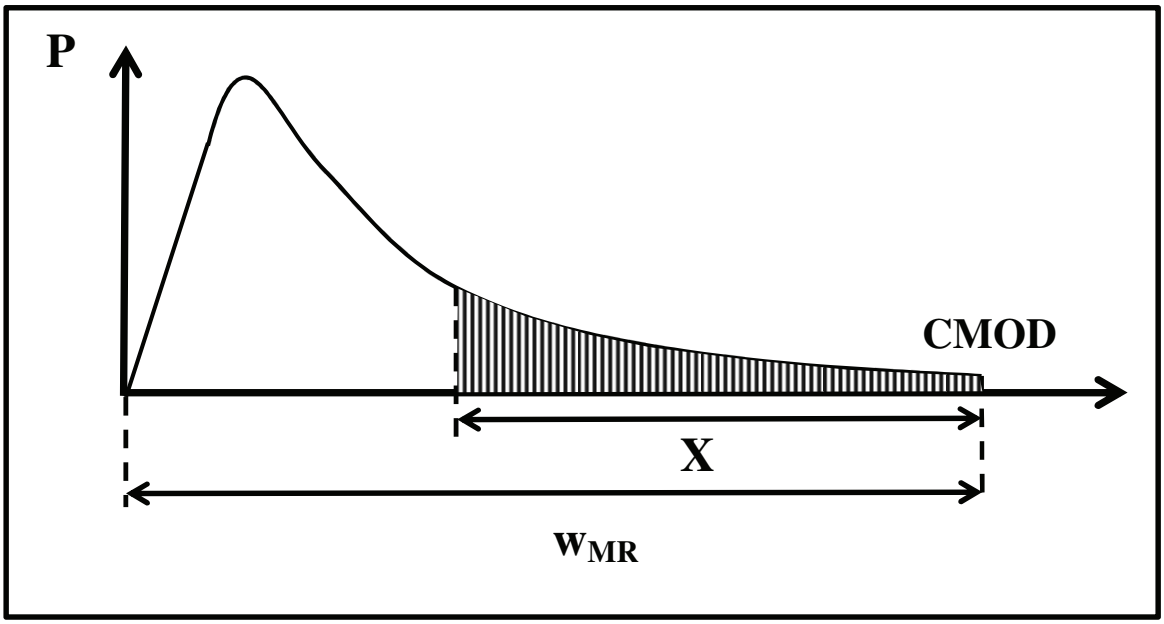

Figure 64: Load-deformation curve where X represents the amount of excised data

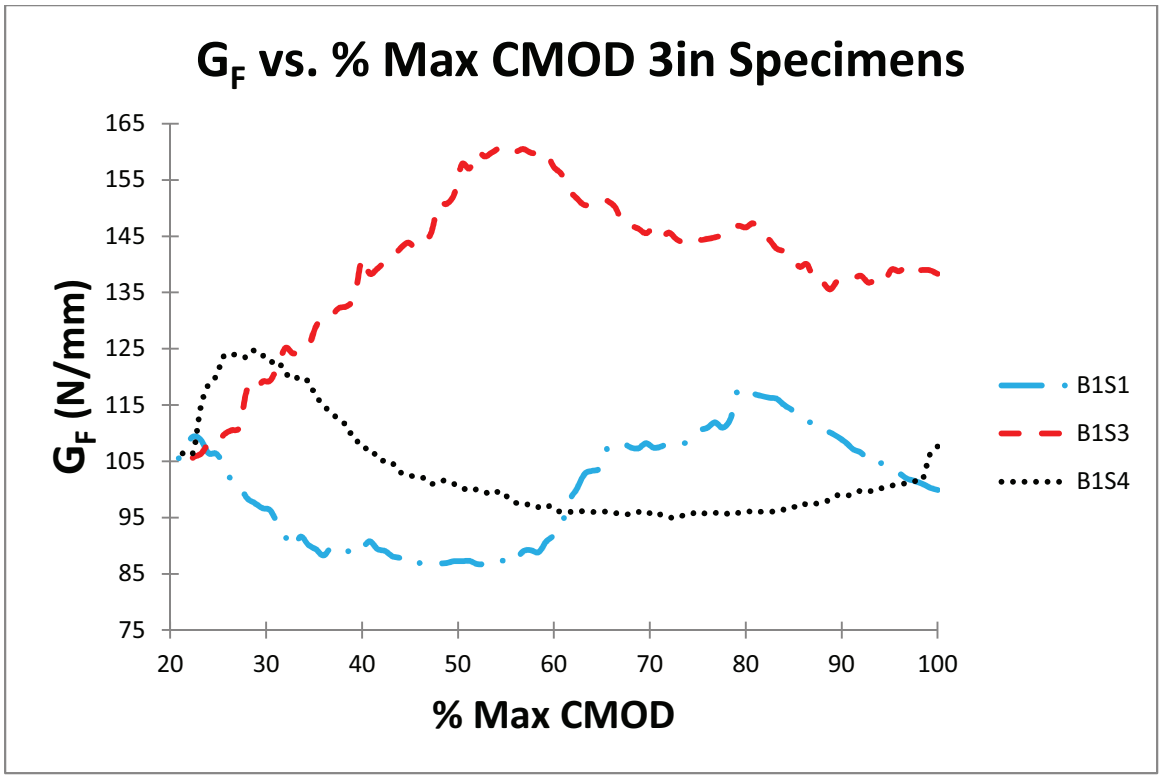

Figure 65: Sensitivity of GF, 3in specimens

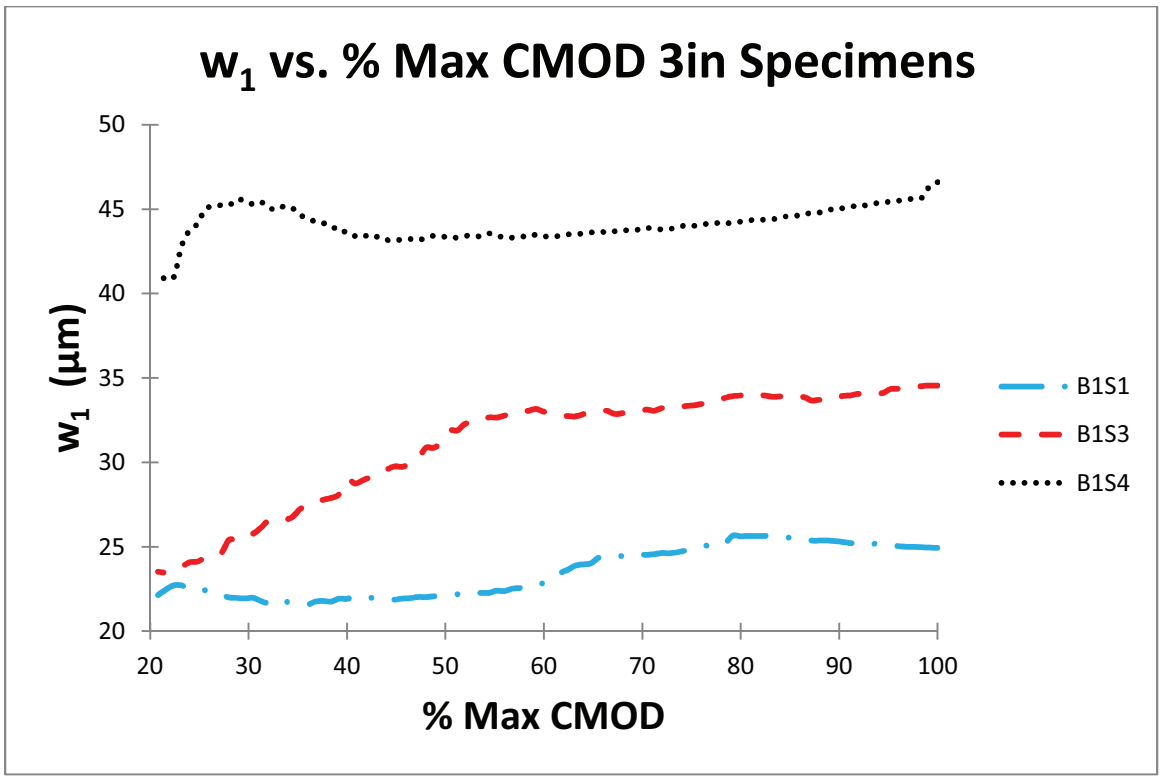

Figure 66: Sensitivity of w1, 3in specimens

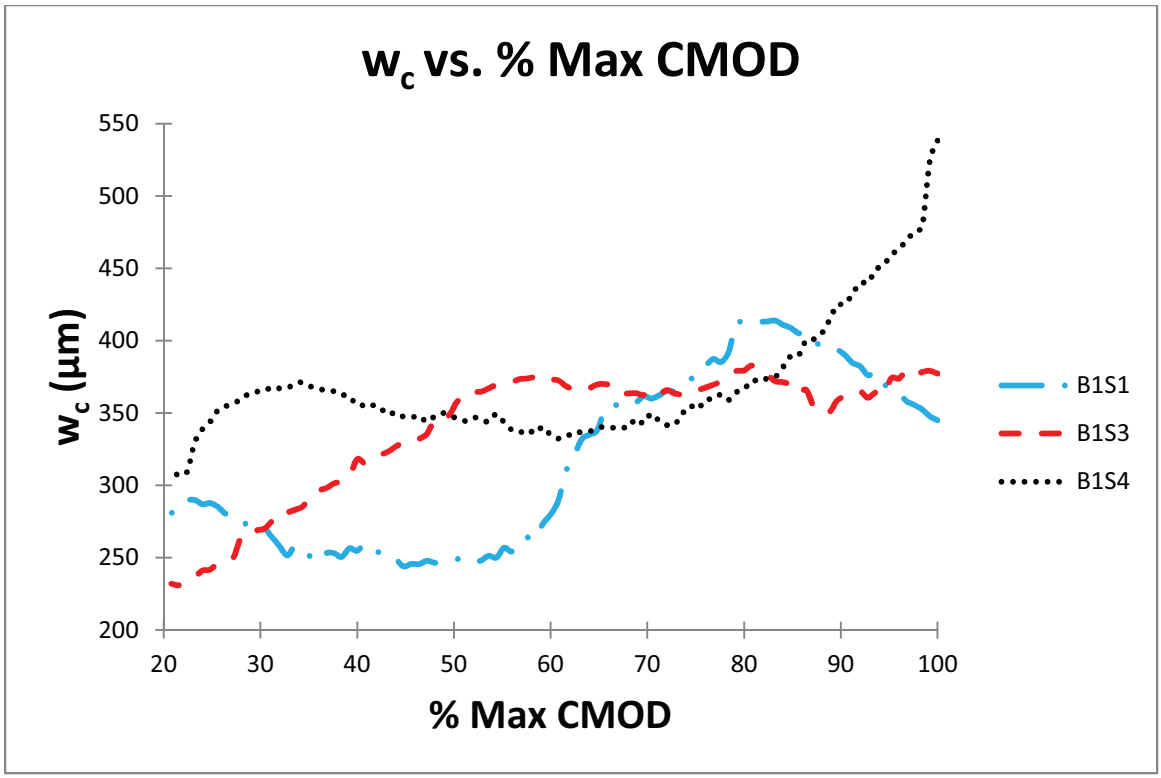

Figure 67: Sensitivity of wc, 3in specimens

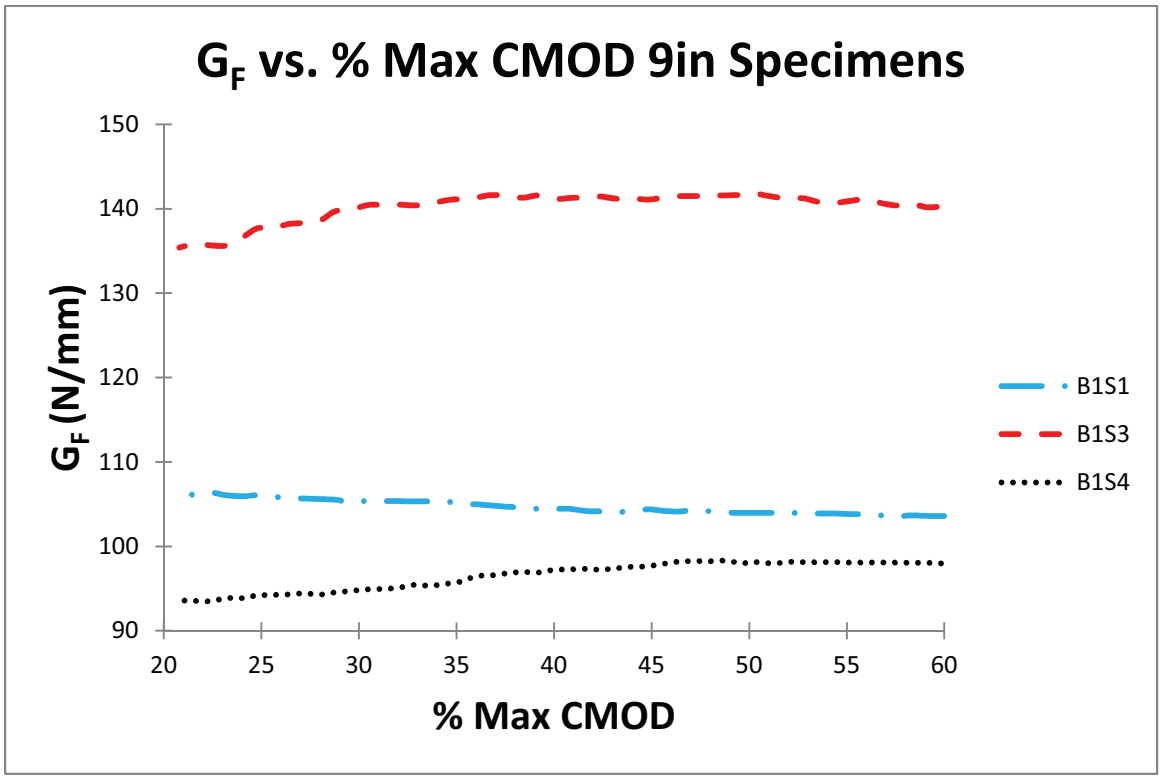

Figure 68: Sensitivity of GF, 9in specimens

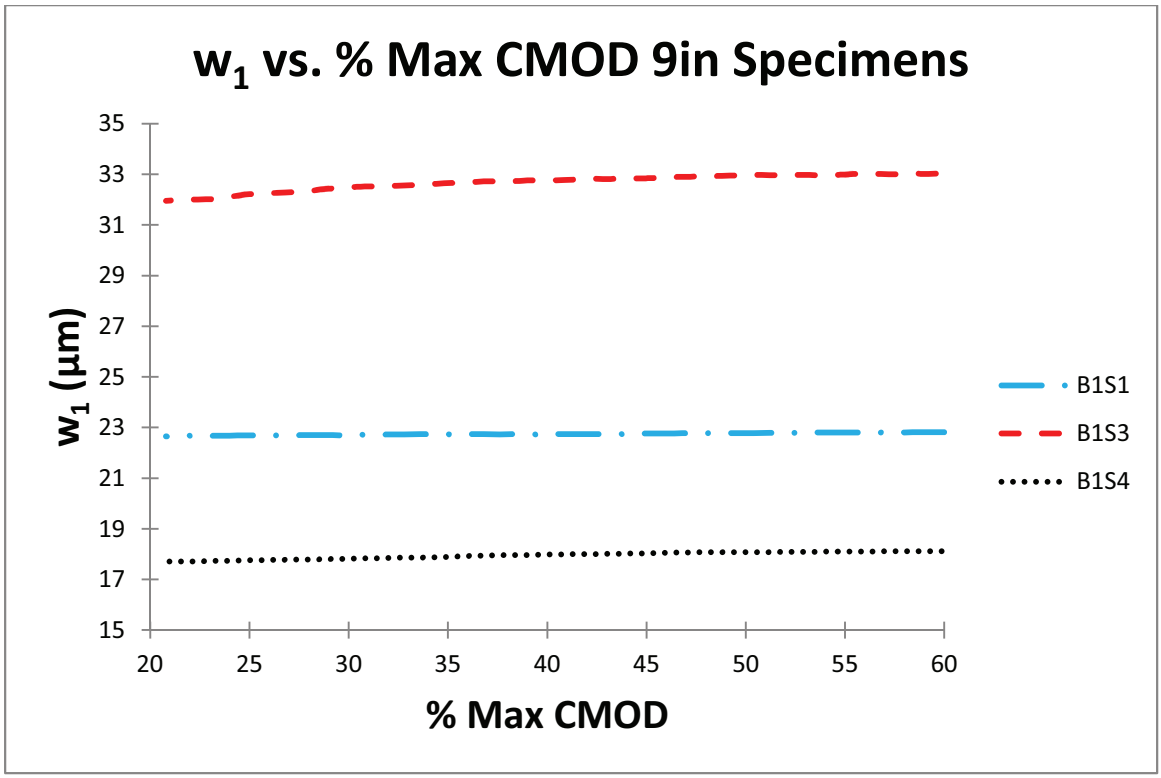

Figure 69: Sensitivity of w1, 9in specimens

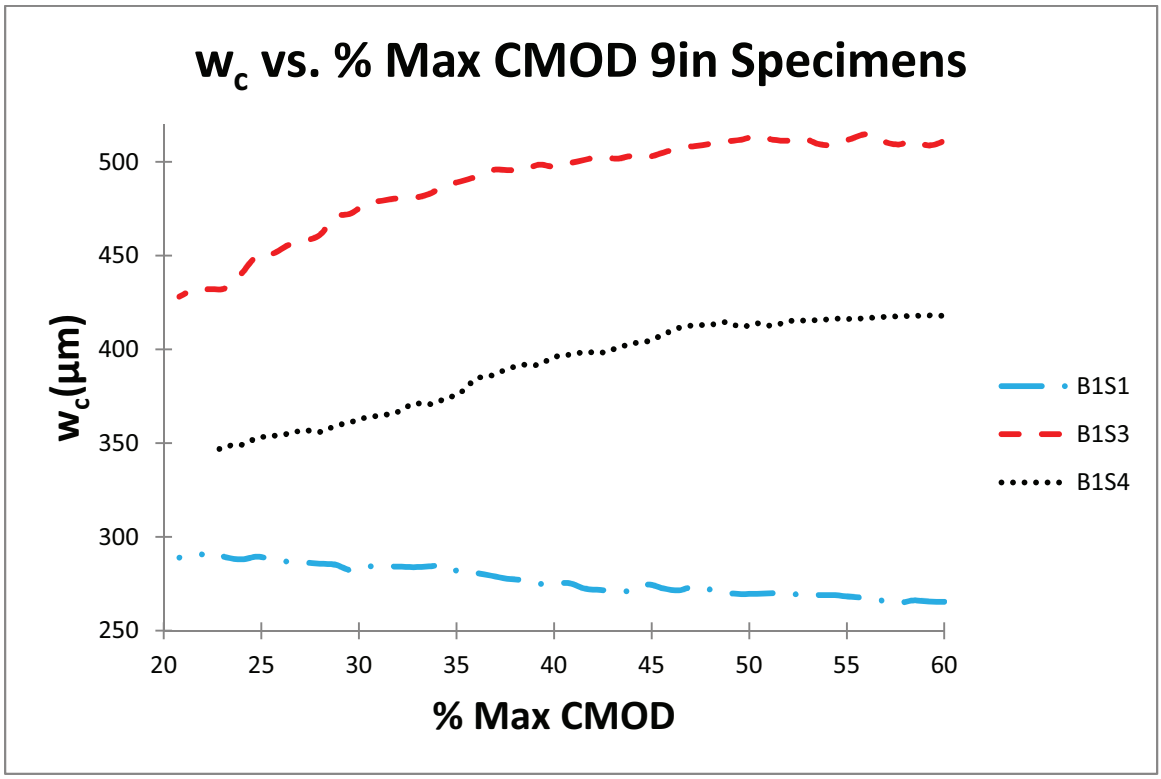

Figure 70: Sensitivity of wc, 9in specimens

As one can see, in many cases the parameters show considerable sensitivity to the length of the softening curve. In particular, the specimens in beam group D3 appear to have a wide range of variability. However, this variability may be exaggerated by a few factors. It is possible that due to the large size of the aggregate with respect to the beam depth that the data obtained from the tests are more erratic than with the other-size beams due to the behavior of crack propagation around the relatively large aggregate. The analysis of the specimens from beam group D9 show more stable behavior, and in the case of w_1 and G_F, they vary only slightly, by as much as 5-10%, showing general trends toward reaching a single value as more data is available at the end of the softening curve. The value of w_c varies by as much as 40% between tests, though it also shows a general trend of approaching a single value as more data is available at the end of the softening curve.

Given the high degree of variability of these fracture parameters with the excising of data from the softening curve, it can be concluded that achieving a fuller softening curve is a necessity for proper calculation of the fracture parameters using the test methods outlined in ACI 446-5, of which the author makes the recommendation of a final CMOD = D/100 in Chapter 3.

This analysis also casts into doubt the values obtained from the specimens in beam group D6, as had more data from the softening curve been obtained, the calculated fracture parameters may have more closely matched those of the specimens in beam groups D3 and D9.

Based upon the results and analysis of these tests, several recommendations will be made for improvement of the test method proposed by ACI 446-5; these will be discussed further in the final chapter.

5 SUMMARY AND CONCLUSIONS

As design codes become more sophisticated, it is inevitable that the research performed in the field of fracture mechanics will be implemented in one fashion or another. However, for design of concrete structures, currently even the most contemporary design codes still use the compressive strength, f'_c, as the primary, and in many cases the *only* material property determined from experiments. Not only does f'_c do a poor job in describing the post-ultimate behavior of concrete, it also has shown much size dependence, and is ultimately an inadequately and grossly overly-simplistic parameter.

However, f'_c does, for the most part, meet the criteria outlined in Chapter 1 for a good test method. The determination of f'_c is a simple, inexpensive test method with a single simple calculation to determine its value. Part of the popularity of f'_c is due to its simplicity and applicability. For the parameters derived from fracture mechanics to eventually find themselves in modern design codes, the test methods to determine them must also show similar qualities to that of the compressive strength test. ACI 446-5 NBLII test takes a step in the right direction by providing a relatively simple and inexpensive method for determining key fracture parameters of concrete using notched beam tests. However, there are several faults with the method that must be addressed. Discussed below, Section 5.1 will summarize the test method and results found in this thesis in a general way, as well as providing conclusions about the applicability of ACI 446-5. Lastly, Section 5.2 will provide recommendations for alterations and for further research to supplement and improve upon ACI 446-5.

5.1 Summary and Conclusions

Three different beam sizes of normal-strength concrete were tested using the NBLII testing method outlined in ACI 446-5 and their fracture parameters calculated assuming a bilinear cohesive crack model. While no size effect conclusions could be made due to anomalous data with beam group D6, the test method itself proved to be as simple as apparently possible. Many of the major concerns in the calculation of these fracture parameters have been put to rest by

careful consideration by the writers of the test method in determining the outside factors that may influence the test method.

However, several issues arose from the tests performed and described in this thesis. In select cases, there are non-trivial errors, ambiguities and impractical testing methods that must be modified before a final test method is adopted. For instance, the equation in Section 9.6.3 of Chapter 4 of ACI 446-5 is obviously incorrect, and must add a term to translate values of displacement to those of CMOD. Luckily, as shown in Chapter 4, the fracture parameters are not particularly sensitive to the needed change, but it is worrisome that the error in this equation was overlooked.

Secondly, the provenance and reasoning for several equations in ACI 446-5 are not properly cited, and in some cases do not exist in the literature. Although some measure of provenance has been provided in this thesis, the testing method itself needs to be the subject of more scrutiny before it is adopted.

Lastly, an important problem was discovered in determining that the fracture parameters are quite sensitive to the amount of data available in the tail of the softening curve. ACI 446-5 makes no effort to define a minimum CMOD that must be achieved for the test to be valid. Thus, specimens that experience dynamic instability leading to the end of testing can be considered valid, when the fracture parameters calculated from such tests could vary by as much as 40% compared with specimens with a well-developed softening curve.

To help solve these problems, recommendations for improvement are made below by the author.

5.2 Recommendations

ACI 446-5 contains some errors, ambiguities and impractical testing methods, as is expected from a draft test method. A major objective of this thesis was to identify such errors and provide suggested corrections and recommendations for changes to ACI 446-5. While many of these problems are rather trivial and easily corrected, some of them require further research to assure the NBLII testing method of ACI 446-5 is a valid and practical testing

procedure for the determination of key fracture parameters. The author recommends a series of changes to the ACI 446-5, in both general and specific cases. Below is a detailed list of specific recommendations by the author for changes to sections of Chapters 2 and 4 of ACI 446-5, followed by a list of more general recommendations:

- Chapter 2, Section 6.4.2: It is impractical to keep the specimen surfaces moist during the entirety of the test, and this requirement should be relaxed or eliminated. The author suggests keeping the specimen surfaces moist only until the clip-gauges and LVDTs have been attached, after which there is no requirement to keep the specimen surfaces moist. However, a requirement of the test being completed within 45 minutes to 1 hour of the concrete starting to dry is reasonable.
- Chapter 2, Section 7.3.3: Figure 2.5 (a) is in error, where the double-span sized specimen creates zero moment at center-span, when it should produce a slight negative moment. Figure 2.5 (a) should be changed to reflect a center-span negative bending moment.
- Chapter 2, Section 7.4.3: It is often impractical to glue within $0.25a_0$ from the notch centerline for smaller specimens, and gluing larger sections does not appear to have any impact on the test results. This requirement should be removed, or fully explained with cited works.
- Chapter 2, Section 7.6.3: It is not explicitly said whether a test is valid if the test ends before a CMOD value of 4D/300. Based upon the findings of this thesis, the author recommends that a minimum CMOD value of D/100 be achieved for a test to be considered valid.
- Chapter 2: Section 8.2.3: The author recommends that this section be deleted, as the pre-loading has little, if any, effect on the results. In particular, any initial seating non-linearity was unnoticeable in specimens that had little to no pre-load. In lieu of this, the section contains ambiguous language, and should specifically state whether the pre-load is to be recorded as part of the useable test data, or excised.

- Chapter 2, Section 8.2.5: Exclusive CMOD control has proven inadequate for attaining a full softening curve, and an alternative method should be developed using machine stroke control to prevent dynamically unstable breaking of the specimen. This should be left open to the user, as different machines will have differing control requirements.
- Chapter 4, Section 9.3: A provision should be made in the case that the pre-load is larger than the residual load, so that w_{ma} and δ_a can be assumed to be a reasonable value of zero.
- Chapter 4, Section 9.3.1: Remove the requirement of choosing P'_R corresponding to a CMOD = 2 mm or the nearest point on record, and instead have P'_R correspond to the last point on record, with a provision to use engineering judgment to excise data in the case of any outlying final data points.
- Chapter 4, Section 9.3.4: An in-line citation, explanation or appendix should be added to clarify the need to use values of CMOD over those found in the literature using values of LPD.
- Chapter 4, Section 9.4.1: The equation for P_{max} should be changed to match that of either equation (35) or equation (37) to account for the change of a span-to-depth ratio of 3.
- Chapter 4, Section 9.5.1: An in-line cited reference or appendix should be added to explain or derive the equation to determine l_1.
- Chapter 4, Section 9.8.3: A cited reference or appendix should be added to explain the derivation of the equation to determine w_c.
- Appendix 4.1: The author suggests that the following references from this thesis be added to the reference list
    - Guinea et al. (1998)
    - Bazant and Planas (1998)
    - This thesis
- In general: In-line citations for the originations of the equations used in Chapter 4 of ACI 446-5 could prove very useful to many testers, as even

the basic principles of the cohesive crack model are complex and require a good deal of research to understand.

Finally, the author suggests several areas where further research is necessary to determine the validity of the NBLII test of ACI 446-5. The most pressing area needing of further research is in addressing the issues with the tail of the softening curve. It was found by the author that switching to machine stroke control after initially using CMOD control proved sufficient in developing a long softening curve tail that regularly reaches to the maximum allowable CMOD outlined in ACI 446-5. However, the method for finding the appropriate timing and rate of machine stroke control is based heavily upon trial and error, and is only a temporary solution to a greater problem. More research is suggested in this area to fully understand why specimens experience dynamic instability at relatively high residual loads. By examining how machine stroke is applied over time based upon CMOD control, it is possible that a new method that only uses stroke control to prevent dynamic instability could be developed. Currently, the method outlined in this thesis only has proven useful for normal strength concretes, as higher strength concretes exhibit sizeable and sudden crack growth at the onset of stroke control, thus violating the maximum CMOD growth rate allowed by ACI 446-5.

Also, further research should be conducted to find an acceptable minimum allowable CMOD value for the test to be considered valid. The author's suggestion of a CMOD = D/100 is based off of only three successful test specimens of one size. More testing must be done to assure that this value is appropriate for different sized specimens and concrete types.

Lastly, it is suggested that further testing be done in an attempt to determine the existence of size dependence of this testing method. Due to the sensitivity of the fracture parameters of the cohesive crack model to the tail of the softening curve, the tests for beam group D6 must be considered invalid, and consequently size effect cannot be determined definitively from this thesis. It may be useful and prudent to do large numbers of tests at different sizes so that statistical analysis may also be used.

Appendix A

This Appendix contains the MATLAB® functions used to determine the bilinear cohesive properties from raw data obtained from testing.

```
function bilinear_approximation
% This function determines key fracture parameters for the NBLII test.
% Written by: Scott Chapman
% Modified: 8/02/2011
%pre_load = 730.00; %pre-load in Newtons
ft = 3.396363147; %splitting tensile strength in MPa, taken from
Brazilian tests
specimen = 'spec64.txt';
S = 25.4*18; %Span length, mm
% D = 228.50; %Average Depth of specimen, mm;
% B = 151.48; %Average Width of specimen, mm;
% a0 = 80.40; %Average Notch Depth of specimen, mm;
[dim, Pc, LPDc, CMODc] = get_data(specimen);

D = dim(1);
B = dim(2);
a0 = dim(3);
b = D-a0;
h = 1.5748; %Distance of the knife edges to specimen surface, mm

max_CMOD = 2; %Max crack mouth opening displacement allowed, mm
%Read in all relevant data


%Sensitivity analysis begins at 100% of the desired final CMOD range,
and
%then does a number of iterations down to 20% of the final CMOD and
finds
%key fracture parameters for each iteration.  This tests the validity
of
%the far tail constant, A, and its effect on the fracture parameters

num_iter = 100;%number of iterations for sensitivity analysis

%read in data for sensitivity analysis
percent_reduction = 0.8/num_iter;
CMOD_holder = max_CMOD;
for j = 1:num_iter
    for i = 1:length(Pc)
        if CMODc(i) < CMOD_holder
            P(i,1) = Pc(i);
            CMOD(i,1) = CMODc(i);
            LPD(i,1) = LPDc(i);
        end
    end
    [E(j,1), fp(j,1), l1(j,1), w1(j,1), GF(j,1), wg(j,1), wch(j,1),
wc(j,1)...
        , ok(j,1), wk(j,1), Gf(j,1)]=
fracture_toughness(P,LPD,CMOD,B,D,...
```

```
        a0,ft,S, max_CMOD,b,h);
    %prep CMOD_holder for next iteration
    CMOD_holder = CMOD_holder * (1 - percent_reduction);
    %free up memory
    P = [];
    CMOD = [];
    LPD = [];
end

%Data to be used in excel files
props = [E, fp, l1, w1, GF, wg, wch, wc, ok, wk, w1, Gf];

return
```

```
function [E, fp, l1, w1, GF, wg, wch, wc, ok, wk, Gf] = ...
    fracture_toughness(P,LPD,CMOD, B, D, a0, ft, S, max_CMOD,b,h)
%This function determines key fracture parameters given load vs. LPD
and
%load vs. CMOD data from a notched beam level II test.
%Inputs: arrays for the following:
%        Load, P
%        Crack Mouth Opening Displacement, CMOD
%        Load Point Displacement, LPD
%Returns:
%          Young's Modulus, E
%          Plastic Flexural Strength, fp
%          Brittleness Length, l1
%          Horizontal intercept of initial portion of softening curve,
w1
%          Fracture Energy, GF
%          Critical crack opening, wc
%          Kink point stress, ok
%          Kink point crack opening, wk
%Written by: Scott Chapman
%Modified: 2/28/2011

%Sensitivity analysis bug fix: Delete any 0 data points at end
while CMOD(end) == 0
    CMOD(end) = [];
    P(end) = [];
    LPD(end) = [];
end
Pm = max(P); %max recorded peak load
%Find location of max P
Pholder = 1;
for i = 1:length(P)
    if Pholder < P(i);
        Pholder = P(i);
        location = i;
    end
end
%9.2.2
%This section gets the values of CMOD and P and calculates the initial
```

```
%compliance, Ci
j = 1; %counter variable
for i = 1:location
    if P(i) > 0.15*Pm && P(i) < 0.55*Pm
        Ptemp(j) = P(i);
        Ctemp(j) = CMOD(i);
        j = j+1;
    end
end
%Find Ci coefficient as CMOD / P
C = polyfit(Ptemp, Ctemp, 1);
Ci = C(1);
%9.2.3
alpha = (a0 + h)/(D + h);

%Calculation of Stress Intensity Factor
V1 = 0.8 - 1.7*alpha + 2.4*alpha^2 + 0.66/(1-alpha)^2 + ...
     4*D/S * (-0.04 - 0.58*alpha + 1.47*alpha^2 - 2.04*alpha^3);

%Calculation of Young's Modulus
E = 6*S*a0 / (Ci*B*D^2) * V1;

%Re-load matrices as neccessary so that CMOD(end) <= max_CMOD
data_length = length(P);
for i = 1:data_length
    if CMOD(i) >= max_CMOD
        CMOD(i) = -1;
    end
end
%delete unneccesary data
while CMOD(end) == -1
    P(end) = [];
    LPD(end) = [];
    CMOD(end) = [];
end
%Get Residual Load
R = P(end);
%Get corrected peak load, P1
P1 = P - R;

%Find location of max P
Pholder = 1;
for i = 1:length(P1)
    if Pholder < P(i);
        Pholder = P(i);
        location = i;
    end
end
P1max = max(P1);

%Determine far tail constant, A, using equation in section 9.3.4.
%Get all data correlated with P1 <= 5% of P1max

counter = 1;
for i = location:length(P1)
```

```
    if P1(i) <= 0.05*P1max;
        wm(counter) = CMOD(i);
        P1x(counter) = P1(i);
        counter = counter+1;
    end
end

%Get CMOD and LPD at end of test, wmr, and CMOD when P1 = 0, wma.
wmr = CMOD(end);
del_r = LPD(end);
%Special case, P1 does not cross x-axis on P vs. CMOD curve,
%so wma and del_a are 0;
counter = 1;
if P1(1) > 0
    wma = 0;
    del_a = 0;
else
    %Otherwise, find location where P1 crosses x-axis on P vs. CMOD
curve
    while P1(counter) < 0;
        counter = counter+1;
    end
    wma = CMOD(counter);
    del_a = LPD(counter);
    %Adjust P1, CMOD, LPD so that there are no data correlated to P1 <
0
    j = 1;
    for i=counter:length(P1)
        P1(j) = P1(i);
        CMOD(j) = CMOD(i);
        LPD(j) = LPD(i);
        j = j+1;
    end
    %Delete left over data
    for i = length(P1) - counter:length(P1)
        P1(end) = [];
        CMOD(end) = [];
        LPD(end) = [];
    end
end

%Get X values, 9.3.4
for i = 1:length(P1x)
    X(i) = ((4*D)/S)^2 * (1/(wm(i) - wma)^2 - 1/(wmr - wma)^2);
end

%Perform least squares fit to get far tail constant, A
p = get_A(X,P1x);
A = p(2);

%Get effective Peak Load, Pmax
Pmax = P1max + A/(wmr - wma)^2;

%Get plastic flexural strength, fp, 9.4.2
fp = Pmax*S/(2*B*(D-a0)^2);
```

```
%Get brittleness length, l1, 9.5.1

%parameters
alpha_0 = a0/D;
k = 1 - alpha_0^1.7;
x = ft/fp;

l1 = k*D*(11.2/(x^2-1)^2 + 2.365/x^2);

%Get horizontal intercept, w1 in micrometers, 9.5.2
w1 = 1000*2*ft*l1/E;

%Get work of fracture from area under P1 vs. LPD curve
Wfm = trapz(LPD,P1);

%Get the total work of fracture
WF = Wfm + 2*A/(del_r - del_a);

%Get the fracture energy, GF, in N/m
GF = 1000*WF/(B*b);

%Get center of gravity of area under softening curve, wg, 9.7.1
wg = 4*A/(B*S*GF)*10^6;

%Get characteristic crack opening, wch, 9.8.2
wch = GF/ft;

%Get critical crack opening of bilinear approximation, wc, 9.8.3
wc = wch*(3*wg-w1)/(2*wch-w1) * (1 + sqrt(...
    1 - 2*w1*(3*wg-2*wch)*(2*wch-w1)/(wch*(3*wg-w1)^2)));

%Get stress at kink point, ok, 9.8.4
ok = ft*(2*wch - w1)/(wc - w1);

%Get crack opening at kink point, wk, 9.8.5
wk = w1*(wc - 2*wch)/(wc - w1);

%Get fracture energy Gf as area under initial part of softening curve
Gf = 0.5*w1*ft;
return
```

```
function [dim, P, LPD, CMOD] = get_data(filename)

%Function "get_data" reads in the values from a text file and outputs
the
%relavent data.
%Returns: P, the load (mm)
%         LPD, the load point displacement (mm)
%         CMOD, the crack mouth opening displacement (mm)
%Written by: Scott Chapman
```

```
%Modified: 8/2/2011


%Load dimension data
%from comma-separated or tab-delimited values
%Note: This section is very specific to a particular set of data.
%Change as needed, or comment out entirely and manually input specific
%data for your specimens

%Name of specimen dimensions file.  Specimen dimensions should be in
the
%following form:
%D, B, a0, preload
data = load('spec_dimensions.txt');
if strcmp(filename, 'spec31.txt') == 1
    dim = data(1,:);
elseif strcmp(filename, 'spec32.txt') == 1
    dim = data(2,:);
elseif strcmp(filename, 'spec33.txt') == 1
    dim = data(3,:);
elseif strcmp(filename, 'spec34.txt') == 1
    dim = data(4,:);
elseif strcmp(filename, 'spec61.txt') == 1
    dim = data(5,:);
elseif strcmp(filename, 'spec62.txt') == 1
    dim = data(6,:);
elseif strcmp(filename, 'spec63.txt') == 1
    dim = data(7,:);
elseif strcmp(filename, 'spec64.txt') == 1
    dim = data(8,:);
elseif strcmp(filename, 'spec91.txt') == 1
    dim = data(9,:);
elseif strcmp(filename, 'spec92.txt') == 1
    dim = data(10,:);
elseif strcmp(filename, 'spec93.txt') == 1
    dim = data(11,:);
elseif strcmp(filename, 'spec94.txt') == 1
    dim = data(12,:);
end

%get pre-load
pre_load = dim(4);

%get specimen data
data2 = load(filename);

P = -1*data2(1:end,2) + pre_load;
for i = 1:length(P)
    LPD(i) = (data2(i, 4)+ data2(i, 5))/2;
    CMOD(i) = -1*(data2(i, 6)+ data2(i, 7))/2;
end
return
```

```
function [p] = get_A(x,y)
% This function fits a curve of P1 vs X (x and y inputs) and fits a
curve
% of the order P1 = KX^2 + AX.  The function outputs the coefficients
of
% the quadratic fit as p = [K A 0]
% This method was taken from the following mathworks solution webpage:
% http://www.mathworks.com/support/solutions/en/data/1-
12BBUC/?product=OP&s
% olution=1-12BBUC
%

%plot the original curve
plot(x,y);

x0 = 0;
y0 = 0;

%reshape the data into a column vector
x = x(:);
y = y(:);

% 'C' is the Vandermonde matrix for 'x'
n = 2; % Degree of polynomial to fit
V(:,n+1) = ones(length(x),1,class(x));
for j = n:-1:1
    V(:,j) = x.*V(:,j+1);
end
C = V;

% 'd' is the vector of target values, 'y'.
d = y;

% There are no inequality constraints in this case, i.e.,
% We use linear equality constraints to force the curve to hit the
required point. In
% this case, 'Aeq' is the Vandermoonde matrix for 'x0'
Aeq = x0.^(n:-1:0);
% and 'beq' is the value the curve should take at that point
beq = y0;

p = lsqlin( C, d, [], [], Aeq, beq );

% We can then use POLYVAL to evaluate the fitted curve
yhat = polyval( p, x );

% Plot original data
plot(x,y,'.b-')
hold on
% Plot point to go through
plot(x0,y0,'gx','linewidth',4)
% Plot fitted data
plot(x,yhat,'r','linewidth',2)
hold off
```

REFERENCES

1. ACI Committee 446-5 (2010), “Fracture Toughness Testing of Concrete”, *ACI Draft Test Procedure*, March, 2010.

2. Bazant, Z.P. and Planas, J. (1998), *“*Fracture and Size Effect in Concrete and Other Quasibrittle Materials*”, CRC Press,* Boca Raton, Florida*,* Chapter 7: Cohesive Crack Models pp. 157-209.

3. Elices, M., Guinea, G.V., Gómez, J., Planas, J. (2002), “The cohesive zone model: advantages, limitations and challenges”, *Engineering Fracture Mechanics*, Vol. 69, pp. 137-163.

4. Guinea, G. V., Pastor, J.Y., Planas, J., Elices, M. (1998), “Stress intensity factor, compliance and CMOD for a general three-point-bend beam” *International Journal of Fracture,* Vol. 89, pp. 103-116.

5. Guinea, G. V, Planas, J. and Elices, M. (1994), “A general bilinear fitting for the softening curve of concrete”, *Materials and Structures,* Vol. 27, 99-105.

6. Hillerborg, A. (1978), “A model for fracture analysis”, *Division of building materials, the lund institute of technology*, Report TVBM-3005.

7. Hillerborg, A. (1985), “The theoretical basis of a method to determine the fracture energy G_F of concrete”, *Materials and Structures,* Vol. 18, pp. 291-296.

8. Lenke, L.R., Gerstle, W.H. (2009), “Standard Test Method for Determination of Direct Tension Fracture Properties of Hardened Concrete Using the Stiff Tension Fracture Test (STFT) Apparatus”, *UNM DRAFT Standard for Stiff Tension Fracture Test*.

9. Petersson, P.-E. (1981), "Crack Growth and Development of Fracture Zones in Plain Concrete and Similar Materials", *Report TVBM-1006, Division of Building Materials*, Lund Institute of Technology, Lund, Sweden.

10. Planas, J., Guinea, G.V. and Elices, M. (1997), “Generalized Size Effect Equation for Quasibrittle Materials”, *Fatigue & Fracture of Engineering Materials & Structures Ltd*, Vol. 20, No. 5, pp. 671-687.

11. Planas, J., Guinea, G. V. and Elices, M. (1999), “Size Effect and Inverse Analysis in Concrete Fracture”, *International Journal of Fracture,* Vol. 95, pp. 367-378.

12. Rocco, C., Guinea, G.V., Planas, J. and Elices, M. (1999), “Size effect and boundary conditions in the Brazilian test: experimental verification”, *Materials and Structures*, Vol. 32, pp 210-217.

13. Shah, S.P., Swartz, S.E., and Ouyang, C., (1995) “Fracture Mechanics of Concrete: Applications of Fracture Mechanics to Concrete, Rock and Other Quasi-Brittle Materials”, *John Wiley & Sons Inc.* Chapter 6: Test Methods to Determine Mode I Fracture Properties of Concrete and Rock pp. 162-242.